Study on Air Interface Variants and their Harmonization for Beyond 5G Systems

Departamento de Comunicaciones
Universitat Politècnica de València

A thesis submitted for the degree of
Doctor por la Universitat Politècnica de València
Valencia, October 2020

Author:
Josué Flores de Valgas

Supervisors:
Dr. Jose F. Monserrat
Dra. Sandra Roger

A la memoria de mi madre,
porque sin ella esto no hubiese sido posible.

Abstract

The standardization of the Fifth Generation of mobile networks or 5G is still ongoing, although the first releases of the standard were completed two years ago and several 5G networks are up and running in several countries around the globe. However, in 2014 when the ITU began the IMT-2020 standardization process, one of the main questions was which would be the waveform to be used on the physical layer of this new generation of technologies. The 3GPP committed to submit a candidate technology to the IMT-2020 process, and that is how within this deliberation process several candidate waveforms were presented. After a thorough evaluation regarding several aspects, in 2016 the 3GPP decided to continue with CP-OFDM (used in 4G) but including, as a novelty, the use of a flexible numerology. Once the waveform was decided, the standardization process continued to fine-tune the frame structure and all the intrinsic aspects of it. This thesis accompanied and participated in this entire process.

To begin with, this dissertation evaluates the main 5G candidate waveforms. Therefore, a theoretical analysis of each waveform is carried out, highlighting its strengths and weaknesses, both at the implementation and performance levels. Subsequently, a real implementation on a Software Defined Radio platform of three of the most promising waveforms (CP-OFDM, UFMC, and OQAM-FBMC) is presented, which allows evaluating their performance in terms of bit error rate, as well as the complexity of its implementation.

This thesis also proposes the use of a harmonized solution as a waveform for 5G and argues that it remains a viable option for systems beyond 5G. Since none of the candidate waveforms was capable of meeting on its own with all the requirements for 5G, instead of choosing a single waveform, this thesis proposes to build a transceiver capable of building all the main waveforms candidates (CP-OFDM, P-OFDM, UFMC, QAM-FBMC, OQAM-FBMC). This is achieved by identifying the common blocks between the waveforms and then integrating them with the rest of the essential blocks for each waveform. The motivation for this solution is to have a physical layer that is capable of complying with all aspects of beyond 5G technologies, always selecting the best waveform according to the scenario. This proposal is evaluated in terms of complexity, and the results are compared with the complexity of each wave-

form.

The decision to continue with CP-OFDM with flexible numerology as a waveform for 5G can also be considered as a harmonized solution, since changing the cyclic prefix and the number of subcarriers, changes also the performance of the system. In this thesis, all the numerologies proposed by the 3GPP are evaluated on each of the channel models described for 5G (and considered valid for beyond 5G systems), taking into account factors such as the mobility of the user equipment and the operating frequency. For this, a 3GPP physical layer simulator is used, and proper adaptations are made in order to evaluate the performance of the numerologies in terms of the block error rate.

Finally, a sketch of what could become the Sixth Generation of mobile networks or 6G is presented, with the aim of understanding the new applications that could be used in the future, as well as their needs.

After the completion of the study carried out in this thesis, it can be said that, as stated from the beginning, for both 5G and beyond 5G systems, the solution is the waveform harmonization. From the results obtained, it can be corroborated that a harmonized solution allows achieving computational savings between 25-40% for the transmitter and 15-25% for the receiver. In addition, it is possible to identify which CP-OFDM numerology is the most appropriate for each scenario, which would allow optimizing the design and deployment of 5G networks. This would open the door to doing the same with 6G, since in this thesis it is considered that it will be necessary to reopen the debate on which is the appropriate waveform for this new generation of technologies, and it is suggested that the way forward is to opt for a harmonized solution with different waveforms, instead of just one, as it is the case with 5G.

Resumen

La estandarización de la Quinta Generación de redes móviles o 5G, ha concluido este año 2020. No obstante, en el año 2014 cuando la ITU empezó el proceso de estandarización IMT-2020, una de las principales interrogantes era cuál sería la forma de onda sobre la cual se construiría la capa física de esta nueva generación de tecnologías. El 3GPP se comprometió a entregar una tecnología candidata al proceso IMT-2020, y es así como dentro de este proceso de deliberación se presentaron varias formas de onda candidatas, las cuales fueron evaluadas en varios aspectos hasta que en el año 2016 el 3GPP tomó una decisión, continuar con CP-OFDM (utilizada en 4G) con numerología flexible. Una vez decidida la forma de onda, el proceso de estandarización continuó afinando la estructura de la trama, y todos los aspectos intrínsecos de la misma. Esta tesis acompañó y participó de todo este proceso.

Para empezar, en esta disertación se evaluaron las principales formas de onda candidatas al 5G. Es así que se realizó un análisis teórico de cada forma de onda, destacando sus fortalezas y debilidades, tanto a nivel de implementación como de rendimiento. Posteriormente, se llevó a cabo una implementación real en una plataforma Software Defined Radio de tres de las formas de onda más prometedoras (CP-OFDM, UFMC y OQAM-FBMC), lo que permitió evaluar su rendimiento en términos de la tasa de error por bit, así como la complejidad de su implementación.

Esta tesis ha propuesto también el uso de una solución armonizada como forma de onda para el 5G y sostiene que sigue siendo una opción viable para sistemas beyond 5G. Dado que ninguna de las forma de onda candidatas era capaz de cumplir por sí misma con todos los requisitos del 5G, en lugar de elegir una única forma de onda se propuso construir un transceptor que fuese capaz de construir todas las principales formas de onda candidatas (CP-OFDM, P-OFDM, UFMC, QAM-FBMC, OQAM-FBMC). Esto se consiguió identificando los bloques comunes entre las formas de onda, para luego integrarlos junto con el resto de bloques indispensables para cada forma de onda. La motivación para esta solución era tener una capa física que fuese capaz de cumplir con todos los aspectos del 5G, seleccionando siempre la mejor forma de onda según el escenario. Esta propuesta fue evaluada en términos de complejidad, y los resultados se compararon con la complejidad de cada forma de onda.

La decisión de continuar con CP-OFDM con numerología flexible como forma de onda para el 5G se puede considerar también como una solución armonizada, ya que al cambiar el prefijo cíclico y el número de subportadoras, cambian también las prestaciones del sistema. En esta tesis se evaluaron todas las numerologías propuestas por el 3GPP sobre cada uno de los modelos de canal descritos para el 5G (y considerados válidos para sistemas beyond 5G), teniendo en cuenta factores como la movilidad de los equipos de usuario y la frecuencia de operación; para esto se utilizó un simulador de capa física del 3GPP, al que se hicieron las debidas adaptaciones con el fin de evaluar el rendimiento de las numerologías en términos de la tasa de error por bloque.

Finalmente, se presenta un bosquejo de lo que podría llegar a ser la Sexta Generación de redes móviles o 6G, con el objetivo de entender las nuevas aplicaciones que podrían ser utilizadas en un futuro, así como sus necesidades.

Completado el estudio llevado a cabo en esta tesis, se puede afirmar que como se propuso desde un principio la solución, tanto para el 5G como para beyond 5G, la solución es la armonización de las formas de onda. De los resultados obtenidos se puede corroborar que una solución armonizada permite alcanzar un ahorro computacional entre el 25-40% para el transmisor y del 15-25% para el receptor. Además, fue posible identificar qué numerología CP-OFDM es la más adecuada para cada escenario, lo que permitiría optimizar el diseño y despliegue de las redes 5G. Esto abriría la puerta a hacer lo mismo con el 6G, ya que en esta tesis se considera que será necesario abrir nuevamente el debate sobre cuál es la forma de onda adecuada para esta nueva generación de tecnologías, y se plantea que el camino a seguir es optar por una solución armonizada con distintas formas de onda, en lugar de solo una como sucede con el 5G.

Resum

L'estandardització de la Quinta Generació de xarxes mòbils o 5G, ha conclòs enguany 2020. No obstant això, l'any 2014 quan la ITU va començar el procés d'estandardització IMT-2020, uns dels principals interrogants era quina seria la forma d'onda sobre la qual es construiria la capa física d'esta nova generació de tecnologies. El 3GPP es va comprometre a entregar una tecnologia candidata al procés IMT-2020, i és així com dins d'este procés de deliberació es van presentar diverses formes d'onda candidates, les quals van ser avaluades en diversos aspectes fins que l'any 2016 el 3GPP va prendre una decisió, continuar amb CP-OFDM (utilitzada en 4G) amb numerología flexible. Una vegada decidida la forma d'onda, el procés d'estandardització va continuar afinant la frame structure (no se m'ocorre nom en espanyol), i tots els aspectes intrínsecs de la mateixa. Esta tesi va acompanyar i va participar de tot este procés.

Per a començar, en esta dissertació es van avaluar les principals formes d'onda candidates al 5G. És així que es va realitzar una anàlisi teòrica de cada forma d'onda, destacant les seues fortaleses i debilitats, tant a nivell d'implementació com de rendiment. Posteriorment, es va dur a terme una implementació real en una plataforma Software Defined Radio de tres de les formes d'onda més prometedores (CP-OFDM, UFMC i OQAM-FBMC), la qual cosa va permetre avaluar el seu rendiment en termes de la taxa d'error per bit, així com la complexitat de la seua implementació.

Esta tesi ha proposat també l'ús d'una solució harmonitzada com a forma d'onda per al 5G i sosté que continua sent una opció viable per a sistemes beyond 5G. Atés que cap de les forma d'onda candidates era capaç de complir per si mateixa amb tots els requeriments del 5G, en compte de triar una única forma d'onda es va proposar construir un transceptor que fóra capaç de construir totes les principals formes d'onda candidates (CP-OFDM, P-OFDM, UFMC, QAM-FBMC, OQAM-FBMC). Açò es va aconseguir identificant els blocs comuns entre les formes d'onda, per a després integrar-los junt amb la resta de blocs indispensables per a cada forma d'onda. La motivació per a esta solució era tindre una capa física que fóra capaç de complir amb tots els aspectes del 5G, seleccionant sempre la millor forma d'onda segons l'escenari. Esta proposta va ser avaluada en termes de complexitat, i els resultats es van comparar amb la complexitat de cada forma d'onda.

La decisió de continuar amb CP-OFDM amb numerología flexible com a forma d'onda per al 5G es pot considerar també com una solució harmonitzada, ja que al canviar el prefix cíclic i el número de subportadores, canvien també les prestacions del sistema. En esta tesi es van avaluar totes les numerologías propostes pel 3GPP sobre cada un dels models de canal descrits per al 5G (i considerats vàlids per a sistemes beyond 5G), tenint en compte factors com la mobilitat dels equips d'usuari i la freqüència d'operació; per a açò es va utilitzar un simulador de capa física del 3GPP, a què es van fer les degudes adaptacions a fi d'avaluar el rendiment de les numerologías en termes de la taxa d'error per bloc.

Finalment, es presenta un esbós del que podria arribar a ser la Sexta Generació de xarxes mòbils o 6G, amb l'objectiu d'entendre les noves aplicacions que podrien ser utilitzades en un futur, així com les seues necessitats.

Completat l'estudi dut a terme en esta tesi, es pot afirmar que com es va proposar des d'un principi la solució, tant per al 5G com per a beyond 5G, la solució és l'harmonització de les formes d'onda. dels resultats obtinguts es pot corroborar que una solució harmonitzada permet aconseguir un estalvi computacional entre el 25-40% per al transmissor i del 15-25% per al receptor. A més, va ser possible identificar què numerología CP-OFDM és la més adequada per a cada escenari, la qual cosa permetria optimitzar el disseny i desplegament de les xarxes 5G. Açò obriria la porta a fer el mateix amb el 6G, ja que en esta tesi es considera que serà necessari obrir novament el debat sobre quina és la forma d'onda adequada per a esta nova generació de tecnologies, i es planteja que el camí que s'ha de seguir és optar per una solució harmonitzada amb distintes formes d'onda, en compte de només una com succeïx amb el 5G.

Acknowledgements

Me gustaría agradecer a todas las personas que han formado parte de este camino junto a mí, y que me han ayudado a cumplir con el objetivo de culminar esta Tesis Doctoral. En primer lugar me gustaría agradecerle a mis tutores, el Profesor Jose F. Monserrat y la Dra. Sandra Roger por haberme dado la oportunidad de trabajar junto a ellos dentro del Grupo de Comunicaciones Móviles. De manera especial me gustaría agradecer al Profesor Jose F. Monserrat sobre todo por su apoyo y guía durante todos estos años. He pasado por momentos muy duros a nivel personal desde que comencé el Doctorado, y lejos de enfadarse cuando esto afectaba mi trabajo siempre supo encontrar la manera de motivarme a seguir adelante, por eso y más le estaré siempre agradecido. También me gustaría agradecer a todos mis compañeros de iTEAM, cada uno de ellos ha contribuido de alguna manera y en algún momento a la consecución de este logro, así que por toda la ayuda que me han brindado les estoy muy agradecido.

Quisiera agradecerle también al Profesor Hüseyin Arslan por haberme permitido realizar mi estancia en su grupo de investigación en la Universidad de Medipol en Estambul. Fue una experiencia excepcional tanto a nivel personal como profesional, y estar ahí me permitió conocer a un grupo especial de gente de quienes guardo un grato recuerdo.

Por último, pero no por ello menos importante, me gustaría agradecer a mi familia y amigos todo el apoyo mostrado durante estos años, en especial en los momentos más duros. Gracias a mis padres, Kerlly y Carlos, sobre todo a mi madre ya que en su memoria va dedicado todo este trabajo; a mis hermanos Melissa, Karla, Camilla y Carlos, siempre han estado allí para alentarme. A mis queridos amigos de la "Embajada", parte de mi familia lejos de casa, a los que siguen aquí y a los que ya han vuelto: Terry, Carlos S, Alfredo S, Carlos B, Francisco, Adrián, Caro, Kath, Iván, Manuel, Patri, Gabriel, Jairo, Albita, Andrés; gracias por todos los momentos compartidos y por hacer que me sintiese más cerca de Ecuador cuando así lo necesitaba. A mi gente de "Awesome People" quienes han sido también mi familia aquí: Esteban, Lucho, Laura P, André, Ariel, Katy, Louise, Mati, Simona; siempre han estado para mí cuando lo he necesitado, y estoy agradecido por haberlos conocido y que hayan estado junto a mí mientras he recorrido este camino. De igual manera quiero agradecer a mi familia del baile: Vicente, Irene, Sara, Vicky, Xavi, Jose, Javi, Angie,

Héctor, Paula; en poco tiempo se han ganado mi cariño y me han demostrado que puedo contar siempre con "vosotros" ja, ja. He querido hacer una dedicación especial a mi muñequita, Laura, porque sin su apoyo en esta recta final hubiese sido mucho más difícil llegar hasta aquí, gracias por motivarme, por apoyarme y por acompañarme, te quiero por eso y por mucho más.

Josué
Valencia, Noviembre 2020

Table of contents

Acronyms

3GPP	Third Generation Partnership Project
3G	Third Generation
4G	Fourth Generation
5G	Fifth Generation
5G-PPP	Fifth Generation Public Private Partnership
AFB	Analysis Filter Bank
AGC	Automatic Gain Control
AI	Air Interface /Artificial Intelligence
AIVs	AI variants
AR	Augmented Reality
AWGN	Additive White Gaussian Noise
BER	Bit Error Rate
BPSK	Binary Phase-Shift Keying
CFO	Carrier Frequency Offset
CoMP	Coordinated Multi-Point
CP	Cyclic Prefix
CP-OFDM	Cyclic Prefix OFDM
D2D	Device-to-Device
DFT	Discrete Fourier Transform
DFT-s-OFDM	Discrete Fourier Transform-spread-OFDM
DL	Deep Learning
DS	Delay Spread
DSA	Dynamic Spectrum Access

D-OFDM	Dynamic OFDM
EC	European Commission
eMBB	Enhanced Mobile Broadband
eURLLC	Enhanced Ultra Reliable and Low Latency Communications
F-RAN	Fog-Radio Access Network
F-OFDM	Filtered OFDM
FBMC	Filtered Bank Multi-Carrier
FFT	Fast Fourier Transform
FIR	Finite Impulse Response
FPGA	Field-programmable Gate Array
FSO	Free-Space Optical
GFDM	Generalized Frequency Division Multiplexing
GI	Guard Interval
HUD	Heads Up Displays
ICI	Inter-Carrier Interference
ICT	Information and Communications Technology
IDFT	Inverse Discrete Fourier Transform
IFFT	Inverse FFT
IMT-2000	International Mobile Telecommunication 2000
IMT-Advanced	International Mobile Telecommunication-Advanced
IMT-2020	International Mobile Telecommunication 2020
INI	Inter-numerology Interference
IoT	Internet of Things
ISI	Inter-Symbol Interference
ITU	International Telecommunication Union
ITS	Intelligent Transportation Systems
KPI	Key Performance Indicator
LoS	Line of Sight
LTE	Long Term Evolution
LTE-A	Long Term Evolution Advanced
LTE-V	LTE Vehicle

LTS	Long Training Sequence
M2M	Machine-to-Machine Communications
MAC	Medium Access Control
MEC	Mobile Edge Computing
METIS	Mobile and wireless communications Enablers for Twenty-twenty Information Society
MIMO	Multiple-Input Multiple-Output
ML	Machine Learning
mMTC	Massive machine type communications
mmWave	millimeter wave
multi-TRP	Multiple Transmission Reception Point
NLoS	Non Line of Sight
NOMA	Nonorthogonal Multiple Access
NR	New Radio
OFDM	Orthogonal Frequency Division Multiplexing
OFDMA	Orthogonal Frequency Division Multiple Access
OOB	out-of-band
OQAM	Offset QAM
OQAM-FBMC	Offset QAM Filter Bank Multicarrier
PAPR	Peak-to-Average Power Ratio
PHY	Physical
PHYDAS	Physical Layer for Dynamic Spectrum Access and Cognitive Radio
P-OFDM	Pulse Shaped OFDM
PPN	Polyphase Network
PRB	Physical Resource Block
QAM	Quadrature Amplitude Modulation
QAM-FBMC	QAM Filter Bank Multicarrier
QC	Quantum Computing
QoS	Quality of Service
QPSK	Quadrature Phase Shift Keying
RAN	Radio Access Network

RB	Resource Block
RMa	Rural Macro
RMS	Root Mean Square
RX	Receiver
SA	System Architecture
SDN	Software Defined Networks
SER	Symbol Error Rate
SDR	Software Defined Radio
SFB	Synthesis Filter Bank
SINR	Signal to Interference plus Noise Ratio
SISO	Single Input Single Output
SMT	Staggered Multitone
SNR	Signal to Noise Ratio
STS	Short Training Sequence
S-UHD	Super-Ultra High Definition
TA	Timing Advance
TDD	Time Division Duplexing
TDL	Tapped Delay Line
TO	Timing Offset
TRP	Transmission Reception Point
TTI	Transmission Time Interval
TX	Transmitter
UDP	User Datagram Protocol
UE	User Equipment
UFMC	Universal Filtered MultiCarrier
UMBB	Ultra Mobile Broadband
UMa	Urban Macro
UMi	Urban Micro
URLLC	Ultra-reliable and low latency communications
V2V	Vehicle-to-vehicle
V2X	Vehicle-to-everything

VLC	Visible Light Communications
VR	Virtual Reality
VRS	Virtual Reality Server
W-OFDM	Windowed-OFDM
WAVE	Wireless Access in the Vehicular Environment
WiMAX	Worldwide Interoperability for Microwave Access
ZF	Zero Forcing

Chapter 1

Introduction

1.1 Background

The role that Long Term Evolution (LTE) and Long Term Evolution Advanced (LTE-A) have played in the wireless industry has been fundamental, facilitating the mobile industry to come together, enabling single technology deployments, and allowing a tremendous progress over the last years. LTE is currently used by a quarter of all global mobile subscribers and continue to expand across the world, even reaching a 90 percent penetration in some countries. However, with technology advancing very quickly, new challenges also appeared and these were properly addressed by the appearance of the Fifth Generation (5G) mobile. One of the main new challenges is the Internet of Things (IoT), which expands the internet as it is currently known by adding a large number of objects like sensors/actors (e.g. power meters) that connect wirelessly to each other, allowing these to collect and exchange data. Any exchange of data that occurs directly between two or more network devices on the cellular frequencies (i.e., inband) or unlicensed spectrum (i.e., outband) is what is known as Device-to-Device (D2D) Communication [1, 2]. The use cases of IoT certainly differ greatly from the devices currently connected to the Fourth Generation (4G) network. This is why a system that incorporates IoT devices is probably not able to apply synchronization requirements as demanding as those used in 4G, due to energy and cost reasons. Another challenge that arises is the use of millimeter wave (mmWave) to support IoT applications. It is known that mmWave use cases promise to bring new levels of capacity and efficiency, supporting a wide range of applications and devices; however, mmWave have shown their potential to solve these problems by presenting themselves

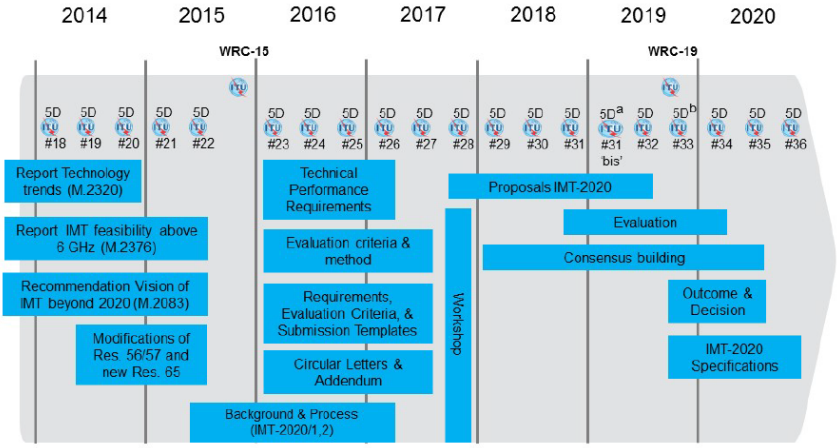

Figure 1.1: Detailed Timeline and Process For IMT-2020 in ITU [8]

as a perfect support for massive IoT applications and services [3, 4]. In this context of evolution appeared the 5G.

1.1.1 5G wireless standard

Due to everything mentioned above the research community and the mobile industry have focused in the establishment of 5G mobile wireless technology and standards development. As with previous mobile generations, the International Telecommunication Union (ITU) is in charge of demarking the requirements and recommendations that serve as a guide for the constitution of 5G. As happened with the Third Generation (3G) when the International Mobile Telecommunication 2000 (IMT-2000) [5] was defined, and with 4G when the ITU established International Mobile Telecommunication-Advanced (IMT-Advanced) [6], now the ITU is working on the International Mobile Telecommunication 2020 (IMT-2020) [7] process to define the 5G requirements. The IMT-2020 standardization work began in 2014, and considers services based on more data capacity and speed, low latency, the ability to massify technologies, autonomous vehicles, permanent connection, among others; and as its name implies, it is expected to end in year 2020, complying with the procedure of defining the requirements, accepting the proposed technologies, and evaluating and certifying those that meet the established requirements.

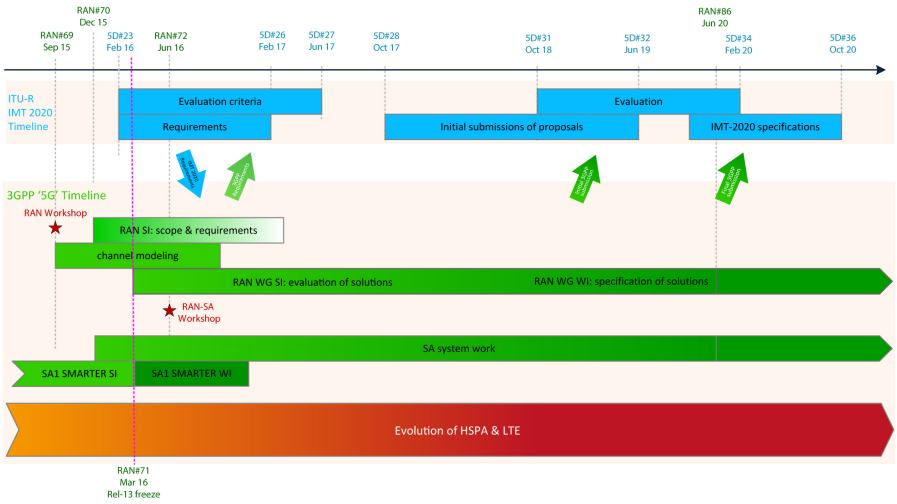

Figure 1.2: 5G timeline in 3GPP [11]

In parallel and jointly with the ITU the Third Generation Partnership Project (3GPP) has been working to define 5G, discussing technologies and system architectures that will be needed to comply with the IMT-2020 specifications, and committing themselves to submit a candidate technology to the IMT-2020 process. The 3GPP has attempted to accomplish this through a work program composed of two phases: in the first one study items were made for Rel-14 [9], while in the second, the launch of two releases with specifications that cover the requirements demanded by IMT-2020 was proposed, i.e. Release 15 [10] and Release 16, and so far it has been accomplished. Figures 1.1 and 1.2 show respectively the proposed timelines by the ITU and 3GPP to deliver a 5G standard, which aligns perfectly with the 5G research projects, pre-standards work and also the priorities for 3GPP work from Release 15 onwards.

The need to have a higher data capacity and higher throughput, proves that broadband services need to be improved. Even so, within 5G there are other relevant edges to consider. The ITU has classified the 5G usage scenarios into three large groups: Enhanced Mobile Broadband (eMBB), Ultra-reliable and low latency communications (URLLC), and Massive machine type communications (mMTC) [12].

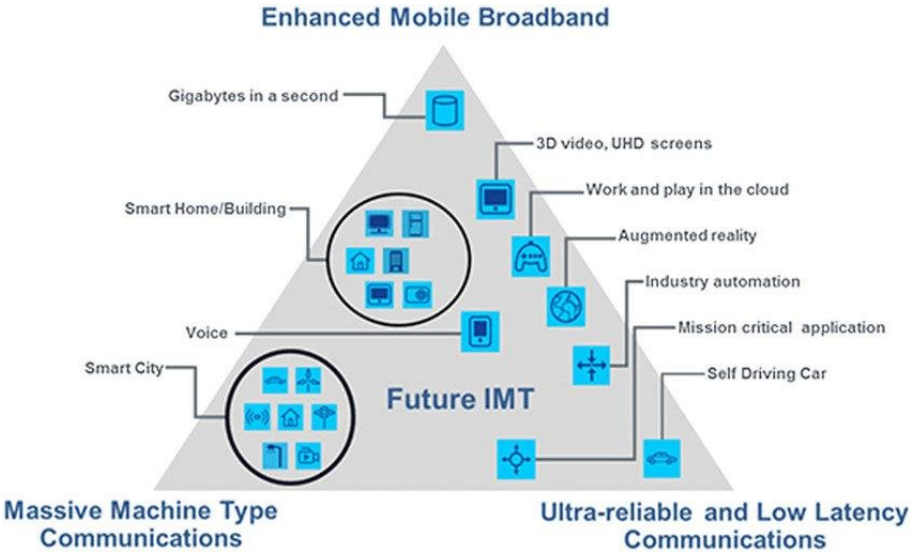

Figure 1.3: Usage scenarios of IMT-2020 and beyond [12]

Enhanced Mobile Broadband

This use case can be considered to be a direct extension of the 4G broadband service, and is focused on reaching of up to 10 Gbps peak throughput, 1 Gbps in high mobility scenarios, and an increasement up to 10,000 times of the total network traffic. Recent research has shown that these numbers are feasible, and that mmWave and Multiple-Input Multiple-Output (MIMO) are a crucial part to achieve this goal. eMBB is expected to provide high resolution multimedia streaming in mobility scenarios, real-time big data processing, ultra-high speed services in both indoor and outdoor, Augmented Reality (AR) and VR applications.

In order to achieve real time processing, very low latency and low network congestion are required, that is why many of the current research topics consider that bringing computing capability and services to the network edge [13, 14] (concept known as Edge Computing) will facilitate this type of services. The use of Edge Computing in combination with cloud services allows provisioning and proper and efficient resource allocation, which will become key for applications that use eMBB. At this point, it is worth clarifying the difference between Edge Computing and fog computing [15–17]. Edge Computing refers to the physical place where resources or nodes are placed; however, fog

computing is the way in which these nodes are organized and work cooperatively. A node that is part of a fog computing network might be or not on the edge. There is a proposal called 5G-MiEdge [18, 19] that combines mmWave and Edge Computing in a hybrid architecture to provide eMBB services. Centralized communications, cloud storage and computing resources are placed towards the closest edge from the devices, also using direct backup communication lines (backhaul) between edge nodes. In this architecture, the processing of data in the order of gigabits is supported by the placement of resources in areas closer to the distribution of the signal, improving response times and offloading cloud computing requirements.

On the other hand, VR applications need to connect to Virtual Reality Server (VRS) to download a huge amount of data, and must do so without delays in the data transmission, a requirement that must be met even in areas where there is a great accumulation of people and in public places. It is known that VR devices will have a high energy consumption because of the aforementioned massive data transmission, and they will be affected by interference from neighboring devices using mmWave, a problem that can be addressed by applying different interference management techniques.

Ultra-reliable and low latency communications

The mmWave are used to send important information with high reliability or, in other words, with an extremely low rate of lost package. This high reliability, together with the low latency, is what is called URLLC, which not necessarily implies high throughput. Some examples of this type of communications could be: natural disaster management, health and hospital environments, military communications, industrial communications, and vehicle applications that need great precision. Nonetheless, even within these examples the characteristics may vary, since latency may be a requirement that goes from less than 1 ms to several seconds, while on the other hand in sanitary applications the reliability to deliver real-time information is essential. Therefore, the 5G deployment must be sensitive enough to support all these scenarios.

One of the main critics towards mmWave is its difficult propagation and easy obstruction, which in first instance could complicate the deployment when the requirement is reliability and low latency. Nevertheless, there are two important points to consider in order to address this problem: the core network design and mobility management. With the purpose of achieve URLLC in 5G using mmWave, it is necessary to understand how mobile networks currently work. In the process of data transmission, the packages that suffer a high

delay are those that need to go through the core network to reach their destination. That is why for 5G the core network functions are taken to a place closer to where the signal is managed, i.e. the network edge. There are three technologies that promise to be the solution to these problems: Mobile Edge Computing (MEC) [20], Software Defined Networks (SDN) [21] and Fog-Radio Access Network (F-RAN) [22]. In addition, we must consider the technology used for eMBB (i.e. 5G-MiEdge), which combines integrated access and backhaul, which facilitates the configuration of small cells with flexible resource allocation.

To support high mobility URLLC scenarios, these requirements must be fulfilled:

- Handover: Moving from one radio link to another, or from one network to another cannot lead to packet loss or delay, and it must be ensured that is carried out without service interruptions.
- Redundant links: in order to have ultra-reliable communications it is necessary to provide link redundancy both in radio access and in the rest of the infrastructure, and these links should be arranged through different radio access nodes.
- Transmission schemes: the system must provide a robust transmission scheme that allows simultaneous transmission through redundant links, in a both coordinated and uncoordinated way.

Precisely these factors are the key to overcome the problem of the channel being unreliable due to the intensity of physical blocking, since they open the possibility of having redundant links and using them to send and receive information simultaneously, which is a technique known as Multiple Transmission Reception Point (multi-TRP) [23]. In high mobility scenarios and high user density, users are likely to experience frequent handovers, running the risk of partial loss of service or slowdown. To avoid such situations, the user must always be attended by a Transmission Reception Point (TRP) with sufficient power and their data must be transferred to the destination TRP before a handover is initiated. As indicated earlier, the availability of these resources at the edge are a solution to this problem.

Massive machine type communications

According to estimations [24] in 2023 there will be 13.1 million mobile devices connected, including those that use Machine-to-Machine Communications (M2M). It is also estimated that 5G communications will generate 4.7

times more traffic than current 4G. mMTC is the basis for Internet of things, allowing several types of communications interacting at the same time, to be something is increasingly palpable. However, not all devices are connected all the time: they can only be receiving data, transmitting them or simply in standby, that is why mMTC device is considered active intermittently and uses a fixed, typically low, transmission rate in the uplink. On the other hand, mMTC is expected to facilitate the efficiency and flexibility of the network so that the size and rate of the packets is variable. Therefore, the main challenge of mMTC is the management of a massive amount of devices connected in an uncoordinated way, unlike current mobile networks, designed for perfectly coordinated voice transmissions and data transfer in a homogeneous way.

It is also important to emphasize the work that 3GPP has done regarding the new Radio Access Network (RAN) and the new System Architecture (SA), especially those studies carried out by the 3GPP RAN working groups, which focus on a new radio access for 5G called New Radio (NR). This NR must be flexible enough to support a wider range of frequency bands that goes from 6GHz to mmWave bands of 100 GHz. Due to this large range of carrier frequencies, one of the key elements within NR will be the waveform used for signal transmission, and along with it, other important factors within NR are the frame structure, the use of MIMO techniques, beamforming, coding, and others.

1.1.2 Air Interface Harmonization

Another of the important actors in the 5G standardization process is the Fifth Generation Public Private Partnership (5G-PPP), which is a joint initiative between the European Commission (EC) and the Information and Communications Technology (ICT) industry, with the intention of delivering solutions, technologies, architectures and standards within 5G. In a broad scale, 5G-PPP is organized into 3 phases: Research, Optimization, Large-scale Trials, and in each of these phases there is a variety of projects dedicated to the different aspects covered by 5G. This thesis is framed in two 5G-PPP projects: Mobile and wireless communications Enablers for Twenty-twenty Information Society (METIS) and METIS-II. In METIS [25], the bases of 5G were established, with the aim of meeting the communication needs of 2020 society. Here, different techniques and multiple antennas algorithms were proposed, which have caused a great impact on 5G. On the other hand, METIS-II focused on the architectural elements needed for the technology components proposed on METIS, in order to have a comprehensive and detailed RAN specification.

Besides, METIS-II has tried to verified that this overall RAN design is techno-economically achievable and energy-efficient.

One of the concepts managed in METIS-II is the Air Interface (AI) harmonization, which refers to the use of different AI variants (AIVs) in an organized manner and according to the different scenarios, with the purpose of maximizing the system's performance. AIVs are the components of the physical layer that determine the reliability, complexity and throughput of the system, e.g. modulation and waveform. In regards to waveforms, although OFDM has been widely used in communications systems, especially in 4G, it can hardly meet by itself the purpose of having a common RAN that covers all 5G use cases (ie eMBB, mMTC and URLLC). This is due to the characteristics of 5G, which have been noted above. For instance, in 4G the devices are connected to the network with a cell-centric behavior, and many protocols and procedures that cover the lower levels of the communications stack (Physical (PHY), Medium Access Control (MAC)), such as time/frequency synchronization and control signaling, are linked to the cell the device is connected to. Therefore, today the cell would be the network element that can be considered as the center of the access layer. In 5G a user-centered processing concept is handled, which discards the basic notion of cell, allowing many aspects of wireless communications such as Coordinated Multi-Point (CoMP), mobility management and offloading to benefit greatly from this. Another key feature of user-centered processing is that normally the devices will be connected to multiple access points. Naturally, the distances between the device and all the access points are divergent and their respective carrier frequencies may also differ. Therefore, a highly demanding synchronization such as that required in LTE does not appear to be effective or even possible for a future system with user-centered processing.

In this sense, two approaches were initially made for the overall AI design. On one hand, the use of a single family of waveforms was considered, i.e. OFDM, using different numerologies and minor modifications and improvements of the waveform in order to cover the diverse cells types, services, and bands. On the other hand, there was another approach proposed which considered the co-existence of different waveforms that jointly fulfill the overall space of cell types, services, and bands; thus, more flexible waveforms were proposed for the 5G standardization process.

1.2 State of the art

The waveform study started even before the formal beginning of the standardization process of 5G by 3GPP. Different waveforms were proposed as candidates for the 5G and as an alternative to the well-known CP-OFDM, among which are: Filtered OFDM (F-OFDM) [26], Universal Filtered Multi-Carrier (UFMC) [27], Pulse Shaped OFDM (P-OFDM) [28], Windowed-OFDM (W-OFDM) [29], Discrete Fourier Transform-spread-OFDM (DFT-s-OFDM) [29, 30], Generalized Frequency Division Multiplexing (GFDM) [31], QAM Filter Bank Multicarrier (QAM-FBMC) [32], and Offset QAM Filter Bank Multicarrier (OQAM-FBMC) [33]. Many studies conducted at that time also offered comparisons between two or three particular waveforms [34–37], while others analyzed the candidates by evaluating specific characteristics [38–41]. In addition, it is important to also highlight some testbeds that were carried out to have a more realistic evaluation of their performance [42–44]. During this evaluation stage, many proposals were launched from the academy and from the industry, which on more than one occasion came together to work on projects with specific objectives for the 5G physical layer.

Despite the advantages of the numerous candidates, it was clear that none was capable of meeting on its own with all the challenges that 5G presented, therefore the 3GPP decided that none of the candidate waveforms was good enough to replace CP-OFDM and make such an important change in the physical layer. That is why in August 2016 the 3GPP opted for CP-OFDM with different numerologies [45], to be the 5G waveform in both the uplink and the downlink. Since then the study of waveforms has focused on solving the different problems that could arise for mixed numerologies. In this sense, there have been field test studies [46], studies on techniques to optimize multiple access schemes such as Nonorthogonal Multiple Access (NOMA) [47, 48], studies that focus on minimizing Inter-numerology Interference (INI) [49–51], and studies that use 5G numerology in different applications such as Vehicle-to-everything (V2X) [52] and mmWave [53].

Currently, 5G is a reality, its physical layer is defined and along with it the waveform to be used. There are countries in which the deployment of small networks has begun, and this deployment is expected to grow in the coming years. However, despite the standardization process recently concluded, the concepts of "beyond 5G", and the sixth generation of mobile technologies (6G), have been on the table for some time. Some articles offer a glimpse of what 6G could become [54–57], and along with this, the waveform debate is reopened and new proposals for the physical layer of beyond 5G systems are being presented

[58–62]. Here it is where this Thesis provides a deep analysis on the different waveforms and their interest in the future development of 3GPP standards.

1.3 Objectives and Thesis scope

The main objective behind the effort of evaluating real implementations of 5G access scheme proposals is to provide a significant ubiquitous boost improvement on the experienced and expected Quality of Service (QoS) of users of the 5G cellular mobile communications systems and minimize, at the same time, the consumption of resources and the impact on the current 3GPP standard network architectures. With this purpose the following partial objectives are proposed when evaluating real implementations of these contributions:

- Promote the assessment of solutions that make easier the deployment of a simplified infrastructure of the access network (e.g. advanced relays in their multi-hop cellular mode).
- Foster the development of new RAN concepts and their integration into the preceding systems, from the control plane and user plane point of view.
- Harmonizing the research effort on different PHY layer multi-access alternatives, suitably including jointly alternative contenders to Orthogonal Frequency Division Multiplexing (OFDM), such as UFMC and OQAM-FBMC; and paying particular attention to its implementability (design and implementation of prototype hardware solutions) and its strong points, (e.g. robustness to the lack of uplink network synchronism).
- Consolidate the innovations obtained in the above objectives, including the performance evaluation of the developed solutions and their integration in 3GPP roadmap.

1.4 Thesis outline and main contributions

This thesis is organized into five chapters as follows:

Chapter 2 describes in detail the main 5G waveforms candidates, analyzing their main characteristics, strengths and weaknesses.

Chapter 3 explains the implementation of some waveforms in a Software Defined Radio (SDR) platform and presents a performance comparison of them.

Chapter 4 addresses the harmonization of the main 5G waveforms candidates, analyzing the viability of this approach from a complexity point of view.

Chapter 5 provides an in-depth analysis of the use of 5G numerologies within the main 5G channel models.

Chapter 6 carries out a conceptualization exercise of the 6G from the conviction that the conventional base stations will be removed.

Chapter 7 draws the main conclusions of this thesis and presents the future research lines of this work.

1.5 Publications

International journals

[J1] D. Garcia-Roger, S. Roger, **J. Flores de Valgas**, J. F. Monserrat, "Multicarrier Waveform Harmonization and Complexity Analysis for an Efficient 5G Air Interface Implementation", Wireless Communications and Mobile Computing, pp. 11, 2017.

[J2] **J. Flores de Valgas**, J. F. Monserrat, H. Arslan "Flexible Numerology in 5G NR: Interference Quantification and Proper Selection Depending on the Scenario", Mobile Information System, pending publication.

National journals

[I1] **J. Flores de Valgas**, David Martín-Sacristán, J. F. Monserrat, "5G New Radio Numerologies and their Impact on V2X Communications", WAVES Magazine, 2018.

International conferences

[C1] D. Garcia-Roger, **J. Flores de Valgas**, J. F. Monserrat, N. Cardona, N. Incardona, "Hardware testbed for sidelink transmission of 5G waveforms without synchronization", in Proc. IEEE International Symposium on Personal, Indoor and Mobile Radio Communications (PIMRC), 2016.

[C2] J. F. Monserrat, D. Martin-Sacristan, F. Bouchmal, O. Carrasco, **J. Flores de Valgas**, N. Cardona, "Key technologies for the advent of the 6G", in IEEE wireless communications and networking Conference Workshops (WCNCW), pp. 1-6, 2020.

Chapter 2

5G Waveform Candidates

This chapter provides a broad analysis and comparison of the main 5G waveforms that were the main candidates at the time. In order to obtain an enlightening analysis, this chapter introduces the basic principles of the waveform, without forgetting to explain the fundamental characteristics of each waveform, their strengths and weaknesses, and its suitability into the 5G and beyond overall landscape.

This chapter is organized as follows:

- Section 2.1 describes the best known OFDM-based waveforms.
- Section 2.2 describes the best known FBMC-based waveforms.
- Section 2.3 presents the most important conclusions.

2.1 OFDM-based Solutions

Cyclic Prefix OFDM (CP-OFDM) is the best known and most used multicarrier waveform. It was created for mobile broadband communications, such as WiFi, Worldwide Interoperability for Microwave Access (WiMAX) and LTE. In a 5G context, where supporting multiple services simultaneously will be essential, classical CP-OFDM may not be the best option, since frequency multiplexing numerous subcarriers is not possible without causing interference between them, given its inherent weak sub-band isolation. CP-OFDM is an Inverse FFT (IFFT) based modulation, where each symbol is separated by a Cyclic Prefix (CP), which is a copy of the last samples of the time-domain

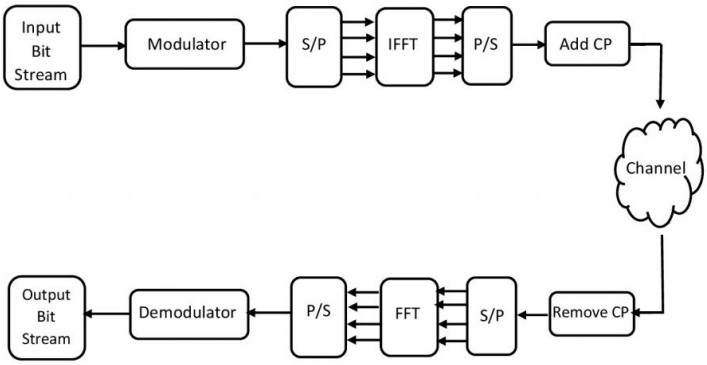

Figure 2.1: OFDM block diagram

symbol.

In a CP-OFDM system, the transmitted data is mapped to some constellation points in order to obtain data symbols. The transmitter then applies an N-point Inverse Discrete Fourier Transform (IDFT), with the purpose of obtaining the time domain CP-OFDM symbols. The time domain CP-OFDM n-th block $\mathbf{x}_{[}n] = [x_{\mathrm{n},0}, x_{\mathrm{n},1}, \ldots, x_{\mathrm{n,N\text{-}1}}]$ is given by

$$\mathbf{x}_{[}n] = \mathbf{F}_N^H \mathbf{s}[n], \tag{2.1}$$

where $\mathbf{F}_N^H$ is the N-point IDFT matrix, $\mathbf{s}[n] = [s_{\mathrm{n},0}, s_{\mathrm{n},1}, \ldots, s_{\mathrm{n,N\text{-}1}}]$ is the n-th transmitted symbol, and N is the block size. After the IDFT block, the CP is added, which as said before, is a copy of the last M samples of the IDFT output. The main function of the CP is to avoid the overlapping between consecutive CP-OFDM symbols. In the receiver side, the CP is discarded, and then, an N-point Fast Fourier Transform (FFT) is applied. In the absence of noise, the n-th received block $\hat{\mathbf{x}}[n] = [\hat{x}_{\mathrm{n},0}, \hat{x}_{\mathrm{n},1}, \ldots, \hat{x}_{\mathrm{n,N\text{-}1}}]$ is

$$\hat{\mathbf{x}}[n] = \mathbf{H}[n]\mathbf{s}[n], \tag{2.2}$$

where $\mathbf{H}[n]$ is the time matrix channel, formed by the elements of the channel impulse response during the n-th block interval. Fig 2.1 shows the block diagram of a CP-OFDM transceiver.

Despite having many positive aspects, OFDM has a fundamental characteristic that makes it unattractive for new mobile communication systems, and

it is that the entire frequency band of the OFDM signal is digitally filtered as a whole, in order to meet the spectral specifications. Additionally, in an OFDM system each subcarrier is shaped using a rectangular window in time domain, resulting into sinc-shaped subcarriers in the frequency domain. Due to the peculiarities of the sinc function one of the main characteristics of OFDM, such as the division of the spectrum into multiple parallel orthogonal sub-bands with the highest possible spectral efficiency, is only fulfilled under perfect circumstances (perfect frequency synchronization and perfect time alignment for the duration of the cyclic prefix).

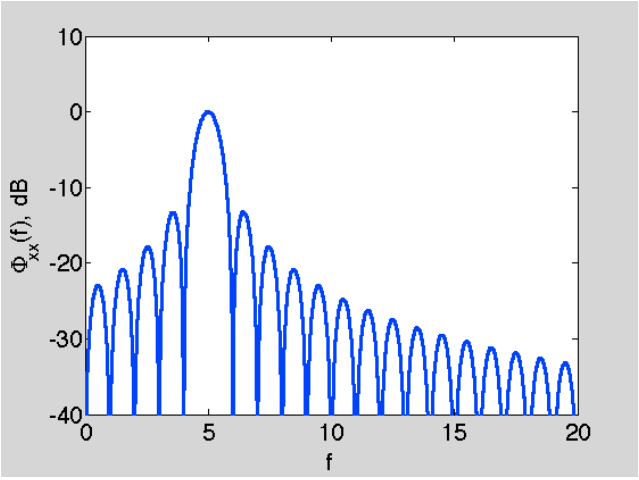

Figure 2.2: OFDM subcarrier power spectral density [63]

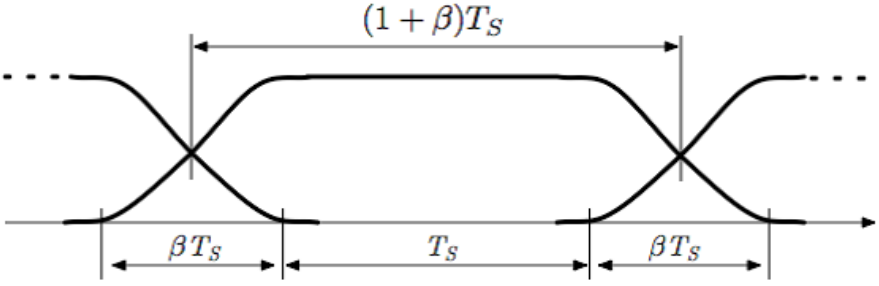

Figure 2.3: Time domain smooth windowing [63]

Another of the OFDM disadvantages of sinc-shaped subcarriers is the small power difference between the primary and secondary lobes. This is easily visible by looking at Figure 2.2, where the power spectral density of an OFDM subcarrier is shown. Figure 2.2 also shows that the first secondary lobe is approximately at -15 dB, which is still a considerable level to interfere with adjacent subcarriers. An alternative to increase the difference between the main lobe and the secondary lobes, is to apply a smooth windowing instead of a rectangular one, as presented in Fig 2.3. By making smooth transitions, the duration of each OFDM symbol is increased from T_s to $(1 + \beta)T_s$, where β is the increment factor and is inversely proportional to the slope of the transition. This makes necessary to include a CP and guard bands, introducing a signaling overhead to the system, and reducing the spectral efficiency and the amount of services that can be attended.

In addition to the aforementioned, another of the CP-OFDM problems is its high out-of-band (OOB) leakage, which makes the system more sensitive to frequency distortions like phase noise and Doppler, causing the necessity of using large guard bands. For high mobility or asynchronous users, is very likely that the system performance is affected by the resulting Inter-Carrier Interference (ICI). Furthermore, every multicarrier waveform has to deal with high Peak-to-Average Power Ratio (PAPR). That is why there are different solutions that provide some enhancements to classical OFDM, in order to overcome all this drawbacks and address the requirements for 5G wireless systems.

2.1.1 Harmonized/flexible CP-OFDM

Changing physical layer parameters (i.e. subcarrier spacing, frequency, number of subcarriers, etc.) provides the opportunity to adapt the characteristics of the system, and thus prepare for a specific scenario. For instance, by choosing a proper subcarrier spacing, the Doppler and sensitivity to phase noise can be handled. Both effects increase as a function of frequency, so with the aim of making an OFDM system robust against them, is possible to use larger subcarrier spacing at higher frequencies. This changes in the CP-OFDM numerology are the option chosen by the 3GPP, so this will be reviewed more deeply in chapter 5.

2.1.2 Universal Filtered MultiCarrier (UFMC)

UFMC is a waveform considered as an enhancement of CP-OFDM, combining its base structure and a frequency domain efficient post-filtering, which is carried out over a group of consecutive subcarriers with the aim of reducing

the OOB leakage, and ICI between adjacent users when using asynchronous transmission [27]. Applying this filtering results in a shorter time domain impulse response, and allows to rule out the use of CP. All this makes UFMC spectrally more efficient than CP-OFDM according to [64, 65], since it allows to reduce the guard bands in contiguous channels. Since the smallest unit used in LTE for scheduling purposes is a Resource Block (RB), which is a subgroup of 12 contiguous subcarriers, UFMC takes advantage of that feature to carry out a subband filtering over a RB. It's important to notice that although the transmitted signal doesn't have a CP, there's a spectral efficiency loss due to the time transient (tails) of the filter.

For a particular multicarrier symbol of user k, the time-domain vector $\mathbf{x}_k$, is the superposition of the subband filtered components $\mathbf{x}_i$, where $i = 1, \ldots, B$; B is the number of subbands; the filter length is L; and N is the FFT length:

$$\underset{[(N+L-1)\times 1]}{\mathbf{x}_k} = \sum_{i=1}^{B} \underset{[(N+L-1)\times N]}{\mathbf{F}_{ik}} \underset{[N\times n_i]}{\mathbf{V}_{ik}} \underset{[n_i\times 1]}{\mathbf{s}_{ik}} \tag{2.3}$$

The IDFT matrix $\mathbf{V}_{ik}$ is formed by the relevant columns of the inverse Fourier matrix, which correspond to the matching subband within the complete frequency range, and it's responsible for the time-domain conversion of the $\mathbf{n}_i$ complex Quadrature Amplitude Modulation (QAM) symbols, for each of the B subbands, which are indexed with i. $\mathbf{F}_{ik}$ is a Toeplitz matrix built by the filter impulse response and is in charge of performing the linear convolution. Is important to notice that UFMC has no time overlap between subsequent symbols, and that the symbol duration is determined by the FFT size and the filter length, i.e., $N + L - 1$. This can be best appreciated in the block diagram shown in Figure 2.4. Filtering by subcarrier blocks or Physical Resource Block (PRB) provides additional flexibility, which result in pass band broad filters and therefore shorter in time. Having shorter times is a feature that can be used to reduce the filter length. This also allows short bursts to be supported, as well as operation in fragmented bands. On the other hand, the suppression of secondary lobes now works between subbands, instead of between subcarriers, which can be observed in Figure 2.5, where a comparison between the power spectral density of UFMC and OFDM is shown.

On the receiver side it's necessary to apply a time processing stage (such as windowing and a serial to parallel conversion), then the samples are zero-padded to apply a $2N$ size FFT. After this, the symbols are obtained by decimation. However, despite the many attempts around this approach, it was not possible to get a functional transceiver this way. So, in order to recover

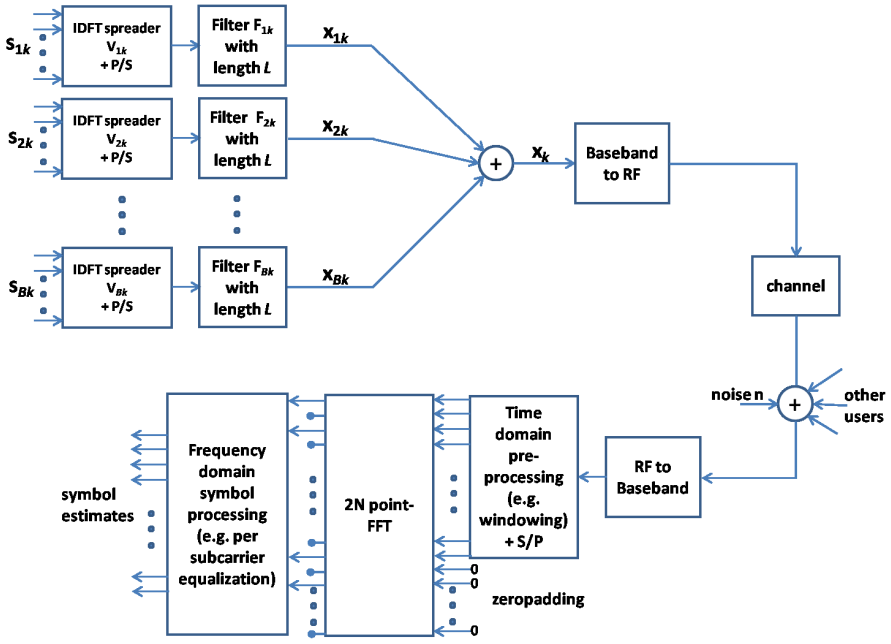

Figure 2.4: UFMC block diagram [37]

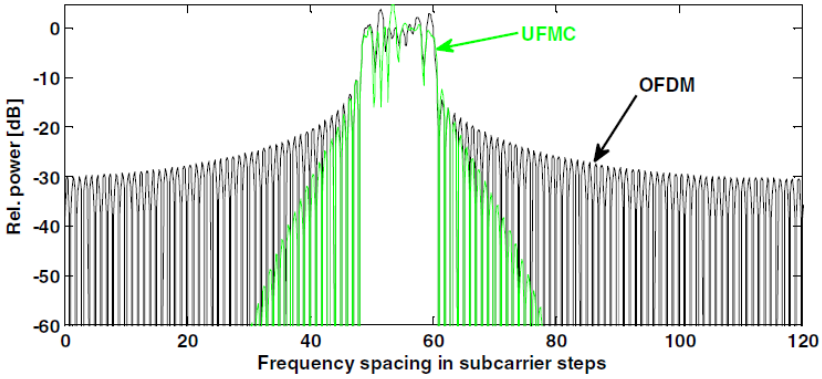

Figure 2.5: UFMC and OFDM power spectral density [37]

the signal, in this thesis the approach described in [66] and showed in Figure 2.6, was the one used. Here, a symmetric procedure is performed to recover the

signal; this means that the effect of the filter is removed and then the symbols are converted from time to frequency domain.

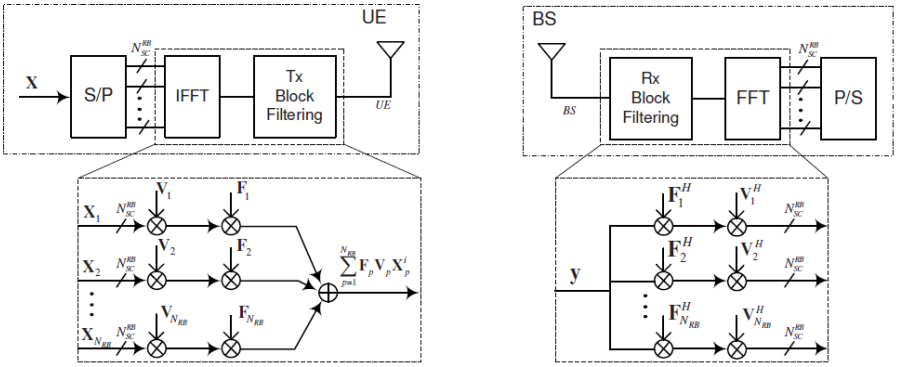

Figure 2.6: UFMC symmetric block diagram [37]

This is achieved by multiplying the signal received by the Hermitian transpose of each subband filter matrix, and subsequently by the Hermitian transpose of the IDFT matrix used in the transmitter. The reason for this is that for certain matrices, multiplying by its Hermitian transpose is equivalent to multiplying by its inverse. Although this is true with the IDFT matrix, this is not the case with Toeplitz matrices; so even if it is not specified in [66], with these matrices it is necessary to make a compensation, multiplying by the inverse of the multiplication between $\mathbf{F}_{ik}^H$ and $\mathbf{F}_{ik}$, as seen in Eq. (2.4). The received block symbol $\hat{\mathbf{x}_k}$ is given by Eq. (2.5):

$$\underset{[N\times N]}{\mathbf{T}} = inv\left(\underset{[N\times(N+L-1)][(N+L-1)\times N]}{\mathbf{F}_k^H \quad \mathbf{F}_k}\right) \tag{2.4}$$

$$\underset{[n_i\times 1]}{\hat{\mathbf{x}_k}} = \underset{[n_i\times N]}{\mathbf{V}_k^H}\underset{[N\times N]}{\mathbf{T}}\underset{[N\times(N+L-1)][(N+L-1)\times 1]}{\mathbf{F}_k^H \quad \mathbf{y}} \tag{2.5}$$

Moreover, it is important to highlight that UFMC is orthogonal with respect to the complex plane. Therefore, complex symbols can be used without having to deal with problems such as channel estimation degradation, as is the case with other waveforms. In addition, the filter ramp-up and down falls in time provide a symbol shape that protects the signal against Inter-Symbol Interference (ISI), as well as the robustness to support the access of multiple

users even if they are not perfectly aligned in time.

Another feature of UFMC is that it can be used with different filter times or with different subcarrier spacing for users in different subbands. For example, suppose user 1 uses an FFT size $N1$ and a filter length $L1$, while user 2 uses $N2$ and $L2$; even so, the durations of the UFMC symbols can be designed to be identical, enforcing that $N1+L1-1 = N2+L2-1$. This makes UFMC a modulation scheme with a very highly adaptability, which can easily be adapted to different aspects of the system, such as Doppler dispersion, user needs and radio channel characteristics. An example of a UFMC signal with 6 subbands is shown in Figure 2.7.

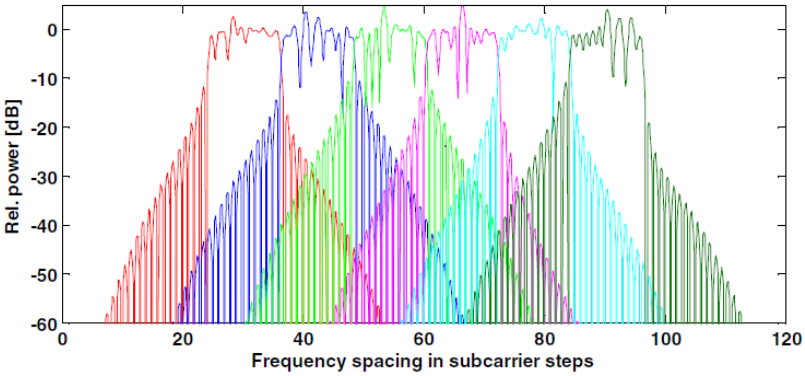

Figure 2.7: UFMC subband power spectral density [37]

In general, UFMC is a waveform capable of satisfying the wide range of requirements for 5G. For instance, a system using UFMC is able to adapt each subband according to the user needs, such as reducing energy consumption, support higher transmission throughput, lower latencies in the radio interface, etc. By doing this, the system can be scaled according to current needs, that is, it can be used in any type of device, whether high-end or low-end, slow or fast processing, without wasting resources, something that does happens with CP-OFDM where adaptation is only possible at symbol level, but not at subband level. Besides, instead of compromising between different needs (as occurs in LTE), a UFMC system is able to adapt to different needs, even improving the quality of user connections.

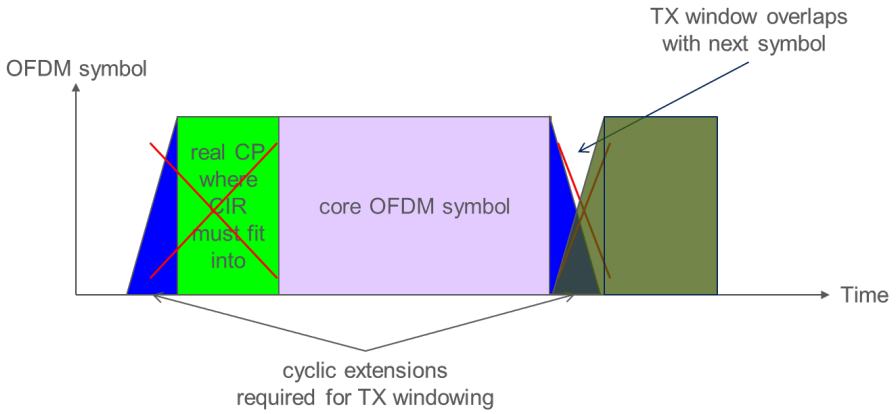

Figure 2.8: W-OFDM TX windowing [67]

2.1.3 Windowed-OFDM (W-OFDM)

Signal discontinuities at OFDM symbol boundaries are the main reason for the slow decay of OFDM spectrum, which is caused by the difference of phase and amplitude between contiguous symbols, since OFDM symbols are independent of each other. As explained at the beginning of this chapter, it is possible to apply a smooth windowing to the OFDM signal instead of a rectangular one, in order to deal with the difficulty of providing an appropriate frequency confinement with rectangular shaped symbols. By applying windowing, is possible to reach a containment of the subcarriers good enough to respect the transmission mask and simultaneously get a suitable spectral efficiency, and it can be applied at the Transmitter (TX) and/or the Receiver (RX).

In a system with windowing applied at the TX, symbols are softened on their borders with a smooth slope in time-domain. This slope can increase from 0 to 1, or decrease from 1 to 0, as seen in Figure 2.8. The decreasing slope is applied at the end of the OFDM symbol considering an extra added cyclic suffix, while the increasing slope is applied at the beginning of the CP. Something additional that can be appreciated in Figure 2.8 is how the decreasing slope overlaps with the increasing slope of the next OFDM symbol, which is possible since the windowed samples are discarded by the receiver keeping only the OFDM symbol, and because this overlapping helps to reduce overhead. It can be said that TX windowing is transparent to the receiver as it discards the guards and keeps only the symbol samples.

As previously stated, having sinc-shaped subcarriers produces some drawbacks, one of them being the high pick-up interference with other adjacent non-orthogonal signals, as can be the case of OFDM with different numerologies. By changing the rectangular OFDM window function to a smoother window, it is possible to reduce this pick-up interference. That is why in a system with windowing at the RX, a window is applied to the core of the OFDM symbol, that is, an increasing slope at the beginning of the OFDM symbol, before the CP; and a decreasing slope at the end of the OFDM symbol before the cyclic suffix.

In the Figure 2.9 you can see how when applying the window (cyan-colored line), it leaves out part of the OFDM symbol, both at the beginning and at the end of it (portions represented by the magenta and orange triangles in the upper corners of the core OFDM symbol). However, it is possible to recover this data thanks to the fact that the window also takes those same portions from the CP and the cyclic suffix, as can be seen in Fig 2.9. Once the OFDM symbol is reconstructed, the FFT is applied to continue with the process of data recovery. Pick-up interference is reduced with this procedure, as long as it does not have the same periodicity as the duration of the OFDM symbol.

2.1.4 Pulse Shaped OFDM (P-OFDM)

According to the general definition of an OFDM-based multicarrier system, the transmitted signal $\mathbf{x}(t)$ can be represented as:

$$\mathbf{x}(t) = \sum_{m=-\infty}^{+\infty} \sum_{k=0}^{N-1} \mathbf{X}_{(m,k)} g_{(m,k)}(t), \tag{2.6}$$

where m is the time index (the number of multicarrier symbols in the time dimension is assumed to be infinite), k is the subcarrier index, $\mathbf{X}_{(m,k)}$ is the modulated symbol transmitted at the k-th subcarrier and m-th multicarrier symbol (generally drawn from a set of complex numbers), N is the number of subcarriers with frequency spacing $\nu = 1/\tau$, and $g_{(m,k)}$ is the synthesis function, which maps the symbols $\mathbf{X}_{(m,k)}$ to the actually transmitted signal.

Likewise, the lattice that contains the coordinates in the time-frequency plane of a multicarrier signal is defined by the subcarrier spacing $F = (NT_s)^{-1}$ and the symbol period $T = MT_s$, where T_s is the sampling rate of the signal and M is the number of samples within one interval. To design P-OFDM is necessary to assume $M > N$, which would mean an overhead in the form of CP. This overhead is defined by $\vartheta = TF - 1 = \frac{M}{N} - 1 > 0$. Fulfilling these conditions guarantees the orthogonality of the signal, thus allowing compatibility

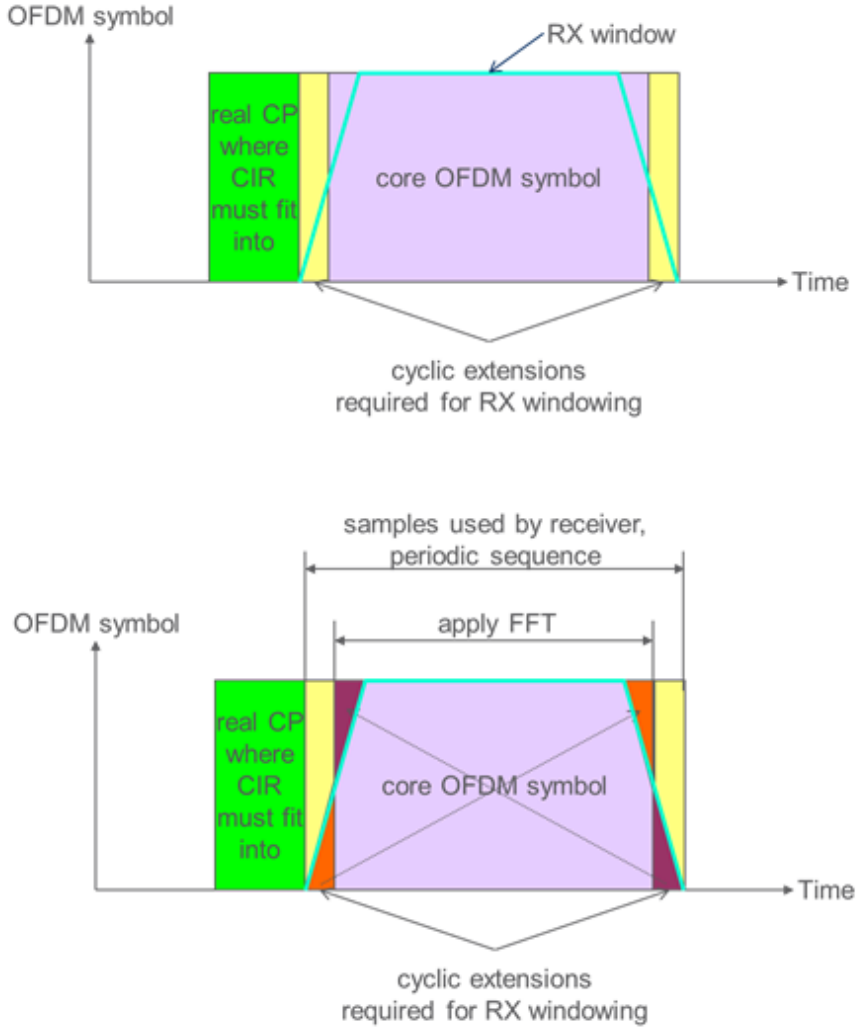

Figure 2.9: W-OFDM RX windowing [67]

with the techniques currently developed for OFDM.

On the other hand, the synthesis function $g_{(m,k)}$ can be expressed as:

$$g_{(m,k)}(t) = p(t - mT)e^{j2\pi k(t-mT)/\tau}. \tag{2.7}$$

$p(t-mT)$ is called the transmitter prototype filter (or pulse shape), and unlike CP-OFDM where the said prototype filter is designed as rectangular pulses, P-OFDM allows using different flexible pulse shapes besides to the rectangular pulse in order to balance the location of the signal power, both in the time and frequency domain; always maintaining the same CP-OFDM structure.

At the receiver side, to estimate the demodulated symbol $\hat{\mathbf{x}}_{(m,k)}$ it is necessary to correlate the received signal $\hat{\mathbf{x}}(t)$ with the receiver filter $\gamma_{(m,k)}(t)$:

$$\hat{\mathbf{x}}_{(m,k)} = \left\langle \mathbf{x}, \gamma_{(m,k)} \right\rangle = \int_{m=-\infty}^{+\infty} \mathbf{x}(t)\gamma^*_{(m,k)}(t)dt, \tag{2.8}$$

where $\gamma_{(m,k)}(t)$ is a time-frequency shifted version of the receive pulse $\gamma(t)$:

$$\gamma_{(m,k)}(t) = \gamma(t - mT)e^{j2\pi k(t-mT)/\tau}. \tag{2.9}$$

When the prototype filter applied in transmission and reception are the same, i.e. $p(t) = \gamma(t)$, this approach is considered as matched filtering [68]. However, it is possible to use different filters at the transmitter and the receiver, i.e. $p(t) \neq \gamma(t)$, which is known as mis-matched filtering. The difference between matched filtering and mis-matched filtering is that the former seeks to maximize the Signal to Noise Ratio (SNR) in an Additive White Gaussian Noise (AWGN) channel; while the latest provides robustness against ISI and ICI in dispersive channels, under the risk of suffering noise increment.

The general description of OFDM , defined in equation Eq. (2.6), does not limit the length of the prototype filter $p(t)$ to the symbol period T, as is the case with CP-OFDM; it only establishes as a requirement the orthogonality between subcarriers. This means that the pulse $p(t)$ could have a length $L = KT$ (where $K \geq 1$ is a rational number), which would mean that in the time domain there would be an overlap of a fraction of contiguous symbols. Provided that the orthogonality is respected in the design of the prototype filter, it will be possible to recover the signal without interference from the adjacent symbols, regardless of the K used for the design.

CP-OFDM is considered to be a special case of P-OFDM , where $K = 1$ and $p(t)$ is a rectangular pulse that performs the addition of the CP:

$$p_{cp}(t) = \begin{cases} \frac{1}{\sqrt{T}}, & t \in \left[-\frac{T}{2}, \frac{T}{2}\right] \\ 0, & \text{otherwise.} \end{cases} \tag{2.10}$$

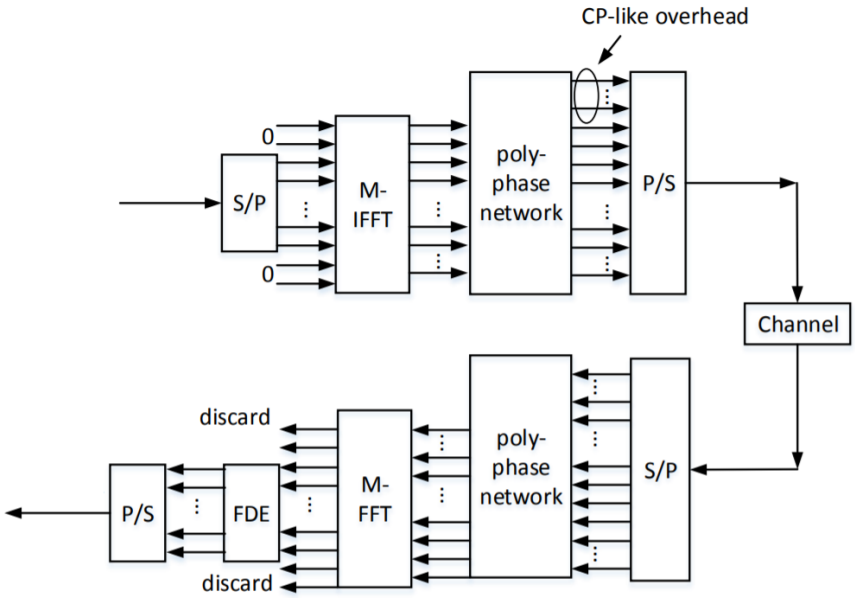

Figure 2.10: P-OFDM transceiver with efficient implementation of pulse shaping by a polyphase network [28]

In the receiver, the receive prototype filter is used to reconstruct the signal. In the case of CP-OFDM, $\gamma(t)$ is responsible for the removal of the CP:

$$\gamma_{cp}(t) = \begin{cases} \frac{1}{\sqrt{T-T_{cp}}}, & t \in \left[-\frac{T-T_{cp}}{2}, \frac{T-T_{cp}}{2}\right] \\ 0, & \text{otherwise.} \end{cases} \tag{2.11}$$

On the other hand, if $K \approx 1$ and a prototype filter with smoothed edges is used, then a W-OFDM signal is obtained as described in [69].

The complete structure of the P-OFDM transceiver is illustrated in Fig 2.10. As seen, it is possible to perform pulse shaping through a Polyphase Network (PPN) [70], for any overlapping factor K. For the case of short pulse shaping, such as when $K \approx 1$, the PPN structure can be simplified to windowing, CP adding, and CP removing operations. If $K > 1$, the PPN structure can be characterized as overlap add.

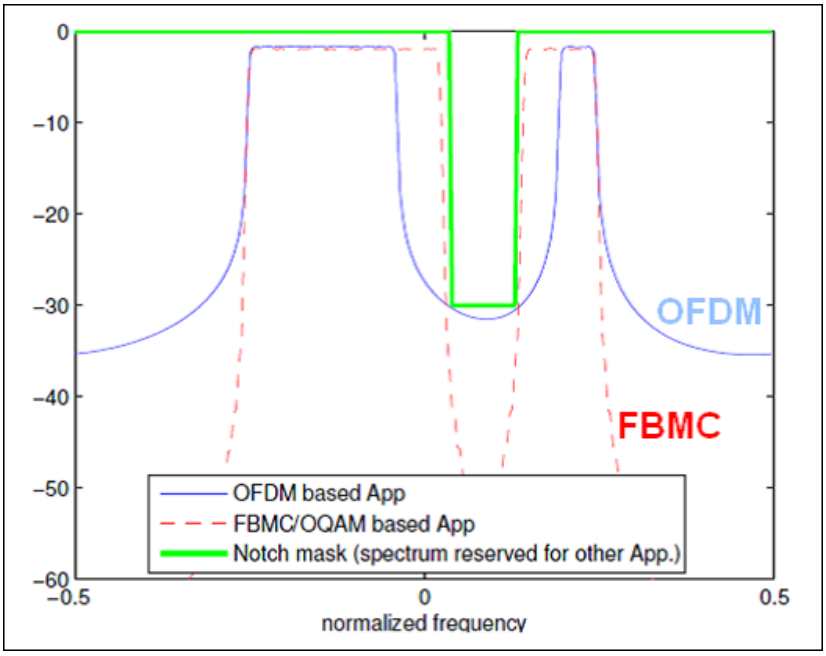

Figure 2.11: FBMC and OFDM power spectral density [37]

2.2 FBMC-based Solutions

While OFDM filters the entire band, and UFMC filters use sub-band filtering, in Filtered Bank Multi-Carrier (FBMC) the modulator implements a subcarrier filter, with a pulse of duration T, that may spread over several symbols. Thus, instead of using sinc shaped subcarriers, these have a more convenient shape depending on the filter design and with reduced secondary lobe levels; therefore, ICI problems are reduced.

The filters on each subcarrier are very narrow in frequency and therefore require quite large filter lengths (typically up to 4 times the basic length of each multicarrier symbol) causing complex symbols to overlap in time. However, designing the pulse orthogonally allows the overlapping symbols to be reconstructed almost perfectly without causing interference between them. Likewise, these filters require long ramp up and ramp down areas in case of bursty data transmissions.

By having reduced secondary lobes bands, and due to the orthogonal pulse design, FBMC does not need a CP and is therefore spectrally more efficient than OFDM or any other multicarrier scheme. The power spectral density of a FBMC signal compared to an OFDM signal can be seen in Fig 2.11.

At the time, two candidates from this family of waveforms were considered for the 5G: OQAM-FBMC and QAM Filter Bank Multicarrier (QAM-FBMC), which are described in the subsequent sections.

2.2.1 OQAM-FBMC

To maximize spectral efficiency, multicarrier symbols need to be staggered in time, which is achieved using Offset QAM (OQAM). OQAM consists of dividing the complex symbols (QPSK, xQAM) into a real and imaginary part, then applying a time offset of half symbol interval to both components, and finally modulating them as consecutive symbols. By doing this, a structure in the shape of a chessboard is built, in which the real and imaginary symbols are located, alternating in time and frequency. Since no guard bands are required, the maximum spectral efficiency of $TF = 1$ is obtained. However, the orthogonality of OQAM exists only in the real part, therefore many of the algorithms developed for OFDM are not directly applicable and require some adaptation in terms of signal processing.

Fig 2.12 shows the block diagram of a FBMC transceiver. As seen, FBMC does not require CP, therefore in the transmitter, after applying the FFT, filter banks are used to realize the prototype filter according to the desired design. The entire FBMC modulation/demodulation process can be effectively performed with FFT and polyphase filtering. If the complexity of the entire FBMC transceiver block is compared with OFDM one, the latest research car-

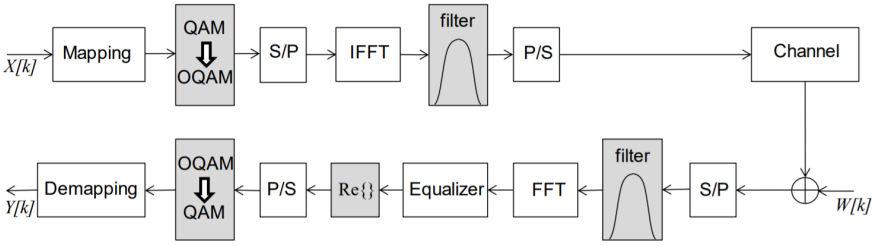

Figure 2.12: FBMC transceiver [67]

ried out showed that the additional complexity required to perform subcarrier filtering is only moderate.

2.2.2 QAM-FBMC

There are some determinant parameters in terms of spectral efficiency, e.g., the block length. In the case of OQAM-FBMC, it is possible that for the uplink a small guard interval is needed once per block due to the filter tails, in order to avoid ISI. Therefore, OQAM-FBMC loses efficiency in cases with short blocks. However, when it comes to blocks with long lengths, OQAM-FBMC would be more efficient than OFDM since the CP or its guard bands are longer than the guard interval of OQAM-FBMC due to the filter tails. Also, due to the low OOB emissions of OQAM-FBMC, the guard bands at the edges of the spectrum can be smaller.

These characteristics make FBMC an attractive waveform for asynchronous scenarios, where technologies such as CoMP and Dynamic Spectrum Access (DSA) are used to meet the high traffic demand expected in 5G. FBMC handles multipath fading well even without CP, thanks to its increased symbol duration.

However, when using OQAM, the regular FBMC system doubles the lattice density compared to OFDM, either in time or in frequency. This is due to the separate mapping of the real and imaginary components of each symbol, which causes inherent interference and makes typical pilot designs and subsequent channel estimation algorithms not directly applicable, just like MIMO schemes. Because of these reasons, QAM-FBMC became a suitable option, since transmitting QAM symbols allows improving spectral efficiency while maintaining low processing complexity, using improved algorithms for channel

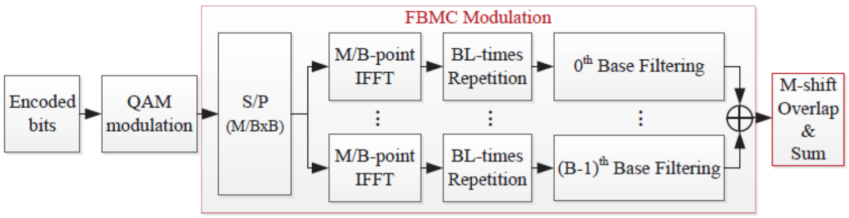

Figure 2.13: QAM-FBMC transceiver [67]

estimation and equalization in order to combat multipath fading.

Fig 2.13 shows the block diagram of a QAM-FBMC system with two different pulse shaping for the even and odd-numbered carriers. First, the symbols are split according to their numbering, that is, even and odd. Then the IFFT is applied to them and the output is repeated. Finally, the signal is pulse shaped by the two prototype filters and added. QAM-FBMC maintains the same symbol rate as CP-OFDM.

On the receiver side, the received symbols are FFT applied and equalized in the frequency domain. They are then filtered by the RX filter for even subcarriers, and due to the orthogonality properties odd-numbered subcarriers symbols are eliminated. The same happens when passing through the RX filter for odd subcarriers. After that, each symbol is filtered by the prototype filter and then demodulated.

2.3 Conclusions

In this chapter, some of the multicarrier waveforms that were the most popular candidates for 5G at the time, have been described. Among them are CP-OFDM,P-OFDM, UFMC, W-OFDM, OQAM-FBMC, and QAM-FBMC; all of them with high spectral efficiency, either by itself or thanks to enhanced algorithms. All listed waveforms are compatible with MIMO algorithms, except for OQAM-FBMC which as previously stated is not directly compatible with the conventional algorithms used for CP-OFDM, that is, it requires additional mechanisms to work properly.

All waveforms have their advantages and disadvantages compared to each other; however, it is important to emphasize two things. First of all, none of them is capable of supporting all the requirements of 5G on its own, since there is always a trade-off between the most relevant characteristics. And on the other hand, none of the contenders presents a considerable superiority over CP-OFDM that cannot be compensated with different mechanisms.

In terms of time location, CP-OFDM has the best performance and also has the lowest baseband complexity, although on the other hand, it has a high OOB leakage. This OOB leakage can be mitigated using mechanisms such as pulse shaping/filtering/windowing, just like it happens with P-OFDM, UFMC, W-OFDM, OQAM-FBMC, and QAM-FBMC. Although all these waveforms present a certain level of improvement in terms of frequency localization, it

happens at expenses of additional complexity and losing time localization. It should be noted that time localization is important for scenarios that require low latency, and also for Time Division Duplexing (TDD) transmissions; while the frequency localization is important when asynchronous transmissions are required, as is the case of D2D communications. Although it would be advisable to use waveforms with good frequency localization (P-OFDM, UFMC, W-OFDM, OQAM-FBMC, and QAM-FBMC), it is possible to use CP-OFDM with band guards, obviously with the cost of losing spectral efficiency.

There is a disadvantage that all multicarrier waveforms have in common, and that is the high PAPR, which grows according to the number of subcarriers used per symbol. This affects especially the battery consumption of the User Equipment (UE).

Chapter 3

Waveform Implementation and Comparison

This chapter explains in detail the implementation of three waveforms (CP-OFDM, UFMC, and OQAM-FBMC) in a Software Defined Radio (SDR) platform, analyzing their performance in terms of Bit Error Rate (BER). This testbed was framed within the research carried out by the METIS-II project, that is why the waveforms chosen were these three, since at that time all the research activities carried out by the members of METIS-II were oriented towards these waveforms. In addition, a performance comparison is made in a Vehicle-to-vehicle (V2V) environment, in order to evaluate which of them would best fit in this context.

With this aim, this chapter has been divided into the next sections:

- Section 3.1 details the implementation of the waveforms.
- Section 3.2 includes the performance comparison in a V2V environment.
- Section 3.3 draws the main findings of this study.

3.1 Waveform Implementation

This section describes the methodology used for the implementation and subsequent evaluation of the performance of UFMC and OQAM-FBMC compared to CP-OFDM, in a in an SDR platform.

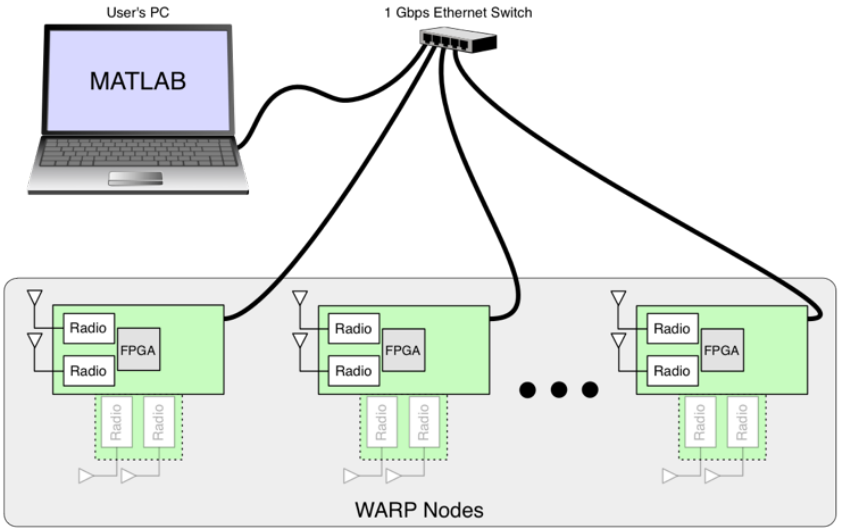

Figure 3.1: WARPLab platform schematic

3.1.1 Software Defined Radio Platform: WARPLab

WARPLab is a platform for the implementation of physical layer prototypes, which allows coordination between arbitrary combinations of transmitter and receiver nodes, whether they use one or more antennas. Being an extensible platform, WARPLab offers users the flexibility to develop and deploy large sets of nodes, in order to satisfy any application or any requirement to carry out an investigation. Its operating scheme can be seen in Fig 3.1.

One of the important aspects of WARPLab is its reference design, which allows the generation and processing of I/Q samples in MATLAB. In this way, the user can choose between using the reference design and focusing exclusively on MATLAB code; or if required, modify the reference design or replace entire parts of it. Also, the reference design combines MATLAB code with Field-programmable Gate Array (FPGA) implementations, allowing for easy extensibility and customization. In other words, while MATLAB executes control over the nodes and performs signal processing, the FPGA is in charge of executing applications with strict latency requirements and time critical processes.

The hardware implementation used for this thesis consisted on two WARP v3 kits connected to each other and to the computer running MATLAB through a switch, as seen in Fig 3.2. Among the main components of the WARP v3 kit are its main processor, which is a Xilinx Virtex-6 FPGA, in which physical layer algorithms can be implemented to work in real-time; and the two radio interfaces that allow data to be sent between the two nodes. These and the other components of the WARP v3 kit can be detailed in Fig 3.3.

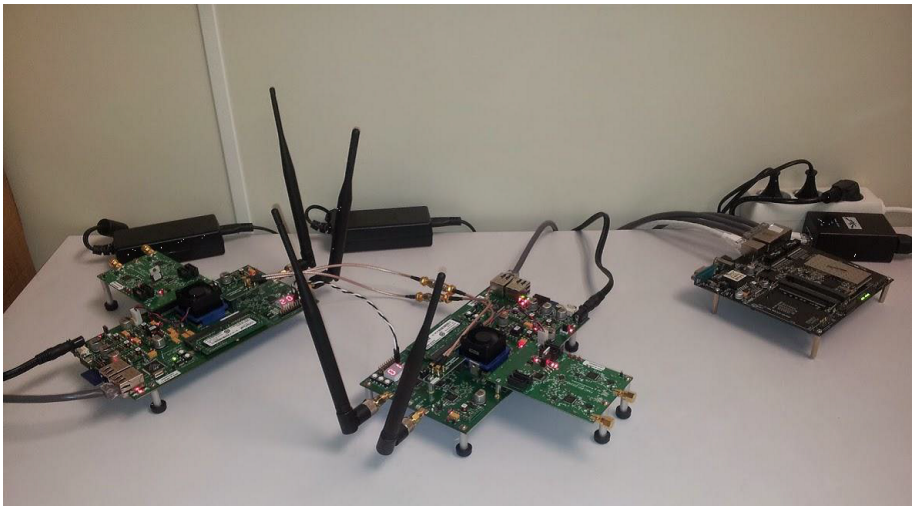

Figure 3.2: SDR scheme used for waveform implementation

3.1.2 MATLAB Code Implementation

For the implementation of UFMC and OQAM-FBMC in MATLAB, one of the examples provided by WARPLab was taken as a starting point to get familiarized with the kit configuration commands, as well as the commands that allow data transmission and reception. In this example, an IEEE 802.11p signal is transmitted, which is an approved modification of the IEEE 802.11 standard that is used for wireless access in vehicular environments within a vehicular communication system, and uses CP-OFDM as a modulation scheme.

OFDM Code

The first thing is to establish the parameters of the OFDM signal inherent to the physical layer, such as the number of CP-OFDM symbols to be generated,

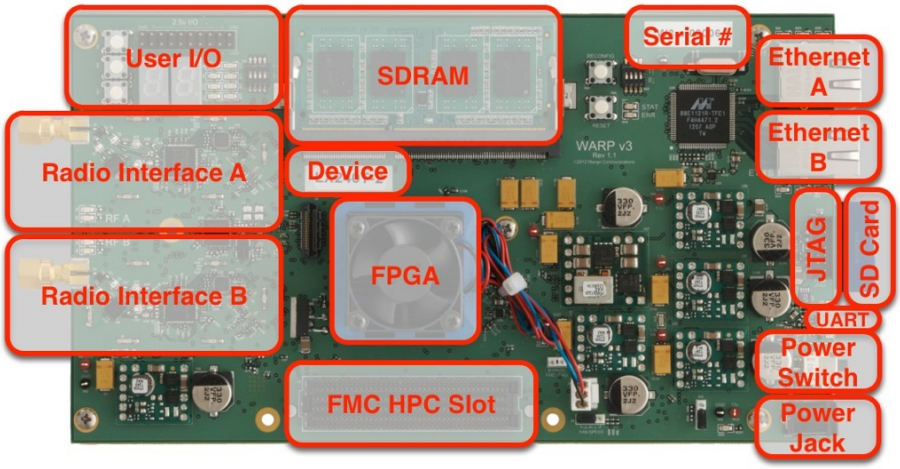

Figure 3.3: Main components of a WARP v3 kit

the total number of subcarriers, number of pilots, modulation order, length of the CP, among others. For this, it is necessary to look at the IEEE 802.11p standard. As can be seen in Fig 3.4, the CP-OFDM signal consists of 64 subcarriers in total, of these 48 are used for complex symbols (Binary Phase-Shift Keying (BPSK), Quadrature Phase Shift Keying (QPSK) or 16QAM) and are those represented in green, 4 are used to locate the pilot symbols and are those in red, while the remaining 12 are null and are located in the central band (from subcarrier 27 to 37) and in the first subcarrier.

From the same standard, the Short Training Sequence (STS) and the Long Training Sequence (LTS) are obtained, which constitute the preamble of the signal, and which will be used later in the receiver to synchronize the signal in time and to perform the channel estimation. The STS is a repetition of 10 equal short symbols of length 16 samples. The LTS comprises 2 identical sequences, of length 64 samples each, preceded by a 32-sample Guard Interval (GI). The synchronization process is split into a coarse Timing Offset (TO) and Carrier Frequency Offset (CFO) estimation based on the LTS, followed by a fine estimation. The coarse TO estimation is accomplished with the algorithm in [71], currently a standard algorithm in OFDM systems. This delay-and-correlate algorithm exploits the periodicity of the training symbols. The coarse CFO estimation is performed with the correlation algorithm in [71]. After this coarse estimation, subsequent samples are multiplied by the CFO error estimates. After that, the program obtains an exact starting point at the first sample of the

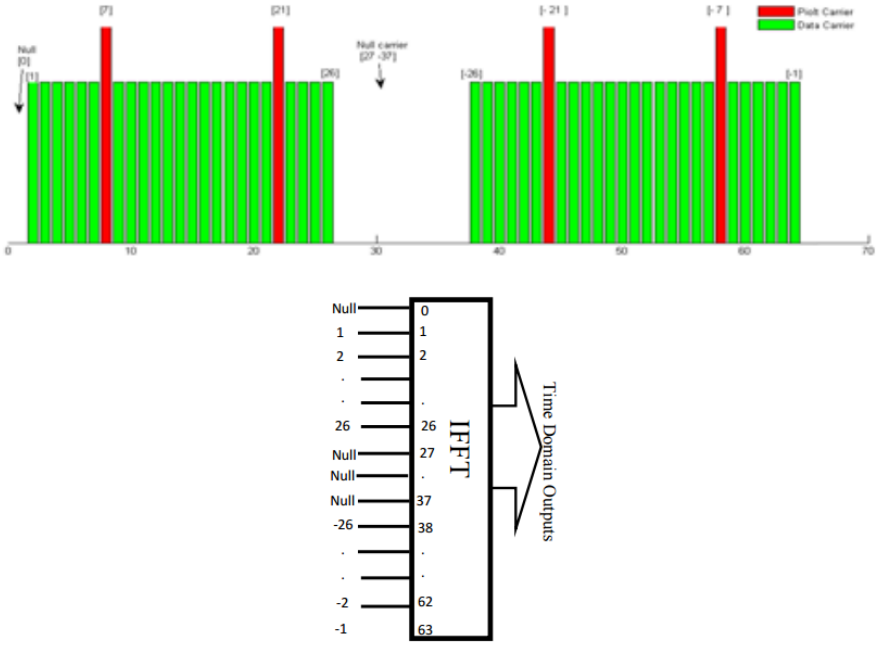

Figure 3.4: OFDM subcarriers assignment according to the IEEE 802.11p standard [73]

first LTS, which would be critical for the decoding process involving the FFT operation, moreover this starting point is useful because the LTS is also needed for channel estimation. This is achieved with cross-correlation or matched filter method, which correlates a local stored STS symbol with an already frequency-synchronized received signal. The output of the LTS correlator is a peak arising at the end of each of the two LTS symbols. The correlator implemented is a SignSign [72]. Fine carrier frequency offset estimation is performed with the aid of four pilot carriers.

The first thing is to configure the nodes, specifying if the Automatic Gain Control (AGC) will be used and the number of nodes that will be used. An User Datagram Protocol (UDP) trigger is also created, and it will start later

when the transmission begins. The sample frequency is read, as well as the maximum number of samples supported by the nodes. Finally, the transmission and reception interfaces are configured, establishing the gains and the operating band, which can be 2.4 GHz or 5 GHz, with its respective channel.

Once the OFDM matrix with the symbols allocated has been constructed, the IFFT is performed and the CP is added, which for this case corresponds to 16 samples in time. Then, the matrix is converted into a vector, which in turn is filled with zeros until the maximum number of samples is completed (32768). Finally, an interpolating filter is used to prepare the signal for transmission. In order to send the data from one node to another, the first step is to write the vector on the buffer of the transmitting node interface, then to enable the interfaces of the nodes, and finally fire the UDP trigger to indicate the interface that is the moment to transmit. To receive the data, the buffer of the receiving node is read and the interfaces are disabled.

On the receiver side, it is necessary to pass the received vector through a decimating filter that performs the opposite function to the interpolator used in the transmitter. A correlation algorithm is used to find the LTS sequence in the vector, and once is found it's used to synchronize the signal, that is, to find the beginning of the data and to perform the channel estimation. Once the data has been located, the Orthogonal Frequency Division Multiplexing (OFDM) matrix is assembled from the vector, the Cyclic Prefix (CP) is extracted and the Fast Fourier Transform (FFT) is performed. Subsequently, a zero-forcing equalization is carried out to the entire matrix, the pilots are extracted and with these, the phase error per symbol is calculated and corrected. Finally, the demodulation is carried out according to the order of modulation, and the calculations of the statistics are carried out, such as the Symbol Error Rate (SER), the BER, and the SNR.

UFMC Code

In the UFMC code, the configuration of the nodes, the configuration of the interfaces, and the procedure for transmission and receiving are exactly the same as that of OFDM; as well as the use of interpolator and decimator filters that are applied on the transmitter and receiver side, respectively. Therefore, the only thing that changes is the signal processing before transmission, and once it is received. As already stated, UFMC is a generalized form of OFDM. Consequently, it is possible to generate the UFMC signal from the OFDM matrix. Following the scheme of Figure 2.4, the first thing is to divide the OFDM signal into sub-bands (PRB's) that have a fixed number of subcarriers.

For this implementation the number of sub-bands is 8 sub-bands, and each of them is composed of 8 sub-carriers. Appendix A details the influence of these parameters on the performance, and the reason for these values is explained.

Once the signal has been divided into sub-bands, it's necessary to multiply each one of them by the corresponding columns of the IDFT matrix, and then by the filtering matrices of each sub-band. As mentioned in Section 2.1.2, the filtering matrices are Toeplitz matrices composed by a Dolph-Chebyshev filter located on each of the sub-bands. For the comparison between OFDM and UFMC to be equivalent, it must be true that $N + L_{CP} = N + L - 1$; where N is the number of subcarriers in the signal, L_{CP} is the length of the cyclic prefix, and L is the length of the filter. For this to be true, given that $L_{CP} = 16$, L must be equal to 17. The value of the rejection band chosen for the filter is 100 dB. With each of the sub-bands filtered in time, it only remains to add them in order to build the UFMC signal in time.

On the receiver side it is necessary to remove the filter effect and then convert the symbols from the time domain to the frequency domain. This is achieved by multiplying the received signal by the conjugate transpose of the filtering matrix of each sub-band, and subsequently by the conjugate transpose of the IDFT matrix used in the transmitter. The reason for this is that for certain matrices, multiplying by their conjugate transpose is equivalent to multiplying by their inverse. Although this is true of the IDFT matrix, it is not the case with Toeplitz matrices; so it is necessary to carry out an additional procedure, which consists of multiplying the filtering matrix by the inverse of the multiplication between the filtering matrix and its conjugate transpose. This is better explained in Section 2.1.2, specifically in equations Eq. (2.4) and Eq. (2.5).

Finally, as in OFDM, demodulation is conducted according to the specified modulation order and calculations of the SER, the BER, and the SNR are performed.

OQAM-FBMC Code

As with UFMC, the OQAM-FBMC code maintains the nodes configuration section, all the signal transmission and reception procedures, but changes the signal processing section. The first difference with UFMC is that the processing in OQAM-FBMC does not start from the OFDM matrix, but from the symbol matrix. To start, OQAM pre-processing is applied to the symbol matrix, i.e., the real and imaginary part of each complex symbol are separated and alter-

nate with an offset of half symbol interval, and then treated as consecutive symbols.

Once OQAM has been applied, the prototype filter that to be used for subcarrier filtering is built. In this case, the filter designed in the Physical Layer for Dynamic Spectrum Access and Cognitive Radio (PHYDAS) project [74] was used, which being one of the first filters proposed for FBMC is the most widely used filter. The design of the PHYDAS filter allows the use of overlap factor $K = 1, 2, 3, 4$, varying the number of coefficients in 1, 3, 5 and 7 respectively. With the filter already built, the filtering matrix is constructed. Subsequently, the symbol matrix is filtered, which is achieved by multiplying said matrix by the filtering matrix. The result will be the symbols filtered and oversampled K times. Finally, the IFFT is applied and the symbols are converted to the time domain.

On the receiver side, the signal is converted to the frequency domain through the IFFT and the filtering process is reversed, in order to do so, the symbols are simply undersampled according to the K factor. Then an OQAM post-processing is applied, merging the real and imaginary components of each complex symbol and reversing the offset.

Again, demodulation is conducted according to the specified modulation order and calculations of the SER, the BER, and the SNR are performed.

3.2 V2V Performance Comparison

IEEE 802.11p [75], also known as Wireless Access in the Vehicular Environment (WAVE), is an amendment to the IEEE 802.11 standard that extends its applicability to vehicular environments, including short-range communications for data exchange between vehicles (V2V) and between vehicles and the roadside infrastructure. IEEE 802.11p is based on OFDM, being its multiple access counterpart, Orthogonal Frequency Division Multiple Access (OFDMA), widely used to divide the spectrum in multiple and orthogonal parallel subbands, as it happens in LTE. But, as it turns out, the orthogonality property of OFDMA is only verified under ideal conditions, that is to say, under perfect frequency synchronization and precise time alignment during the CP. This issue imposes critical requirements, in such a way that, in order not to introduce ICI or ISI, the terminals should be prevented from transmitting if a central entity does not verify that both time and frequency alignment are being re-

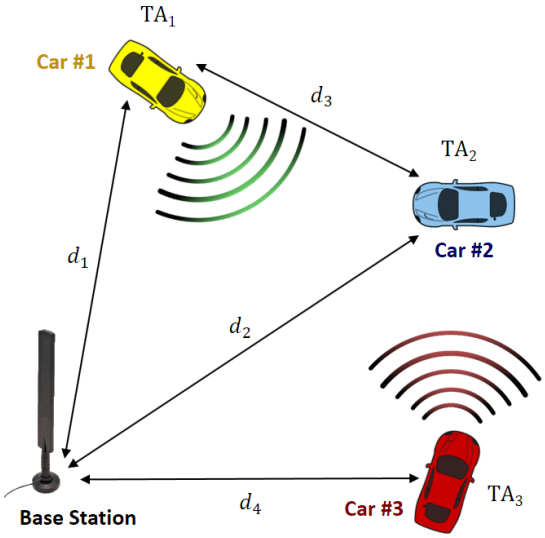

Figure 3.5: V2V case scenario

spected.

However, in the current design of LTE Vehicle (LTE-V) the synchronization requirements are becoming a crucial issue. For example, while vehicles may be synchronized with elements of the roadside infrastructure (i.e. base stations), it is not expected that the synchronism between vehicles in a V2V sidelink communication scenario would be supported by such elements; thus specific synchronization signals are now under discussion for the support of this direct V2V communication. Moreover, the concept of Timing Advance (TA) may not be reused because it only assists in the determination of the distance to a common element (the base station) and is useless when determining the distance between two vehicles with varying relative distances. Consequently, it is of the utmost benefit to assess alternatives to OFDM, which should be able to tolerate a lower degree of synchronization without introducing additional ICI or ISI.

3.2.1 V2V Scenario

This section explains the results of studying the effect of timing offset in OFDM, OQAM-FBMC, and UFMC systems with respect to the sidelink three-user sce-

nario depicted in Fig 3.5. As shown, the three vehicles are synchronized with respect to the base station via an ongoing closed-loop TA control enforced for each user in the uplink, thus anticipating the transmission so as to achieve perfect synchronization at the base station. TA is calculated as $\mathrm{TA} = 2d/c$, being d the distance in meters between the base station and the vehicle and c the speed of light. In addition, if opportunistic sidelink communications are allowed, vehicles are free to transmit data between them at will. Under such conditions, time-aligning each user before the transmission can start, is unacceptable, and thus supporting multiple concurrent V2V transmissions renders impossible for vehicles to be perfectly synchronized between them. In fact, asynchronous operation may be necessary to reach an acceptable level of spectral efficiency.

Assuming that vehicles lack a dedicated synchronization mechanism between them, only synchronizing with the base station and using the very same TA for their sidelink communications. In Fig 3.5, if car #1 and car #2 do not modify their TA, then the timing offset experienced at car #2 is $\mathrm{TO} = \mathrm{TA}_1 - \mathrm{TA}_2 + (d_3/c)$. Sidelink communication opportunities distributed in frequency (and/or time) mapped into adjacent frequency resources (and/or consecutive symbols) produce timing offsets that will be perceived by the receiver as multiuser interference.

Previous work has evaluated the impact of timing synchronization for OFDM systems (analytically [76], or jointly with simulations [77]); for OQAM-FBMC (either mathematically [78], or combining analytical evaluation and numerical simulations [79, 80]); and for UFMC (analysis and simulation [64]). Moreover, previous comparisons between waveforms have been done, again via numerical analysis and simulation: examining OFDM and FBMC [81], and studying OFDM, FBMC and UFMC (among others) [82]. This work complements the state of the art by assessing the impact of the timing offset by means of a hardware platform.

3.2.2 Waveform Comparison

This section shows a performance comparison of the studied waveforms. A total number of 1000 measurements per waveform have been performed using the PHY layer parameters of IEEE 802.11p shown in Table 3.1. In each case, the values of CP (OFDM), the overlap factor K (OQAM-FBMC), and sidelobe attenuation (UFMC) are explicitly stated in the figures. The modulation used is 16-QAM. Note that we refer in the legends to Dynamic OFDM (D-OFDM)

Table 3.1: Key 802.11p PHY layer parameters used

Parameters	IEEE 802.11p
FFT size	64
Total subcarriers	52
Data subcarriers	48
Pilot subcarriers	4
Symbol duration	8 µs
Guard interval	1.6 µs
FFT period	6.4 µs
Preamble Duration	32 µs
Subcarrier frequency spacing	0.156 25 MHz
Channel bandwidth	10 MHz
Band	5.9 GHz

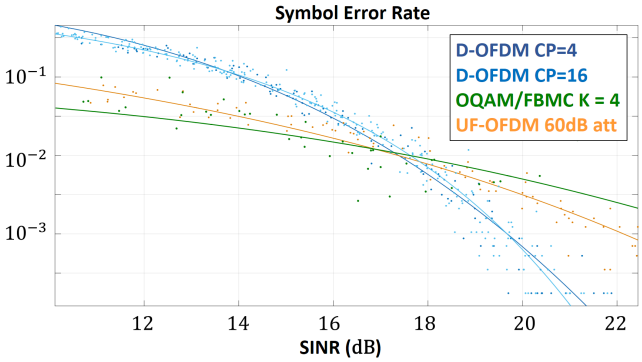

Figure 3.6: Symbol error rate with respect to the signal-to-interference-plus-noise ratio

to stress that, in this solution, CP can be modified dynamically to adapt to the different timing offsets.

The first results assume perfect synchronization between a transmitter and the base station in a Single Input Single Output (SISO) case. Fig 3.6 shows the symbol error rate with respect to the Signal to Interference plus Noise

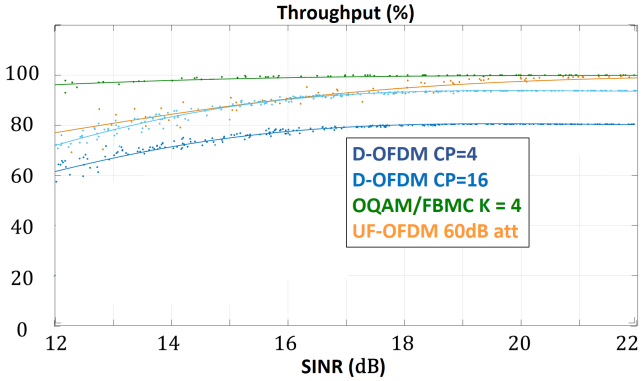

Figure 3.7: Throughput performance with respect to the signal-to-interference-plus-noise ratio.

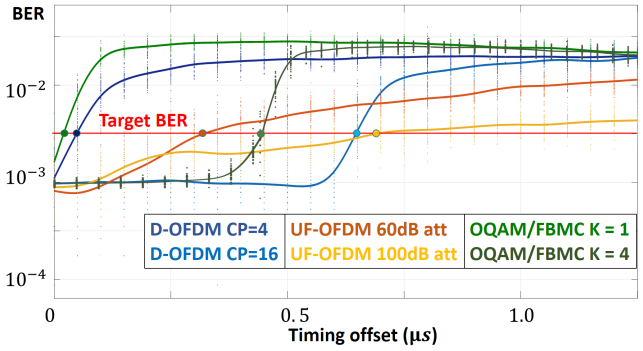

Figure 3.8: BER performance with respect to the timing offset. The target BER determines the highest tolerable timing offset.

Ratio (SINR) ratio. As shown in the figure, D-OFDM behaves better than OQAM-FBMC and UFMC for higher values of SINR while the opposite is true for lower values. Fig 3.7 shows the throughput counterpart. As shown, while OQAM-FBMC and UFMC achieve near 100% throughput, in the OFDM case the longer the CP the lower the throughput, because of the impact of the reduced spectral efficiency.

Next, the hardware testbed is used to mimic the sidelink communication scenario of Fig 3.5, where car #1 and car #3 are the transmitters and car #2 is the receiver; car #1 and car #3 transmit in the same carrier frequency but

on two distinct non-overlapping sub-bands (upper and lower, with 24 data carriers each). It is assumed that car #2 perceives car #1 transmission perfectly synchronized and car #3 transmission with a certain timing offset. The timing offset is adjusted in 50 ns steps, which correspond to a degree of unsynchronization of 1 sample. Fig 3.8 shows the BER performance with respect to the timing offset, where the target BER determines the highest tolerable timing offset. Note that, in case of OFDM, if car #3 transmission is misaligned its timing offset is equal to the relative delay to car #2. When the FFT operation is performed, car #2 may experience ISI and ICI from car #3 because if the OFDMA symbol of car #3 does not lie within the FFT window of car #2 the FFT duration may be extended over symbol boundary; and if the OFDMA symbol of car #3 lies within the FFT window it will be now less robust to delay spread of the channel. Note that the ISI and ICI from car #3 cause performance degradation also to car #1 transmission, which is perfectly synchronized. This multiple timing-offsets issue in an OFDMA uplink may be solved by increasing the CP duration, so that it covers both the longest transmission delay and the channel's maximum delay spread. As shown in Fig 3.8 the receiver can absorb small positive timing offsets (signal arrives later than the receiver expected) as long as the timing offset remains within the duration of the CP, approximately. However, OFDM performance degrades significantly as soon as the timing error is such that the channel transient exceeds the CP duration. Therefore the experimental results of the effect of timing errors on OFDM are in concordance with [76].

As shown in Fig 3.8, OQAM-FBMC exhibits a similar behavior and the signal is protected as far as the robustness provided by the overlap factor is not surpassed. In contrast, any timing offset in UFMC systems affects the system performance, since no CP is inserted. Even with a small timing offset, the orthogonality between subcarriers is destroyed, which causes ICI, and ISI. However, for UFMC the filter ramp-up and ramp-down may provide a soft protection against timing offset, since relatively small energy is contained, and as shown the degradation instead of sudden is progressive. This type of protection is also applicable to OQAM-FBMC, although the results shown in Fig 3.8 do not implement this mechanism.

3.3 Conclusions

The hardware testbed here presented is a valid framework for rapid physical layer prototyping, allowing arbitrary combinations of single and multi-antenna

transmit and receive nodes. Although implementing an OFDM waveform is less complex results show that OFDM is less robust against the lack of synchronization. However, there exist mechanisms that improve OFDM robustness (e.g. increasing the length of the CP or filtering, i.e. UFMC). On the other hand, OQAM-FBMC is more robust against the lack of synchronization, but not as easily applicable to MIMO since straightforward implementations of FBMC are more complex than OFDM. UFMC is also robust against timing issues and has a complexity similar to OFDM. In any case, we have highlighted the need for a software defined radio approach to provide more flexibility to accommodate sidelink communication..

Future work shall use the testbed to research the impact of mobility on the performance of FBMC, UFMC (as well as other waveforms investigated by METIS-II) and check their degradation, including a performance assessment when different modifications to the numerology of the waveforms are tested. Moreover, additional efforts should be made in order to harmonize the PHY layer with a single transmission chain that could implement a set of different waveforms.

Chapter 4

Waveform Harmonization

Nowadays, the standardization process of the fifth generation (5G) cellular systems is almost finished. Although there's still multiple research regarding the definition of the set of scenarios and requirements, the most important ones are already defined [83]. Within the 5G system, users with heterogeneous demands are expected to coexist, ranging from machine-type users that need ultra-reliable low-rate communications to classical mobile subscribers requiring communications of high data rate and broad coverage. Motivated by this, it has been identified, among other aspects, the need for multiple AI variants (AIVs) able to satisfy the demands of different types of users requiring communication at different bands, services and cell types [84].

A key aspect identified by academia and industrial stakeholders involved in 5G systems design is the integration of the different 5G AIVs into an adaptable and flexible 5G Air Interface (AI) [85]. Finding a one-fits-all solution for the AI is not certainly an easy (or even feasible) task, but a certain degree of protocol harmonization can be achieved by identifying the main similarities among AIVs and, at the same time, the main distinctive features of each of them. For instance, AI harmonization can be reached at a certain layer of the protocol stack, where multiple AIVs match, while keeping other layers independent. Overall, finding a harmonized AI is beneficial in order to save resources, reduce equipment complexity and communication delay and, also, to minimize standardization and implementation efforts for a new AIV integration [86].

This chapter addresses the harmonization of the AI physical layer, which was quite a promising approach at the time; more specifically, those that were the main 5G multi-carrier waveform candidates [87] and already described in

previous chapters, i.e., OFDM, P-OFDM, UFMC, W-OFDM, OQAM-FBMC, and QAM-FBMC. P-OFDM, W-OFDM, and OQAM-FBMC segment the spectrum into multiple orthogonal sub-bands and improve on CP-OFDM.

For their intrinsic design constraints, it comes as no surprise that each waveform has certain advantages and drawbacks that make them appropriate for specific operating circumstances [88]. CP-OFDM has a low complexity, straightforward implementation, as well as affinity with MIMO systems; however its suffers from signaling overhead because of the CP and from comparatively high OOB emissions. These issues justify why CP-OFDM cannot handle satisfactorily asynchronous or high mobility users and the proposal of new solutions like W-OFDM and P-OFDM. Filter bank-based waveforms do not require CP and achieve good spectral containment and better side lobe attenuation offering significantly enhanced capabilities when dealing with the interference produced by asynchronous transmissions; however the implementation complexity of filter banks is higher than that of CP-OFDM systems; MIMO is difficult and requires specific processing for channel estimation, pilots, and so forth. Thus, designing a comprehensive solution integrating these waveforms into a single harmonized implementation would advance the 5G physical layer towards providing flexible adaptation to a particular communication scenario at a reduced computational cost.

Many experimental testbeds including multiple waveforms have been developed [42, 44, 46, 89–94]. However, they mainly focus on dedicated implementations for isolated waveforms, without considering a versatile implementation able to generate different waveforms according to a harmonized framework with hardware reuse. In contrast to previous works, this approach propose a harmonized waveform implementation that is capable of reducing the overall complexity and memory usage with respect to multiple isolated waveform implementations. The harmonized implementation is based on Gabor systems [95], a mathematical tool to provide a general framework for multi-carrier systems, where different multi-carrier waveforms can be represented by selecting the appropriate prototype filter, subcarrier spacing and symbol spacing in time. A comprehensive survey on multi-carrier waveforms based on Gabor systems can be found in [96] and references therein.

Keeping this in mind, the main goal of this chapter is to provide a solution for waveform harmonization and demonstrate the advantages of using such harmonized implementation. Gabor representations will be used to describe the main building blocks of all the considered waveform implementations and subsequently evaluate the complexity of: a) each isolated waveform implemen-

tation and b) a harmonized waveform implementation for 5G. Therefore, the contribution of this work is twofold: a harmonized solution is proposed together with a thorough analysis of the complexity associated with the implementation of a number of waveforms either in an isolated manner or following the proposed harmonization solution.

Taking this into account, this chapter has been divided into the next sections:

- Section 4.1 analyzes the general framework for multicarrier waveform generation.
- Section 4.2 particularizes the description to the specific waveforms studied in this thesis.
- Section 4.3 summarizes the implementation details of the proposed harmonized transceiver design.
- Section 4.4 compares the complexity of all the waveforms presented.
- Section 4.5 compares the proposed harmonized system to the nonharmonized one.
- Section 4.6 outlines the most important conclusions of this study.

4.1 General framework

4.1.1 Transmitted signal

A multicarrier scheme is based on multiple subcarriers transmitted at the same time. Mathematically, the transmitted signal $\mathbf{x}(t)$ is expressed as:

$$\mathbf{x}(t) = \sum_{m=-\infty}^{+\infty} \sum_{k=0}^{N-1} \mathbf{x}_{(m,k)} g_{(m,k)}(t), \tag{4.1}$$

where m is the time index (the number of multicarrier symbols in the time dimension is assumed to be infinite), k is the subcarrier index, $\mathbf{X}_{(m,k)}$ is the modulated symbol transmitted at the k-th subcarrier and m-th multicarrier symbol (generally drawn from a set of complex numbers, although real numbers can be also considered as a special case), N is the number of subcarriers with frequency spacing $\nu = 1/\tau$, and $g_{(m,k)}$ is the synthesis function, which maps the symbols $\mathbf{X}_{(m,k)}$ to signal space, in order to constitute the transmitted signal. For this study, the time-frequency plane is considered as the signal

space, and hence the time and the frequency as its coordinates. Fig 4.1 shows how modulated pulses are placed into the lattice formed by the time-frequency plane, based on the locations of samples. The general multicarrier scheme is defined as a Gabor system [68] when $g_{(m,k)}$ has the form:

$$g_{(m,k)}(t) = p(t - mT)e^{j2\pi k(t-mT)/\tau}, \tag{4.2}$$

where $p(t - mT)$ is called the transmitter prototype filter (or pulse shape, or Gabor atom), and T is the multicarrier symbol period.

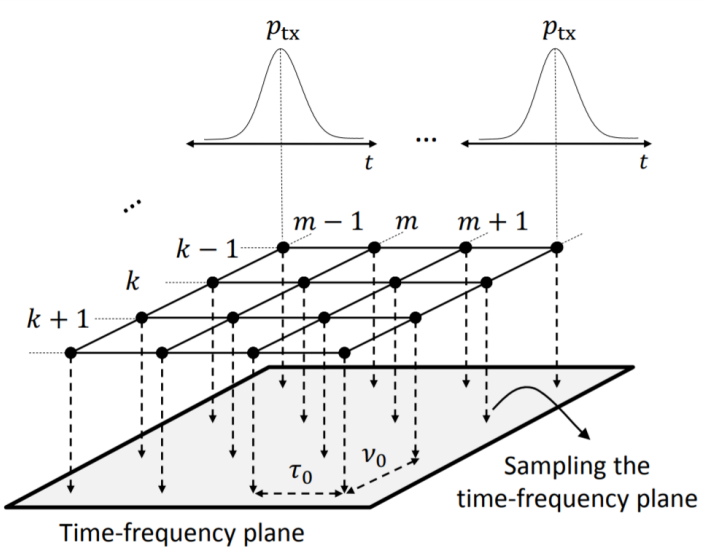

Figure 4.1: Lattice formed by the time-frequency plane [68]

Focusing on practical digital systems, the discrete-time version of the Gabor system describes the transmitted signal, denoted by $\mathbf{x}[n]$, which can be obtained by sampling with period T_s:

$$\mathbf{x}[n] = \mathbf{x}(nT_\mathrm{s}) = \sum_{m=-\infty}^{+\infty} \sum_{k=0}^{N-1} \mathbf{X}_{(m,k)} p\left[n - m\frac{T}{T_\mathrm{s}}\right] e^{jk(n-m\frac{T}{T_\mathrm{s}})\frac{2\pi T_\mathrm{s}}{\tau}}, \tag{4.3}$$

where $T/T_\mathrm{s} = N_\mathrm{T}$, is the length of the total symbol period in samples and the symbol duration has been expressed in terms of T_s as $\tau = NT_s$. The discrete-time version of the prototype filter $p[n] = p(nT_\mathrm{s})$ has length $L = KN_\mathrm{T}$, with K

standing for the overlapping factor, where the n-th sample belongs to the s-th symbol, $\{n, s \in Z\}$; being $s = \lfloor n/N_{\mathrm{T}} \rfloor$, where $\lfloor x \rfloor$ denotes the floor function, that is, the largest integer less than or equal to x. When $T/T_{\mathrm{s}} = N$ the filter bank is said to be critically sampled; when $T/T_{\mathrm{s}} < N$ the filter bank is said to be noncritically sampled (oversampled).

Renaming $i = n - mN_{\mathrm{T}}$, the prototype filter $p[i]$ has the following form:

$$p[i] = \begin{cases} p_i \in \mathbb{R}, & \text{if } 0 \leq i \leq KN_{\mathrm{T}} - 1 \\ 0, & \text{otherwise.} \end{cases} \tag{4.4}$$

where real-valued filter coefficients (i.e., symmetric filters in the frequency domain) are generally considered. Note that the waveform exhibits overlapping in time between consecutive symbols because, from the prototype filter definition, $p[n - mN_{\mathrm{T}}] \neq 0$ when $(m+1)N_{\mathrm{T}} \leq n \leq (m+K)N_{\mathrm{T}} - 1$, and hence, in this context, K is called the overlapping factor.

4.1.2 Received signal

Reconstructions of the modulated symbols originally transmitted from the received signal $\mathbf{x}[n]$, denoted as $\hat{\mathbf{X}}_{(m,k)}$, may be achieved by reverting the operations performed at the transmitter as follows:

$$\hat{\mathbf{X}}_{(m,k)} = \sum_{n=-\infty}^{+\infty} \mathbf{x}[n] e^{-jk(n-mN_{\mathrm{T}})\frac{2\pi T_{\mathrm{s}}}{\tau}} p^*[n - mN_{\mathrm{T}}] + w[n], \tag{4.5}$$

where $w[n]$ are statistically uncorrelated samples of an AWGN. Note that the signal detection operation involves convolving the received signal with a conjugated time-reversed version of the prototype filter and, thus, it is equivalent to matched filtering. Also note that if the prototype filter is real, the presence of the conjugation is irrelevant. For simplicity reasons, the effects induced by a linear time-varying multipath channel, propagation delay, and clock discrepancies between transmitter and receiver are ignored. In general, even in the presence of a noiseless channel, $\hat{\mathbf{X}}_{(m,k)} \neq \mathbf{X}_{(m,k)}$ because only multicarrier waveforms designed to guarantee appropriate time and frequency domain orthogonality avoid the effects of ISI and/or ICI.

4.2 Multicarrier waveforms

4.2.1 CP-OFDM variants

The well-known CP-OFDM multicarrier waveform is based on including a CP as a guard time interval to reduce or completely remove the effect of ISI. This CP is added after the filter bank, as it will be later elaborated. Conveniently, the discrete domain of Eq. (4.3) makes adding a CP possible by increasing in N_{CP} samples the total size of the multicarrier symbol $N_{\mathrm{T}} = N_{\mathrm{CP}} + N$, and adjusting at the receiver the offset position of the reception window accordingly [97]. Moreover, for the sake of waveform harmonization, CP-OFDM variants may be conceived as increasingly particular cases of Eq. (4.3), as it will be further elaborated below.

P-OFDM

A generic P-OFDM scheme follows the general signal structure of Eq. (4.3) and allows the use of flexible pulse shapes to balance the time and frequency domain localization of the signal power [98]) but including also the use of a CP to counteract ISI. P-OFDM allows the pulse shape to extend over the symbol period, rendering successively transmitted symbols to overlap. The transmitted signal is given directly by Eq. (4.3) and its prototype filter by Eq. (4.4).

W-OFDM

W-OFDM is essentially the name of a CP-OFDM system with a time-domain (non-rectangular) smoothing window that is used in most cases to suppress sidelobes, thus improving frequency localization at the expense of a minor increase in complexity and a reduction in time domain localization. As such, a W-OFDM signal can be seen as a P-OFDM signal with a short pulse shape, i.e. that expands over $K \approx 1$ symbol intervals. A window of length $K \approx 1$ may be built from a window of length $K = 2$ and proper zero-padding. Therefore, all the mathematical details from P-OFDM also hold for W-OFDM.

CP-OFDM

CP-OFDM is a particular case of W-OFDM where the pulse shapes are built on rectangular prototype filters. Simplifying Eq. (4.3) further, the samples of a CP-OFDM symbol may be expressed as:

$$\mathbf{x}[i + mN_{\mathrm{T}}] = \sum_{k=0}^{N-1} \mathbf{X}_{(m,k)} p[i] e^{jki(2\pi/N)}, \tag{4.6}$$

with $\{m, i \in Z \mid 0 \leq i \leq N_{\mathrm{T}} - 1\}$ and where the non-overlapping succession of CP-OFDM symbols simplifies the sum over m.

The prototype filter adds the CP:

$$p[i] = \begin{cases} \frac{1}{\sqrt{N_{\mathrm{T}}}}, & \text{if } 0 \leq i \leq N_{\mathrm{T}} - 1 \\ 0, & \text{otherwise.} \end{cases} \tag{4.7}$$

4.2.2 FBMC variants

FBMC systems divide the spectrum into several narrow subchannels to try to address the main drawbacks of CP-OFDM: the loss in spectral efficiency because of the CP insertion, the higher OOB emissions, and the higher sensitivity to narrowband interference. Since FBMC subcarriers are optimally designed in the frequency domain to emphasize spectral compactness, these waveforms do not need a CP and thus are more spectral efficient. These properties make FBMC a good alternative for narrowband machine-type communications. It could bring more efficiency to these services while alleviating the synchronization requirements on the devices. This section is focused on two alternative multicarrier waveforms based on the FBMC concept.

QAM-FBMC

The Gabor system expression $\mathbf{x}[n]$ for the critically sampled version of the well-known scheme called QAM-FBMC (That is, $T_{\mathrm{s}} = \tau/N$, the sampling period is such that the number of samples per multicarrier waveform symbol is exactly the number of subcarriers and then $T = NT_{\mathrm{s}}$) may be produced from Eq. (4.3) by removing the CP, i.e. $N_{\mathrm{T}} = N$, as follows:

$$\mathbf{x}[n] = \mathbf{x}(nT/N) = \sum_{m=-\infty}^{+\infty} \sum_{k=0}^{N-1} \mathbf{X}_{(m,k)} p[n - mN] e^{jk(n-mN)(2\pi/N)}. \tag{4.8}$$

In such scheme, the transmit signal is built from the N parallel streams, where the m-th data symbol in the k-th branch $\hat{\mathbf{X}}_{(m,k)}$ is accordingly selected from a QAM symbol constellation. QAM-FBMC is an orthogonal scheme where the prototype filters enjoy good frequency localization, which is obtained by using non-overlapping guard bands between the subcarriers in the frequency domain, leading to ICI reduction at the expense of some loss in bandwidth efficiency. The scheme typically uses a real-valued low-pass FIR filter like the one in Eq. (4.4), but with length $L = KN$.

OQAM-FBMC

An alternative to QAM-FBMC is to use the Staggered Multitone (SMT) scheme where prototype filters with overlapping impulse responses fulfilling the Nyquist ISI criterion are applied [99]. In this case, OQAM modulation is used, which transmits the real and imaginary parts of the data separately with a time offset duration of half of a symbol. As a result, the symbols to transmit are real numbers. Before the transmission, the symbols are overlapped such that they can be separated at the receiver. The imaginary parts include a time offset with respect to the real ones. Modifying Eq. (4.8) accordingly results in:

$$\mathbf{x}[n] = \sum_{m=-\infty}^{+\infty} \mathbf{x}_{\Re}[n]p[n - mN] + \mathbf{x}_{\Im}[n]p[n - mN - N/2] \tag{4.9}$$

with

$$\begin{aligned} \mathbf{x}_{\Re}[n] &= \sum_{k=0}^{N-1} \theta_k \Re\{\mathbf{X}_{(m,k)}\} e^{jk(n-mN)(2\pi/N)}, \\ \mathbf{x}_{\Im}[n] &= \sum_{k=0}^{N-1} \theta_{k+1} \Im\{\mathbf{X}_{(m,k)}\} e^{jk(n-mN)(2\pi/N)} \end{aligned} \tag{4.10}$$

and where θ_k is the *theta sequence* or *theta pattern*, defined as:

$$\theta_k = \begin{cases} \pm 1, & \text{if } k \text{ is even;} \\ \pm j, & \text{if } k \text{ is odd,} \end{cases} \tag{4.11}$$

which can be included within the symbol mapping stage as product by j^k. The expression for the prototype filter of OQAM-FBMC is also Eq. (4.4). For fair performance comparison purposes, it is worth noting that the sampling frequency in OQAM-FBMC must be twice the one used for the rest of schemes presented in this chapter.

4.3 Implementation Aspects

4.3.1 Harmonized transceiver design

As already introduced, an all-encompassing solution integrating these waveforms in a single harmonized implementation would be very beneficial to provide flexible adaptation to particular communication scenarios and while reducing implementation costs. For this particular purpose, the block diagrams of a proposed harmonized transmitter and receiver are presented in Fig 4.2 and 4.3,

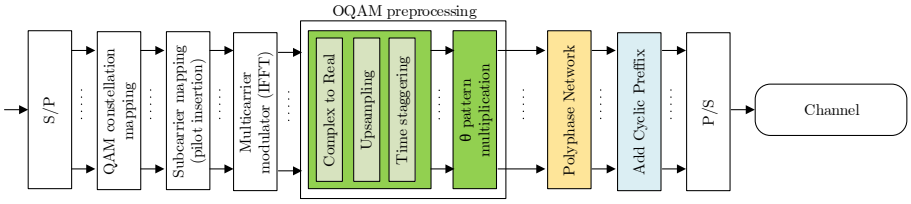

Figure 4.2: Proposed harmonized transmitter for multicarrier waveform generation

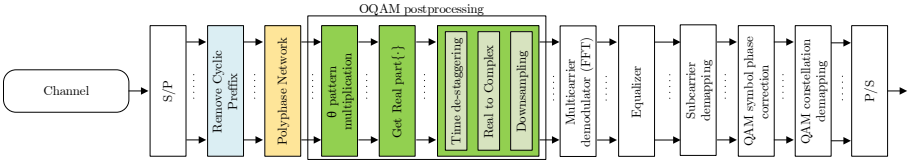

Figure 4.3: Proposed harmonized multicarrier receiver

respectively. The diagrams correspond to a generic multicarrier waveform as the one represented by Eq. (4.10), focusing on a specific implementation based on polyphase filtering, carried out in the time domain through a PPN [100].

All the waveforms include all the general blocks of the diagram (in white). By selectively enabling or disabling particular blocks, both harmonized implementations are able to generate and reconstruct each one of the different multicarrier waveforms. The blocks that require specific configuration for each waveform are emphasized with colors and are next detailed:

On the one hand, all the waveforms include all the general blocks of the diagram (in white). On the other hand, the blocks of the harmonized implementation that require specific configuration for each waveform are emphasized with colors and are next detailed:

- OQAM preprocessing/postprocessing: The green blocks contain the necessary preparative multiplexing steps for the OQAM-FBMC transmission (complex to real number conversion of QAM complex symbols, upsampling, and time staggering), and OQAM-FBMC reception (real to complex number conversion, downsampling, and time de-staggering).

- Polyphase network: The yellow blocks perform the convolution of the discrete signals with a filter implemented through a PPN. The prototype

filter is assumed to be purely real. All waveforms except for OQAM-FBMC require one complex-valued filtering operation while OQAM-FBMC requires two real-valued filtering operations in parallel (see Subsection 4.2.2). As a result, two PPNs are needed. If the filtering stage is disabled (i.e. CP-OFDM) the impulse response may be assumed to be ideal.

- Add/Remove cyclic prefix: The blue blocks carry out the insertion and extraction of cyclic extensions, which for CP-OFDM variants are added after the IFFT operation at the transmitter and removed before the FFT at the receiver. It is possible to disable the blocks by configuring the associated CP length to zero ($N_{\mathrm{CP}} = 0$).

The proposed harmonized block diagram implementation assists in the selection of the building blocks for each particular multicarrier waveform. Regarding the CP-OFDM variants, all of them will leave aside the green blocks and include the blocks in blue for the CP addition and removal. With respect to the inclusion of the filtering blocks (in yellow), it will actually depend on the specific variant. Plain CP-OFDM will not require these blocks, whereas W-OFDM and P-OFDM will need them (although using only one PPN). Concerning the QAM-FBMC waveform, it must contain all the blocks in Figures 4.2 and 4.3 except for those involving the CP, in blue, and the operations in charge of OQAM generation, shown in green. Finally, the transmission of OQAM-FBMC will require all the blocks of the diagram but the ones involving the CP.

4.3.2 Fast Fourier transform implementation

The Discrete Fourier Transform (DFT) is a constituent part of multicarrier waveforms. By inspecting Eq. (4.10), isolating the terms that imply filtering from those that do not, and compacting the products by means of matrix multiplication, then:

$$\begin{aligned}\mathbf{x}[n] &= \sum_{m=-\infty}^{+\infty} \sum_{k=0}^{N-1} \mathbf{X}_{(m,k)} p[n - mN] e^{jk(n-mN)(2\pi/N)} = \\ &= \sum_{m=-\infty}^{+\infty} \mathrm{IDFT}[\mathbf{X}_m] \odot \mathbf{p}_{K-1-m} \\ &= \sum_{m=-\infty}^{+\infty} \mathbf{x}_m \odot \mathbf{p}_{K-1-m},\end{aligned} \tag{4.12}$$

where "$\odot$" denotes Hadamard (element-wise) product, the $\mathbf{X}_m$ is defined as the $N \times 1$ vector whose k-th component is $\mathbf{X}_{(m,k)}$, $\mathbf{x}_m$ is the $N \times 1$ vector resulting from the inverse DFT (IDFT) of $\mathbf{X}_m$, and $\mathbf{p}_m$ is defined as the $N \times 1$ vector whose n-th component is $p[n - mN]$.

The IDFT operation may be computed through the inverse of a FFT. A typical implementation of the inverse FFT (IFFT) is the split-radix algorithm [101], which yields identical computational cost for both the FFT and IFFT. In this work, the complexity is computed by unfolding a complex multiplication into its real-valued counterparts (A complex multiplication is equal to four real-valued multiplications and two real-valued additions); then the total number of real operations is determined. In particular, the number of real-valued multiplications required by a FFT of size N is:

$$C\mathrm{m}_{\mathrm{FFT}}(N) = N \log_2 N - 3N + 4, \tag{4.13}$$

while the number of real-valued additions is:

$$C\mathrm{a}_{\mathrm{FFT}}(N) = 3N \log_2 N - 3N + 4. \tag{4.14}$$

The total number of floating point operations (flops) is the sum:

$$C\mathrm{f}_{\mathrm{FFT}}(N) = C\mathrm{m}_{\mathrm{FFT}}(N) + C\mathrm{a}_{\mathrm{FFT}}(N) = 4N \log_2 N - 6N + 8 \tag{4.15}$$

Because of its importance for reducing the complexity costs of OQAM-FBMC, the simultaneous calculation of the FFTs of size N of the two real-valued inputs involved is proposed, e.g. $g[n]$ and $h[n]$, via a single FFT of size N with complex-valued inputs, as shown in the following [102]:

$$\mathcal{F}(h[n] + j\ g[n])_k = Z[k] = R[k] + j\ I[k], \tag{4.16}$$

where $R[k] = \Re\{Z[k]\}$ and $I[k] = \Im\{Z[k]\}$, via the following set of properties:

$$\begin{aligned} H[k] &= \left(\frac{R[k]}{2} + \frac{R[N-k]}{2}\right) + j\ \left(\frac{I[k]}{2} - \frac{I[N-k]}{2}\right), \\ G[k] &= \left(\frac{I[k]}{2} + \frac{I[N-k]}{2}\right) - j\ \left(\frac{R[k]}{2} - \frac{R[N-k]}{2}\right) \end{aligned} \tag{4.17}$$

After performing the IFFT, the additional total cost of reconstructing each individual FFT for both two real-valued inputs is $C\mathrm{m}_{\mathrm{C2R}}(N) = 8N$, and $C\mathrm{f}_{\mathrm{C2R}}(N) = 12N$. Note that from now on, subscript 'm' refers to the number of real-valued multiplications, 'a' to the number of additions, and 'f' to the number of flops.

4.3.3 Filter bank implementation through a PPN

Multicarrier systems segment signals into (and reconstruct signals from) subbands via a set of N parallel filters called a filter bank. At the transmitter, the Analysis Filter Bank (AFB) is designed to split the signal into subbands according to the waveform properties. At the receiver, the Synthesis Filter Bank (SFB) is designed to rebuild the input signal by merging appropriately the outputs of these filters together.

This work considers that these filter banks are designed as Finite Impulse Response (FIR) filters. It also follows from the concept of prototype filter that the filter banks are uniform, that is, all filters in the filter bank are derived from the prototype filter via uniformly spaced frequency shifts. The uniformity of the filter bank is revealed by inspecting $P(z)$, the Z-transform of the FIR prototype filter $p[i]$ of KN coefficients, defined as:

$$\begin{aligned} P(z) &= \sum_{i=-\infty}^{+\infty} p[i]\ z^{-i} = \sum_{i=0}^{KN-1} p[i]\ z^{-i} \\ &= \sum_{n=0}^{N-1}\sum_{m=0}^{K-1} p[n+mN] z^{-(n+mN)} \\ &= \sum_{n=0}^{N-1} E_n(z^N) z^{-n},\ \text{with}\ \{z \in \mathbb{C}\}, \end{aligned} \tag{4.18}$$

where $E_n(z^N) = \sum_{m=0}^{K-1} p[n+mN] z^{-mN}$ are the polyphase components of $P(z)$. Let us denote by $P_k(z)$ the k-th parallel filter of the filter bank, created by applying a frequency shift of k/N to $P(z)$. It can be shown that:

$$P_k(z) = P(ze^{-j2\pi k/N}) \quad = \sum_{n=0}^{N-1} E_n(z^N) z^{-n} e^{j2\pi n(k/N)} \tag{4.19}$$

and thus the polyphase components of the prototype filter are a constant term independent from k and present for any $P_k(z)$.

In this sense, the most common implementation option for the design of the AFB and SFB is the PPN approach because it provides a significant reduction of the computational complexity through the use of polyphase filtering. A PPN filter bank modulates the prototype filter and carries out the addition, returning multiple bands of decimated and filtered time-domain data symbols from the IFFT stage. The IFFT implicitly multiplies by a complex phasor and is used to perform modulation to the different frequencies according to the

prototype filter. The PPN thus removes the redundancy in the computations through time domain processing. Broadly speaking, this scheme requires an FFT of size N, roughly KN multiplications and storing KN samples for the PPN. As a disadvantage, a receiver implementing a polyphase network must perform subcarrier equalization in the time domain.

The polyphase network filtering structure is made clear by building $\mathbf{y}_s$, that is, the N samples of the s-th symbol via the terms of Eq. (4.10). By definition, the vector $\mathbf{p}_m$ is non-null only for $0 \leq m \leq K-1$, therefore:

$$\mathbf{y}_s = \mathbf{x}_s \odot \mathbf{p}_0 + \mathbf{x}_{s-1} \odot \mathbf{p}_1 + \ldots + \mathbf{x}_{s-(K-1)} \odot \mathbf{p}_{K-1}. \tag{4.20}$$

Note that, although creating the $\mathbf{p}$ vector requires phase rotations to get the linear phase filters at each subcarrier, the $\mathbf{p}$ vector is fixed and thus the computations need to be done just once.

Producing $\mathbf{y}_s$ requires K point-wise complex products between $N \times 1$ vectors, and $K-1$ complex additions between $N \times 1$ pairs of vectors, so the total number of real-valued multiplications of the PPN filtering of size N in Eq. (4.20) is:

$$C\mathrm{m}_{\mathrm{PPN}}(N, K) = 4NK \tag{4.21}$$

and the total number of flops is:

$$C\mathrm{f}_{\mathrm{PPN}}(N, K) = 4NK + 2NK + 2N(K-1) = 2N(4K-1). \tag{4.22}$$

When the prototype filter is symmetric in the frequency domain, as considered in this work, the complexities in Eq. (4.21) and Eq. (4.22) can be reduced to:

$$C\mathrm{m}_{\mathrm{PPN}-\Re}(N, K) = 2NK \tag{4.23}$$

and the total number of flops is:

$$C\mathrm{f}_{\mathrm{PPN}-\Re}(N, K) = 2NK + 2N(K-1). \tag{4.24}$$

4.4 Complexity of Waveforms

In this section, first the complexity of the different waveforms under study is evaluated and compared. Assuming perfect synchronization between all the

elements, at the transmitter only signal building procedures are accounted for, and at the receiver the recovery of the signal, and the equalizer —its application and update (computing the equalizer coefficients)— are taken into account. With this viewpoint in mind, Eq. (4.5) draws the conclusion that the receiver performs the same operations as the transmitter but in reverse order (generally polyphase filtering and then applying the FFT), and thus the computational complexity of the receivers and transmitters differs mainly in the cost of the equalizer operations. Note that for the CP-OFDM variants, the computation of the CP, although produced naturally by Eq. (4.3), actually has no computational cost because CP insertion is equivalent to copying values already computed on memory.

4.4.1 Complexity of CP-OFDM

The CP-OFDM transmitter may be seen as an IFFT operation, and from Eq. (4.13) and (4.15) the costs are:

$$\begin{aligned} C\mathrm{m}_{\mathrm{TX/CP\text{-}OFDM}}(N) &= C\mathrm{m}_{\mathrm{FFT}}(N) = N\log_2 N - 3N + 4, \\ C\mathrm{f}_{\mathrm{TX/CP\text{-}OFDM}}(N) &= C\mathrm{f}_{\mathrm{FFT}}(N) = 4N\log_2 N - 6N + 8. \end{aligned} \tag{4.25}$$

With respect to the receiver, a single-tap Zero Forcing (ZF) is the simplest CP-OFDM equalization design approach. It takes advantage of the CP to provide frequency-flat fading for each subcarrier. Therefore one complex coefficient is associated to each subcarrier (determined via a complex division that obtains the inverse of the frequency response of the channel and costs $6N$ multiplications and $4N$ additions). Then equalization is applied in the frequency domain with just one complex multiplication (one-tap) which costs $4N$ multiplications and $2N$ additions:

$$\begin{aligned} C\mathrm{m}_{\mathrm{RX/CP\text{-}OFDM}}(N) &= N\log_2 N + 7N + 4, \\ C\mathrm{f}_{\mathrm{RX/CP\text{-}OFDM}}(N) &= 4N\log_2 N + 10N + 8. \end{aligned} \tag{4.26}$$

4.4.2 Complexity of W-OFDM

The W-OFDM transmitter may be seen as a CP-OFDM transmitter that introduces a stage after the CP insertion where the multicarrier symbols are filtered by a short pulse shape ($K = 1$). Using Eq. (4.21)–(4.25) the cost is:

$$
\begin{aligned}
C\mathrm{m}_{\text{TX/W-OFDM}}(N) &= C\mathrm{m}_{\text{FFT}}(N) + \frac{C\mathrm{m}_{\text{PPN}}(N,K)}{K}|_{K=1} \\
&= N\log_2 N - N + 4, \\
C\mathrm{f}_{\text{TX/W-OFDM}}(N) &= C\mathrm{f}_{\text{FFT}}(N) + \frac{C\mathrm{f}_{\text{PPN}}(N,K) + 2N}{K}|_{K=1} - 2N \\
&= 4N\log_2 N - 4N + 8.
\end{aligned}
\tag{4.27}
$$

Similarly, assuming a single-tap equalizer the cost of the W-OFDM receiver is:

$$
\begin{aligned}
C\mathrm{m}_{\text{RX/W-OFDM}}(N) &= N\log_2 N + 9N + 4, \\
C\mathrm{f}_{\text{RX/W-OFDM}}(N) &= 4N\log_2 N + 12N + 8.
\end{aligned}
\tag{4.28}
$$

4.4.3 Complexity of P-OFDM

The P-OFDM transmitter may be conceived as a W-OFDM transmitter that allows the pulse shape to extend over the symbol period ($K \geq 1$). Modifying Eq. (4.27) accordingly, the cost is:

$$
\begin{aligned}
C\mathrm{m}_{\text{TX/P-OFDM}}(N,K) &= C\mathrm{m}_{\text{FFT}}(N) + C\mathrm{m}_{\text{PPN}}(N,K) \\
&= N\log_2 N + 2KN - 3N + 4
\end{aligned}
\tag{4.29}
$$

$$
\begin{aligned}
C\mathrm{f}_{\text{TX/P-OFDM}}(N,K) &= C\mathrm{f}_{\text{FFT}}(N) + C\mathrm{f}_{\text{PPN}}(N,K) \\
&= 4N\log_2 N + 4KN - 8N + 8.
\end{aligned}
\tag{4.30}
$$

With an appropriate design of the CP, the P-OFDM receiver may also take advantage of a single-tap equalizer [103]:

$$
\begin{aligned}
C\mathrm{m}_{\text{RX/P-OFDM}}(N,K) &= N\log_2 N + 4KN + 7N + 4, \\
C\mathrm{f}_{\text{RX/P-OFDM}}(N,K) &= 4N\log_2 N + 4KN + 8N + 8.
\end{aligned}
\tag{4.31}
$$

4.4.4 Complexity of QAM-FBMC

Since the QAM-FBMC transmitter is a P-OFDM transmitter without CP insertion, its complexity is given by Eq. (4.29) and Eq. (4.30). Because of the lack of a CP, the QAM-FBMC receiver implements a Least Mean Square (LMS) equalization algorithm with L equalizer coefficients, which minimizes the minimum mean-square error (MMSE), and assumes a typical pilot-based channel estimation used in CP-OFDM systems. This approach leads to significantly improved results, while keeping the complexity of the algorithm still low [104]

(applying it amounts to $4NL_{\text{eq}}$ multiplications and $2NL_{\text{eq}}$ additions and updating the equalizer coefficients amounts also to $4NL_{\text{eq}}$ multiplications and $2NL_{\text{eq}}$ additions):

$$\begin{aligned} C\text{m}_{\text{RX/QAM-FBMC}}(N,K) &= N\log_2 N + 2KN + 8NL_{\text{eq}} - 3N + 4, \\ C\text{f}_{\text{RX/QAM-FBMC}}(N,K) &= 4N\log_2 N + 4KN + 12NL_{\text{eq}} - 8N + 8. \end{aligned} \tag{4.32}$$

4.4.5 Complexity of OQAM-FBMC

As explained in Subsection 4.3.2, the implementation that fits the harmonization purposes of this work best consists of implementing the two real-valued IFFT of size N as one IFFT of size N, then adding the OQAM preprocessing, and finally performing two polyphase filtering procedures in parallel of size N.

The cost of computing one FFT of size N to compute two IFFTs of size N with the purely real and purely imaginary components as inputs, respectively is obtained from Eq. (4.13) and Eq. (4.15)

$$\begin{aligned} C\text{m}_{\text{FFT-OQAM}}(N) &= C\text{m}_{\text{FFT}}(N) + C\text{m}_{\text{C2R}}(N) \\ &= N\log_2 N + 5N + 4, \end{aligned} \tag{4.33}$$

$$\begin{aligned} C\text{f}_{\text{FFT-OQAM}}(N) &= C\text{fm}_{\text{FFT}}(N) + C\text{f}_{\text{C2R}}(N) \\ &= 4N\log_2 N + 6N + 8. \end{aligned} \tag{4.34}$$

The total cost of the OQAM-FBMC transmitter is:

$$\begin{aligned} C\text{m}_{\text{TX/OQAM-FBMC}}(N,K) &= C\text{m}_{\text{FFT-OQAM}}(N) + 2C\text{m}_{\text{PPN}-\Re}(N,K) \\ &= N\log_2 N + 4KN + 5N + 4, \end{aligned} \tag{4.35}$$

$$\begin{aligned} C\text{f}_{\text{TX/OQAM-FBMC}}(N,K) &= C\text{f}_{\text{FFT-OQAM}}(N) + 2C\text{f}_{\text{PPN}-\Re}(N,K) \\ &= 4N\log_2 N + 8KN + 2N + 8. \end{aligned} \tag{4.36}$$

The cost of the OQAM-FBMC receiver, which also implements the LMS equalizer, is:

$$\begin{aligned} C\text{m}_{\text{RX/OQAM-FBMC}}(N,K) &= N\log_2 N + 4KN + 8NL_{\text{eq}} + 5N + 4, \\ C\text{f}_{\text{RX/OQAM-FBMC}}(N,K) &= 4N\log_2 N + 8KN + 12NL_{\text{eq}} + 2N + 8. \end{aligned} \tag{4.37}$$

4.4.6 Complexity comparisons

From now on, overlap factors of $K = 2$ and also the typical $K = 4$ are considered, assuming $L_{\text{eq}} = 3$ equalizer coefficients [105], a number within the typical range of values of 2 to 20 (more than 20 taps do not provide noticeable enhancement [104, 106]). Fig. 4.4 and 4.5 show the cost for the standalone transmitters implementing each waveform for $K = 2$ and $K = 4$, respectively. As is shown, the most complex waveform is OQAM-FBMC and, above $N = 512$ subcarriers, transmitters experience significant complexity differences. For $N = 4096$, CP-OFDM and W-OFDM are twice less complex than OQAM-FBMC and 1.5 times less complex than P-OFDM. Note that for $K = 2$ the inherent cost of implementing a waveform of the FBMC family is lower but performance will be also reduced.

Fig. 4.6 and 4.7 shows the cost for the standalone receivers implementing each waveform for $K = 2$ and $K = 4$, respectively. As expected, the receiver is always more complex than the transmitter because of the equalizer. Also, it is apparent that the cost of the equalizer starts dominating the complexity for $N \geq 128$, as it shows that the waveform receivers that require the LMS equalizer are significantly more complex (QAM-FBMC and OQAM-FBMC) than the waveforms that work satisfactorily using a simpler equalizer (CP-OFDM family). It is worth noting that the weight of the equalizer on the overall complexity increases with the value of L_{eq}.

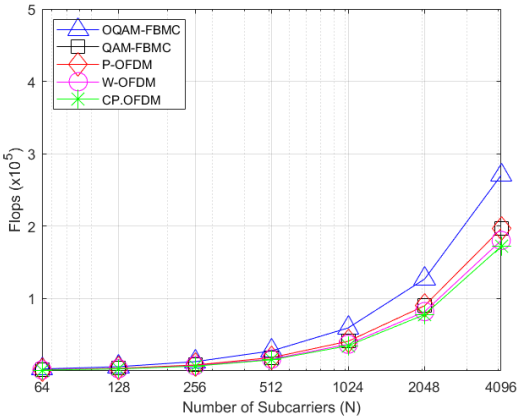

Figure 4.4: Comparison between transmitters complexity for the different waveforms under study for $K = 2$

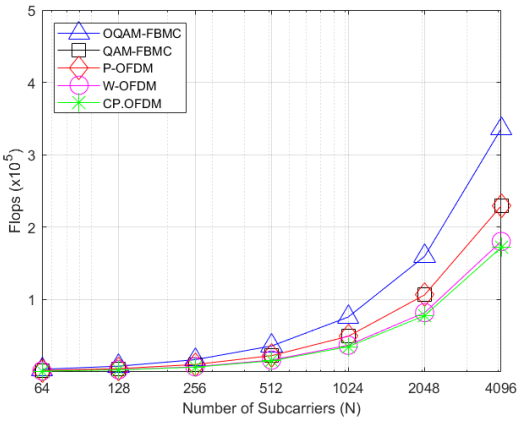

Figure 4.5: Comparison between transmitters complexity for the different waveforms under study for $K = 4$

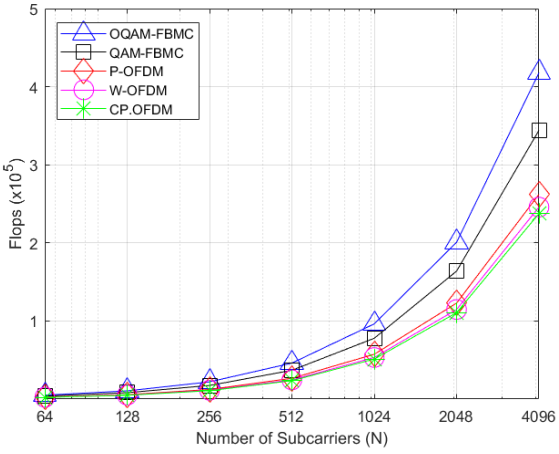

Figure 4.6: Comparison between receivers complexity for the different waveforms under study for $K = 2$

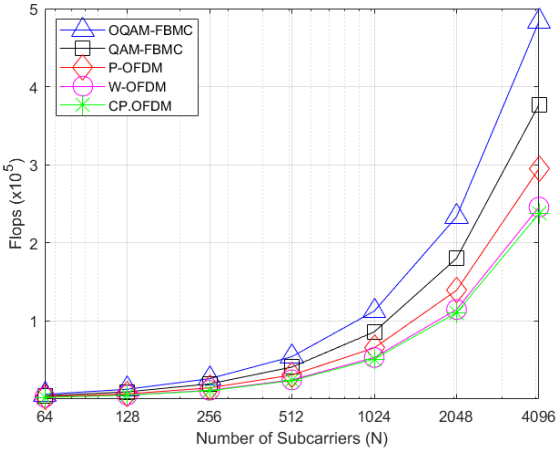

Figure 4.7: Comparison between receivers complexity for the different waveforms under study for $K = 4$

4.5 Complexity of Harmonized and Nonharmonized Implementations

4.5.1 Complexity of the proposed harmonized systems

A harmonized transmitter generating all waveforms requires at least one FFT block of size N (common to all waveforms) with complexity $C\mathrm{f}_{\mathrm{FFT}}(N)$, one block to rebuild the FFT of two real-valued inputs (required for OQAM-FBMC) with complexity $C\mathrm{f}_{\mathrm{C2R}}(N)$, and two blocks of real-valued polyphase network filtering with complexity $C\mathrm{f}_{\mathrm{PPN}-\Re}(N, K)$ each. The aggregated complexity is:

$$\begin{aligned} C\mathrm{m}_{\mathrm{TX/HARM}}(N, K) &= N \log_2 N + 4KN + 5N + 4, \\ C\mathrm{f}_{\mathrm{TX/HARM}}(N, K) &= 4N \log_2 N + 8KN + 2N + 8. \end{aligned} \tag{4.38}$$

The harmonized receiver implementation requires all the blocks mentioned in the transmitter above, and additionally an instance of the LMS equalizer, which being more general offers better performance. The total complexity cost is:

$$\begin{aligned} C\mathrm{m}_{\mathrm{RX/HARM}}(N, K) &= N \log_2 N + 4KN + 8NL_{\mathrm{eq}} + 5N + 4, \\ C\mathrm{f}_{\mathrm{RX/HARM}}(N, K) &= 4N \log_2 N + 8KN + 12NL_{\mathrm{eq}} + 2N + 8. \end{aligned} \tag{4.39}$$

4.5.2 Complexity of the non-harmonized systems

The nonharmonized transceiver used here as a baseline for comparison comprises two independent transceivers able to generate either only CP-OFDM or only FBMC waveform variants. As a result, the complexity of such a nonharmonized solution is found by considering the costs of the most complex waveform variants for each family, that is, P-OFDM and OQAM-FBMC, respectively. Therefore, by adding, on one side, the number of multiplications in Eq. (4.29) and Eq. (4.35) and, on the other side, the number of flops in Eq. (4.30) and Eq. (4.36), the complexity values for the nonharmonized transceiver are as follows:

$$\begin{aligned} C\mathrm{m}_{\mathrm{TX/NOHARM}}(N,K) &= 2N\log_2 N + 6KN + 2N + 8, \\ C\mathrm{f}_{\mathrm{TX/NOHARM}}(N,K) &= 8N\log_2 N + 12KN - 6N + 16. \end{aligned} \tag{4.40}$$

Similarly, the nonharmonized baseline receiver comprises a standalone P-OFDM and OQAM-FBMC receivers plus an instance of both a single-tap and a LMS equalizer, respectively. By adding the corresponding costs, the complexities in multiplications and flops of the nonharmonized receiver are as follows:

$$\begin{aligned} C\mathrm{m}_{\mathrm{RX/NOHARM}}(N,K) &= 2N\log_2 N + 6KN + 8NL_{\mathrm{eq}} + 12N + 8, \\ C\mathrm{f}_{\mathrm{RX/NOHARM}}(N,K) &= 8N\log_2 N + 12KN + 12NL_{\mathrm{eq}} + 10N + 16. \end{aligned} \tag{4.41}$$

4.5.3 Complexity comparisons

The complexity savings given by harmonization show similar trends for $K = 2$ and $K = 4$, and thus only the results for $K = 4$ will be reported. Fig. 4.8 shows the percentage of improvement in the complexity costs achieved by the harmonized implementation of the transmitter for different values of N, calculated as $(1 - C\mathrm{m}_{\mathrm{TX/HARM}}(N,4)/C\mathrm{m}_{\mathrm{TX/NOHARM}}(N,4)) \times 100$. As is shown, the typical savings range 25–30% for the number of multiplications and 25–40% for the number of flops. Likewise, Fig. 4.9 shows that the harmonized implementation on the receiver achieves 25–35% improvement in complexity in terms of both multiplications and flops, only a slight reduction in the improvement with respect to the harmonized transmitter because of the fixed cost of the equalizer.

4.6 Conclusions

This chapter uses particularizations of the Gabor system formulation for multicarrier waveforms to identify common functional blocks among the follow-

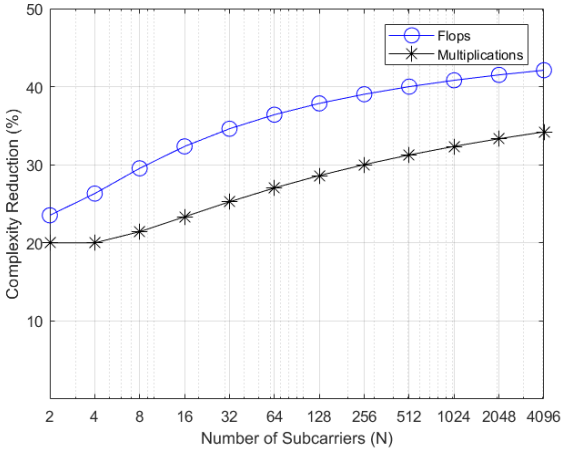

Figure 4.8: Complexity improvement ratio achieved at the transmitter by the harmonized implementation

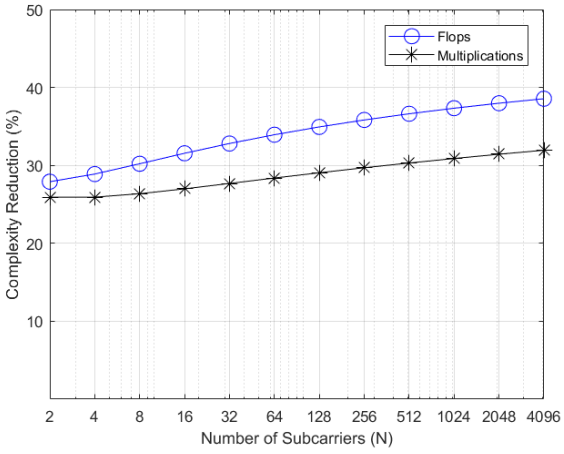

Figure 4.9: Complexity improvement ratio achieved at the receiver by the harmonized implementation

ing former 5G waveform candidates: CP-OFDM, W-OFDM, P-OFDM, QAM-FBMC, and OQAM-FBMC, which are nowadays still into the debate for beyond 5G systems. The impact of the number of subcarriers on waveforms

complexity has been evaluated and compared for the transmitter and receiver. As expected, although CP-OFDM is the simplest waveform, the more complex waveform (OQAM-FBMC) only exhibits significant complexity differences for the transmitters when $N \geq 512$ subcarriers. Because of equalization, the receivers are more complex than the transmitters and, for waveforms that require more sophisticated equalization schemes (FBMC family), the equalizer cost dominates for $N \geq 128$ in average.

This work has further proposed a harmonized implementation that is capable of generating and reconstructing each of the studied waveforms. In contrast to a standalone implementation of the more general waveform candidates of each family (P-OFDM and FMBC-OQAM), this harmonization helps reduce the aggregated complexity cost by sharing as many common functional blocks as possible, while each waveform can be easily generated by means of enabling or disabling the corresponding blocks. In broad terms, the harmonized proposal provides computational cost savings of around 25-40% of flops for the transmitter and 15-25% for the receiver. Therefore, it provides a proper rationale and an incentive for the joint integration of waveforms into a harmonized solution.

Chapter 5

5G OFDM Numerologies

The 3GPP has been working since 2016 on the standardization of the 5G NR [107], the global standard for 5G that will ensure the quality, performance, and interoperability of 5G devices and networks, as the next generation radio technology [108]. 5G NR will make services like automated intelligence, the IoT [109], autonomous vehicles, and virtual/augmented reality, come true. These technologies are based on more prompt, even faster, and more reliable inter-connectivity of everything, resulting in the need for the next generation of mobile communication systems.

5G is designed to provide a wide variety of services, and that is why there are three main challenges that 5G NR must solve in order to enable a truly networked society: a higher traffic volume, a massive growth in the number of devices, and more reliable and low latency transmissions. These challenges result in three broad use cases [110]: eMBB, which requires very high data rates and large bandwidths, e.g., highly mobile UE connected to macrocells; mMTC, which requires low bandwidth, low energy consumption at the UE, and high connection density, e.g., collection of the measurements from a massive number of sensors; and URLLC, which requires very low latency, and very high reliability and availability, e.g., factory process, and power system automation.

Even before the formal beginning of the 5G NR standardization process, there have been different waveforms presented as candidates for this new specification [37, 38, 82], among which are all those mentioned in the previous chapters (CP-OFDM, W-OFDM, UFMC, P-OFDM, FBMC-QAM, FBMC-OQAM). However, in August 2016, after a long process of evaluation and deliberation, 3GPP agreed to adopt only CP-OFDM for both uplink and downlink

in NR Release 15. This gives 5G NR an advantage, since being built upon OFDM (which is used on LTE) allows devices to keep low complexity and, consequently, low hardware costs. Nevertheless, a single OFDM numerology, i.e. subcarrier spacing and cyclic prefix length, cannot fulfil the performance constraints across the desired frequency range and all proposed deployment options and scenarios. This is why the OFDM numerology must be adapted to fit the specific requirements of services, operation frequencies and deployment scenarios.

This chapter provides an in-depth analysis of the use of 5G numerologies within the main 5G channel scenarios, taking into account the operating frequency and the mobility of the UE. Although there are some studies regarding OFDM numerology itself [111, 112]; and some other approaches considering the use of multiple numerologies at the same time, looking for the lowest Inter-numerology Interference (INI) [49–51]; there is currently no evaluation of the impact of numerology changes on the total system interference, making possible to determine whether a numerology is appropriate for a particular 5G scenario. This chapter's main contribution is to provide performance results on the use of the different 5G OFDM numerologies within a specific scenario, taking into account the topology, operating frequency and mobility, allowing to determine which numerology is better fitted for each scenario.

The remaining sections of the chapter are structured as follows:

- Section 5.1 describes the analysis of interference calculation.
- Section 5.2 provides an explanation of the 5G OFDM Numerologies.
- Section 5.3 presents the performance results.
- Section 5.4 draws the main conclusions of this work.

5.1 ICI and ISI Analysis

In an OFDM system, the transmitted data is mapped to some constellation points in order to obtain data symbols. The transmitter then applies an N-point IDFT, with the purpose of obtaining the time domain OFDM symbols. The time domain OFDM n-th block $x[n] = [x_{\text{n,0}}, x_{\text{n,1}}, \ldots, x_{\text{n,N-1}}]$ is given by:

$$x[n] = F_N^H S[n], \tag{5.1}$$

where F_N^H is the N-point IDFT matrix, $S[n] = [s_{\text{n,0}}, s_{\text{n,1}}, \ldots, s_{\text{n,N-1}}]$ is the n-th transmitted symbol, and N is the block size. After the IDFT block, the

CP is added, which is a copy of the last M samples of the IDFT output. The main function of the CP is to avoid the overlapping between consecutive OFDM symbols. In the receiver side, the CP is discarded, and then, an N-point FFT is applied. In the absence of noise, the n-th received block $\hat{X}[n] = [\hat{X}_{\text{n,0}}, \hat{X}_{\text{n,1}}, \ldots, \hat{X}_{\text{n,N-1}}]$ is:

$$\hat{X}[n] = H[n]S[n], \tag{5.2}$$

where $H[n]$ is the time matrix channel, formed by the elements of the channel impulse response during the n-th block interval. This OFDM structure can be affected by several aspects, which in turn trigger harmful effects on its performance. This is the case of a scenario with insufficient CP, which causes ISI and ICI; and the case of a scenario with a high Doppler spread producing ICI.

5.1.1 Insufficient Cyclic Prefix

In the presence of a multipath channel, what happens is that at the receiver side all the multipath components are summed. As a result, we have multiple echoes of each symbol arriving at multiple instances of time and overlapping with each other, causing data to get corrupted and consequently lost. The total delay between the first echo of the symbol and the last one can be measured through the Delay Spread (DS) concept. Therefore, most of the energy caused by the distortion in the symbol reaches up to certain DS given by the characteristic of the channel.

If DS is much longer than the OFDM symbol period T_S, the degradation of the signal is significant (DS $\gg T_S$). Therefore, by extending the symbol length the overlap will happen only on a small portion of the symbol, and hence most of it will not suffer interference ($T_S \gg$ DS). As mentioned before, this is achieved by copying a portion of the last samples to the beginning of the symbol, which is known as the CP.

One of the main benefits of using a CP between consecutive OFDM symbols is that it isolates different OFDM blocks from each other, acting as a guard interval to protect the OFDM signal from ISI. However, there are cases where the CP can be shorter than the DS, which causes ISI because of the overlapping of subsequent symbols. On the other hand, a shorter OFDM symbol period makes subcarriers more separated from each other, which at the end is good to combat ICI. There is a compromise between counteracting the effects of ISI and suffering from more effects of ICI.

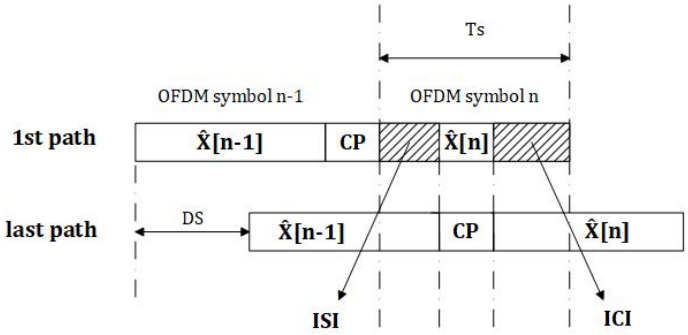

a) Insufficient CP scenario with presence of ISI and ICI

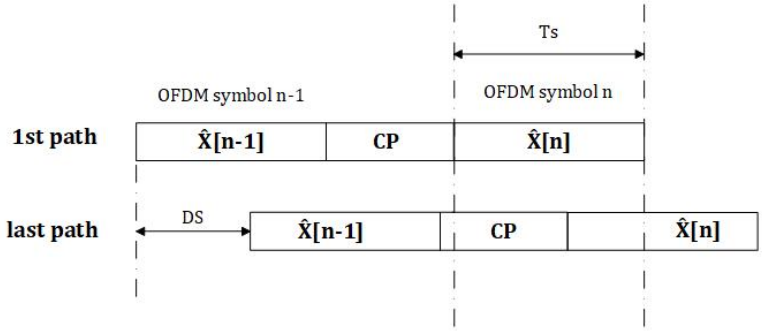

b) Scenario with CP larger than DS and no ISI or ICI

Figure 5.1: Relationship between the DS and CP, and its effect on the ICI and ISI

This can be introduced by extending the model in Eq. (5.2). Considering a channel with an impulse response of length L and a CP of length M, if $L > M$ then the n-th received block now would be [113]:

$$\hat{X}[n] = H[n]x[n] + \hat{X}_1[n] + \hat{X}_2[n], \tag{5.3}$$

where $\hat{X}_1[n] = BX^{(\text{i-1})}$ and $\hat{X}_2[n] = -AX^{(\text{i})}$; B is the $N \times N$ contribution of the elements of the channel impulse response that exceeds the CP, as seen in Eq. (5.5); and A is the same matrix as B but circularly shifted $L - M$ columns to the left, as seen in Eq. (5.4).

$$A = \begin{bmatrix} 0 & \cdots & h_M & h_{M-1} & \cdots & h_{L+1} & 0 & \cdots & 0 \\ 0 & \cdots & 0 & h_M & \cdots & h_{L+2} & 0 & \cdots & 0 \\ \vdots & \cdots & \vdots & \ddots & \ddots & \vdots & \vdots & \vdots & \vdots \\ 0 & \cdots & 0 & 0 & \ddots & h_M & 0 & \cdots & 0 \\ \vdots & \cdots & \vdots & \ddots & \ddots & \vdots & \vdots & \vdots & \vdots \\ 0 & \cdots & 0 & 0 & \cdots & 0 & 0 & \cdots & 0 \end{bmatrix} \tag{5.4}$$

$$B = \begin{bmatrix} 0 & \cdots & 0 & h_M & \cdots & \cdots & h_{L+1} \\ 0 & \cdots & 0 & 0 & h_M & \cdots & h_{L+2} \\ \vdots & \cdots & \vdots & \ddots & \ddots & \ddots & \vdots \\ 0 & \cdots & 0 & \ddots & \ddots & 0 & h_M \\ \vdots & \cdots & \vdots & \ddots & \ddots & \ddots & \vdots \\ 0 & \cdots & 0 & 0 & \cdots & \cdots & 0 \end{bmatrix} \tag{5.5}$$

In Fig 5.1a is possible to see how the previous OFDM symbol $\hat{X}[n-1]$ overlaps a portion of the current symbol $\hat{X}[n]$, this is known as ISI and would correspond to $\hat{X}_1[n]$ in Eq. (5.3). Likewise, it can be seen that the last path contains a part of the current symbol that interferes with itself. This can be considered as a subcarrier shift since it is the same symbol, and therefore is possible to refer to this as ICI, thus corresponding with the term $\hat{X}_2[n]$ in Eq. (5.3). Fig 5.1b shows that when the CP is greater than the DS, there is no ISI or ICI.

5.1.2 Doppler Spread

The mobility of the user equipment with respect to the receiver, that is, the base station, produces a variation in the incoming received signal. This is known as Doppler Spread, and is explained due to the frequency shift that each multipath component experiences as it propagates from the transmitter to the receiver. The rate of this shift (Doppler shift) depends on the speed and direction of the mobile terminal (although in 5G the use of mobile base stations could be expected). The frequency of the received signal will increase as it travels over the air, as long as the distance between the transmitter and receiver decreases; conversely it will decrease when the distance increases.

The above can be explained taking into account the following [114]. Assuming that the user equipment is moving a constant speed v, at the receiver

side each multipath echo will arrive at different instant of time, different phase and different amplitude. The phase change by a single multipath echo is given by:

$$\Delta\phi = \frac{2\pi\upsilon\Delta t}{\lambda}\cos\theta, \tag{5.6}$$

where $\lambda = \frac{c}{f_c}$ is the signal wavelength, f_c is the carrier frequency, c is the speed of light, Δt is the time used by the user equipment to move, and θ is the angle of arrival. Using the terms in Eq. (5.6), the Doppler shift can be derived as:

$$f = \frac{1}{2\pi}\cdot\frac{\Delta\phi}{\Delta t} = \frac{\upsilon f_c}{c}\cos\theta. \tag{5.7}$$

The maximum Doppler shift occurs when the transmitter and the receiver are moving in opposite or same direction ($\theta = 180^{o}$ or 0^{o}):

$$f_{\max} = \frac{\upsilon f_c}{c}. \tag{5.8}$$

As said before, Doppler shift is the effect caused by a single multipath echo, which typically occurs in a free space scenario with Line of Sight (LoS). Doppler spread instead, is a random effect caused by several multipath components coming from different directions. In both cases ICI affects the system, but the one produced by Doppler spread is harder to deal with, since it can degrade considerably the performance of OFDM systems since subcarriers while shifting lose the required orthogonality with their neighbors. An exact equation for the ICI power created by Doppler spread is derived in [115], and is given as:

$$P_{\text{ICI}} = \frac{(f_{\max}T_S)^2}{2}\sum_{\substack{k=1\\k\neq i}}^{N}\frac{1}{(k-1)^2}, \tag{5.9}$$

5.1.3 Unified Interference Model

In [113], a unified interference system model is proposed. In the case of a doubly-selective channel, the channel impulse response is time-variant during an OFDM block, so the first term in Eq. (5.3) can be rewritten as the sum of two components:

$$\hat{X}[n] = \hat{X}_1[n] + \hat{X}_2[n] + \hat{X}_3[n] + \hat{X}_4[n], \tag{5.10}$$

where,

$$\hat{X_3}[n] = H_{\text{ave}}^{[n]}x[n], \tag{5.11}$$

$$\hat{X}_4[n] = H_{\text{var}}^{[n]} x[n], \tag{5.12}$$

and where $H_{\text{ave}}^{(i)}$ is the time average channel impulse response matrix for the i-th received block; and $H_{\text{var}}^{(i)}$ represents the channel variation from the average. The model proposes that $\hat{X}_3[n]$ is the ICI-free and ISI-free term, while $\hat{X}_4[n]$ represents the ICI caused by the channel variations and corresponds to the equation specified in Eq. (5.9), i.e., the ICI power produced by Doppler spread.

5.2 5G NR Numerology

As already mentioned, OFDM has a key role in 5G NR, although a single fixed OFDM numerology is not enough to meet all the requirements presented in the new 5G landscape. So far, LTE supports carrier bandwidths up to 20 MHz with a fixed OFDM numerology regarding CP duration (T_{CP}) and subcarrier spacing (Δf). More specifically, a 15 kHz spacing between OFDM subcarriers is used, with a 4.69 μs CP. The idea for 5G NR is to introduce scalable OFDM numerology in order to support a wide range of frequencies, diverse scenarios and deployment models. One of the most critical requirements is that the OFDM subcarrier spacing must be able to scale with the channel bandwidth, so the processing complexity does not increase exponentially for wider bandwidths, as the FFT size scales.

Therefore, the main difference between LTE numerology (subcarrier spacing and CP length) and 5G NR numerology, is that the latter can support different types of subcarrier spacing. This subcarrier spacing is scalable according to the following factor: 15×2^n kHz, where n is an integer and 15 kHz is the subcarrier spacing used in LTE. By using this 2^n factor, 5G NR ensures that slots and symbols of different numerologies are aligned in the time domain, which is important to efficiently enable TDD networks.

Table 5.1: Numerology Structures for 5G NR

$\Delta f = 15 \times 2^n$ **(kHz)**	**Symbol duration** (μs)	T_{CP} (μs)	**Slot duration** (μs)	**Number of slots/subframe**	**Number of symbols/slot**
15	66.67	4.69	1	1	14
30	33.33	2.34	0.5	2	14
60	16.67	1.17	0.25	4	14
120	8.33	0.57	0.125	8	14

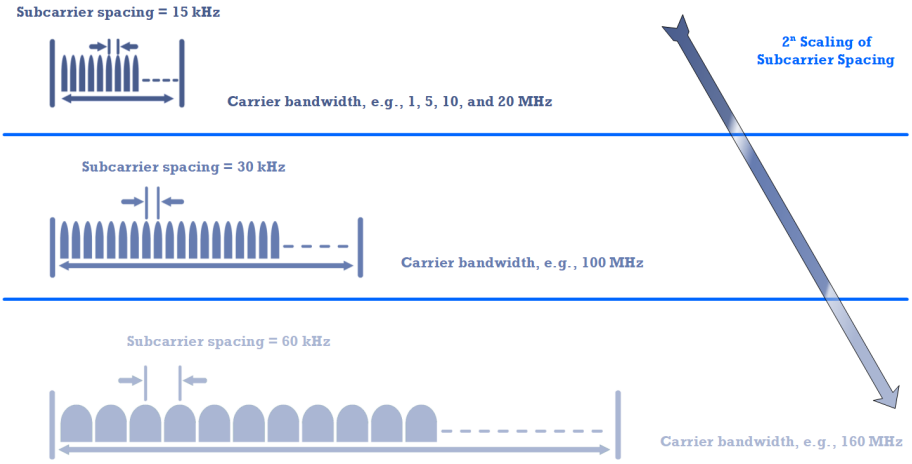

Figure 5.2: Example channel bandwidths, and subcarrier spacing

Other features that change within the frame structure when 5G NR numerology is modified are slot duration, the symbol duration, and the number of slots per subframe, which are inevitably modified by changing the separation of carriers, with a general tendency to get shorter OFDM symbols as subcarrier spacing gets wider. This tendency comes from the nature of OFDM.

Finally, we have the number of OFDM symbols within a slot, which despite not changing intrinsically when changing the numerology, is necessarily adjusted so that the time alignment is not lost. For any numerology, it will always be 14, unlike LTE that had two slots with 7 symbols each. The summary of 5G NR numerology can be seen in Table 5.1.

The choice of a particular numerology depends on various factors including carrier frequency, mobility, type of deployment, service requirements (latency, reliability, and throughput), and implementation complexity. For example, wider subcarrier spacing can be better suited for latency-critical uRLLC services, small coverage areas, and higher carrier frequencies, which could be the case of a V2X scenario. A graphic explanation of the different channel widths and different scalable deployment types can be seen in Fig 5.2.

5.3 Performance Results

The performance comparison of the different 5G NR numerologies at various speeds, frequencies, and within most common 5G channel scenarios, was made with 1000 Transmission Time Interval (TTI) per numerology, using the PHY layer parameters of LTE and adjusting the frame structure with the parameters of the numerologies shown in Table 5.1, a 64-QAM modulation, and a Tapped Delay Line (TDL)-C 300 [116] channel model with 24 taps. The chosen speeds were 3, 120, and 300 km/h, in order to simulate low, medium and high mobility scenarios. Regarding the frequency of operation, the band from 400 MHz to 6 GHz was used (spectrum utilized by LTE), as well as frequencies higher than 6 GHz, which are intended to be used in 5G NR, especially those that correspond to mmWave. Finally, based on a 3GPP calibrated simulator of the LTE PHY layer, changes were made to the CP and subcarrier spacing, in order to obtain the level of interference for every possible scenario.

The TDL-C 300 channel is constructed to represent a particular channel profile for Non Line of Sight (NLoS), allowing to obtain a desired Root Mean Square (RMS) delay spread for a specific scenario by scaling every tap delay according to the following equation:

$$\tau_{\mathrm{n,scaled}} = \tau_{\mathrm{n,model}} \cdot DS_{\mathrm{desired}}, \tag{5.13}$$

Table 5.2: DS scaling factors for all scenarios

Proposed scaling factor		**FREQUENCY [GHz]**						
		2	**6**	**15**	**28**	**39**	**60**	**70**
Indoor Office	Normal-delay profile	39	30	24	20	18	16	16
	Long-delay profile	59	53	47	43	41	38	37
UMi Street-canyon	Normal-delay profile	129	93	76	66	61	55	53
	Long-delay profile	634	316	307	301	297	293	291
UMa	Normal-delay profile	363	363	302	266	249	228	221
	Long-delay profile	1148	1148	955	841	786	720	698
RMa	Normal-delay profile	37	37	N/A	N/A	N/A	N/A	N/A
	Long-delay profile	153	153	N/A	N/A	N/A	N/A	N/A
UMi/UMa O2I	Normal-delay profile	240						
	Long-delay profile	616						

Figure 5.3: Model scenarios topology examples

where $\tau_{\mathrm{n,model}}$ is the normalized delay value of the n-th path, $\tau_{\mathrm{n,scaled}}$ is the new delay value in ns, and DS_{desired} is the wanted delay spread in ns.

On the other hand, the TDL-C 300 model can be scaled to other channel scenarios optimized for 5G NR, that is, for frequencies up to 100 GHz. This is achieved thanks to a scaling factor, which allows adapting the delays for each scenario. The scenarios used are: Indoor office, Urban Micro Street-canyon (UMi street-canyon), Urban Macro (UMa), Rural Macro (RMa), Urban Micro (UMi), and UMa Outdoor-to-Indoor (UMa O2I) [117].

Table 5.2 [116] shows different scaling factors, which have been chosen in such a way that the RMS delay spread covers the entire range observed in

the measurements corresponding to the proposed 5G scenarios. The values of "normal-delay profile" and "long-delay profile" correspond to the median and 90th percentile RMS delay spread for NLOS scenarios.

These "normal-delay profile" and "long-delay profile" DS values are obtained through several measurements and estimations made for the different scenarios used. It can be seen that the highest values of DS are those of the UMa model, and this is due to the fact that in this scenario more objects are present, which causes more echoes to occur and therefore increases the DS. Something similar happens with the UMi/Uma O2I and UMi Street-canyon models, however, the latter has the peculiarity that it confines the signal as if it were a corridor, and due to this topology it presents a lower DS than the other urban models. Finally, we have the Indoor office and RMa models, which are the ones with the lowest DS of all the proposed models; in the case of the first one, it is due to its small coverage area topology, with many objects that reflect the signal, but all of them relatively close to the receiver, while in the case of the latter it is a topology with open spaces, so there are few objects that produce echoes, and therefore the DS is low. All these topologies are visually represented in Fig 5.3 for the sake of clarity and intuitive explanation.

After carrying out the simulations with the different configurations, the results corroborated what was previously explained, i.e., when increasing the speed, the ICI caused by the Doppler spread also increases; while changing numerology and increasing the subcarrier spacing, the CP is reduced and the signal becomes more prone to the ISI and ICI caused by insufficient CP. By adding up the interference of both effects, it is possible to obtain the total percentage of interference of the system for each different scenario. In Fig 5.4 it is possible to observe a comparison between the interference caused by the Doppler spread; the interference caused by insufficient CP; and the total interference of an UMa scenario at 120 km/h. In the graph of the interference caused by Doppler spread it can be seen how for the cases of 15 kHz and 30 kHz subcarrier spacing, the interference increases as the frequency increases, while for 60 kHz and 120 kHz subcarrier spacing there is hardly an increase in the interference. On the other hand, in the graph of interference caused by insufficient CP it can be appreciated that for a 120 kHz subcarrier spacing interference, the DS is so large that the echoes completely overlap the next symbol, therefore this would mean a 100% ISI case. Finally, by considering both interferences, it is possible to determine the best numerology according to the band in use.

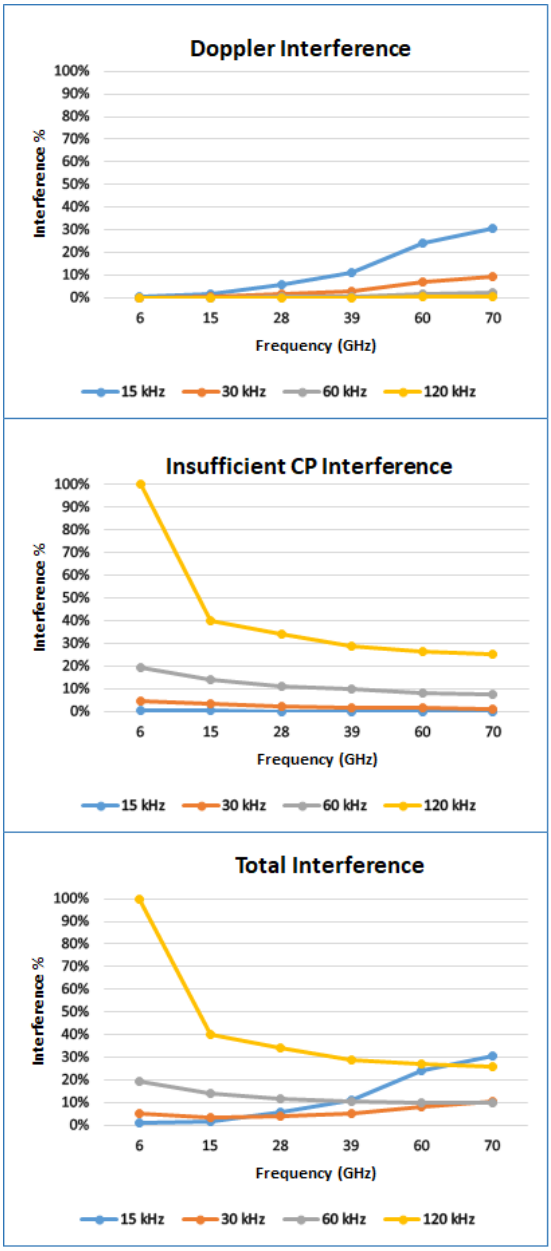

Figure 5.4: Interference comparison for an UMa scenario at 120 km/h

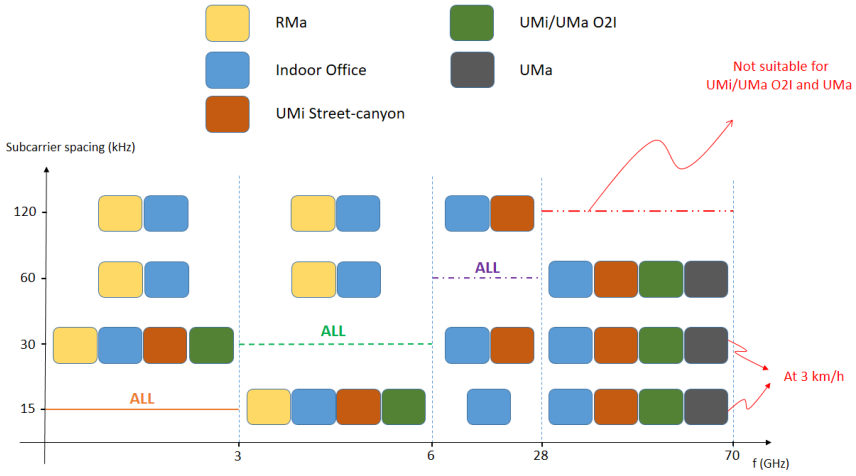

Figure 5.5: Allowed numerologies for each 5G scenario

Fig 5.5 shows which numerology can be used according to the operation frequency, speed and topology. The first thing to note is that for frequencies < 3 GHz, the results show that the 15 kHz subcarrier spacing is the best option, and still a valid option for frequencies between 3 GHz and 6 GHz. This is something to be expected since it is the spectrum used for LTE, which corroborates that 4G systems are currently working optimally. However, for the < 3 GHz band it is possible to use different subcarrier spacing; i.e., 30 kHz subcarrier spacing can be used in UMi Street-canyon, Indoor office, RMa, and UMi/Uma O2I environments; while 60 kHz and 120 kHz subcarrier spacing can be used in Indoor office and RMa environments. Regarding the 3-6 GHz band, where the recommendation is to use a 30 kHz subcarrier spacing, Fig 5.5 shows that as in the < 3 GHz band, it is possible to use a 15 kHz subcarrier spacing in UMi Street-canyon, Indoor office, RMa, and UMi/Uma O2I environments; and also a 60 kHz and 120 kHz subcarrier spacing in Indoor office and RMa environments. An interesting detail is that for this range of frequencies (3-6 GHz), in both Indoor office environment and RMa environment, it is possible to use any numerology since the total interference does not exceed 1%.

For frequencies between 6 and 28 GHz (before mmWave), the recommendation is to use a 60 kHz subcarrier spacing, but as shown in Figure 5.5 it is possible to use a 15 kHz subcarrier spacing in the case of Indoor office environ-

ments; and both 30 kHz and 120 kHz subcarrier spacing for UMi street-canyon and Indoor office environments.

Regarding the mmWave band, it is recommended to use a 120 kHz subcarrier spacing; however, for UMi/UMa O2I and UMa topologies the interference levels using this numerology are not in acceptable ranges, which is why in these scenarios it is better to use a 60 kHz spacing subcarrier. Other topologies that allow the use of a 60 kHz subcarrier spacing in mmWave are Indoor Office and UMi street-canyon. Regarding the 15 kHz and 30 kHz subcarrier spacing numerologies, in mmWave it can be used in any topology (except for RMa, since the channel model used does not allow to scale the DS for frequencies > 6 GHz), as long as it is at low speeds, i.e., pedestrians moving at an average speed of 3 km/h.

5.4 Conclusions

Changes in 5G NR numerology have a significant impact on the total system interference, and its influence can be greater or less depending on the system conditions. This has been verified according to the results obtained, and the analysis of the ICI and ISI under diverse parameters such as frequency, topology and UE speed. However, as explained before, increasing subcarrier spacing involves a trade-off between the ICI effect and the ISI effect over the performance of the system. Therefore, by quantifying this interference, it has been possible to determine the best numerology for each of the analyzed scenarios within the landscape of 5G.

From the results obtained, it can be concluded that the operating frequency should not be the only parameter to take into account when deciding which numerology should be used in a given system. All 5G OFDM numerologies can be used throughout the 5G spectrum, depending on the characteristics of the system. Thus, contrary to what was recommended, 120 kHz is not necessarily the best option for mmWave, since the trade-off between the ICI effect and the ISI effect is not better than the obtained with a 60 kHz subcarrier spacing.

Future work includes analysis adding mobility to the base station, so that the UE is not the only element with a travel speed. This could be useful to determine the best 5G OFDM numerology for systems where base stations are drones that constantly change height and position, in order to maximize coverage, reaching even sectors with difficult access.

Chapter 6

From 5G to 6G

For more than forty years, engineers and researchers have been developing new technologies and standards of the different generations of mobile communications not only to accommodate the always increasing demand of traffic, but also to improve human and machine communications [118]. Nowadays, we are seeing that the brand new SG is rolling out in small scale in the form of a campus-style or even private networks. However, taking into consideration that the main scenarios of 5G were defined as three: eMBB, mMTC, and URLLC [119], in Release 15 the only scenario receiving attention from the 3GPP standards was eMBB.

That is, 5G has just been born, and we will still see in the coming years an important evolution of its characteristics, an evolution that will allow it to reach the three desired services. However, from the point of view of research, it is time to start talking about the sixth generation mobile, that is, the technologies that will change the way we see the world in 2030. This is the advent of the 6G.

Although it seems surprising, it was in September 2018 when the first rigorous article dealing with the topic of 6G was published [120]. Klaus David was the first one to wonder if a new generation mobile was really needed. Soon, other researchers came to the discussion reinforcing the idea that yes, on their view there will be a new paradigm that supposes the sixth generation mobile. In fact, the first ideas regarding the 6G revolution came from the hand of quantum technologies.

In April 2019, Nawaz et al. [121] defended the idea that the 6G should be the union of greater transmission capabilities and Artificial Intelligence (AI) enabled by quantum processors. They would not be the only ones, since from this point on, any contribution on the 6G vision includes a fact: the 6G will bring the incorporation of AI into mobile communications systems [55, 56, 122, 123].

Some more recent articles go one step further, and come to define the Key Performance Indicators (KPIs) that will characterize it [55, 122]. Others focus more on use cases [123], or even to investigate unconventional communications, such as underwater [122]. As with AI, everyone agrees that the 6G will be a Terahertz technology, likely using Visible Light Communications (VLC) too.

This chapter carries out a conceptualization exercise of the 6G from the conviction that the network will be articulated from indoor plus aerial deployment and, therefore, conventional base stations will be removed. The remaining sections of the chapter are structured as follows:

- Section 6.1 presents the main use cases that require the design of a new mobile generation.
- Section 6.2 describes in detail the first technological pillar of this 6G, that is, the cell-less deployment.
- Section 6.3 explains the importance of the extension of the access point up to a few meters distant from the user, which is the second technological pillar.
- Section 6.4 outlines third and last technological pillar of 6G, that is, the configuration of a federated network of shared intelligence.
- Section 6.5 gathers some final questions, as well as suggestions on how to arrange the process that comes in the near future.

6.1 Vision on the Use Cases

The definition of a new mobile generation always begins by imagining, in the first place, the most characteristic applications of the society making use of that technology. In this case, is necessary to project our imagination to 2030 and figure out how our society will look like in 10 years.

Fig 6.1 shows an exercise of this speculative projection, where the main services are distributed in space according to three axes. These axes correspond to a group of services as proposed in this chapter, depending on the

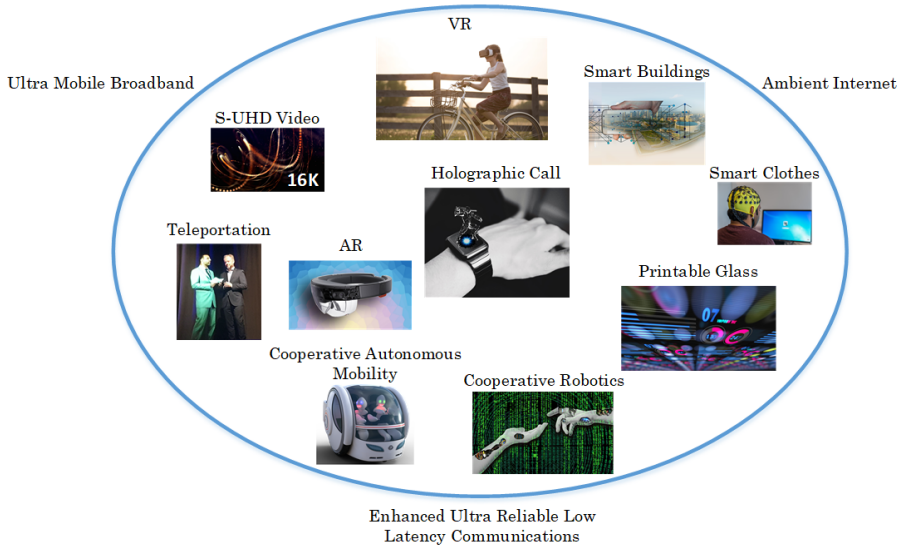

Figure 6.1: Use cases envisioned for 6G organized according to dimensions of UMBB, Ambient Internet and eURLLC

main characteristics that define them. Specifically, three types of services have been contemplated and are described in the following sections.

Special attention is paid to the holographic call service, since this is the killer application of the 6G.

6.1.1 Ultra Mobile Broadband

Ultra Mobile Broadband (UMBB) service type a service characterized by the fact that is the capacity of the link which determines the quality of experience of the end user. Typically, it can be assimilated with the services that are executed in the user's terminal, although it is not clear if this terminal will be a handheld device, a watch, a wearable or some kind of glass or headset.

One aspect in which all researchers agree upon is that this type of service will continue to exist, and it is likely that with capacity requirements not much higher than those offered by 5G, but in any case, providing a transmission experience in the terminal between 10 and 100 Gbps. Some applications under this category could be the following:

Super-Ultra High Definition (S-UHD) Video

Current devices support 2K+ pixels and a refresh frequency of 60 Hz. For dimensions of around 6 inches, this resolution seems sufficient and our retina would not be able to identify a higher resolution, except for the refreshment, that raising it to 100 Hz would show greater fluidity in the videos. The inclusion of higher resolutions on phone screens are justified by the development of virtual reality technology. When the phone is situated so close to the eyes, pixels are an issue. 16K resolution with a refresh rate of 240 Hz is deemed to be the resolution able to make us have a full immersive virtual experience, or project the image in a larger screen, e.g. in the wall of the dinning room. S-UHD refers to a display resolution of 15360 horizontal pixels by 8640 vertical pixels, resulting in a total of 132.7 megapixels per frame. With a refresh rate of 240 Hz, and plain RGB coding, this results in about 750 Gbps data rate. This is UMBB, indeed.

Virtual Reality (VR) on the move

When this S-UHD video gets moving, problems grow. Mainly in two dimensions, the accuracy in the necessary location and the feedback obtained from the environment. The VR gets closer to the Ambient Internet concept discussed in Section ILC since the virtual world has to adapt to the real world and vice versa in order to allow the user to move along without physically crushing with the real objects around that are hidden to his/her eyes. Here the problem lies in the ability to compute and sense in real time that allows adapting the virtual world to the client's desire and to the underlying reality. The interaction with the surrounding objects will be fundamental, and the connection will be of proximity. The architecture requirements from the new 6G network are based on the flexibility and the local interaction of connected devices and sensors.

Teleportation

3D holographic projectors already exist. They are based on two perpendicular LED lines that, hanging from the ceiling or on the floor, allow projecting a 3D image in space. The object to be teleported must be characterized as an Avatar, that is, creating a kind of fictional object, like an object of a game, that characterizes said person or thing. For this, a set of cameras have to record in real time the object to teleport and build the avatar in real time, to later transmit it and be projected. To sum up, what is projected is a 3D reconstruction of a real object or person. In the case of a person, it could even be transported virtually to the new location just by placing a 360 camera at that point and using a VR glass reproducing what is being recorded by the

camera. Humanity has finally managed to teleport, but not by displacing the body, but by bringing the world to us. Along 2019, teleportation experiences have already been done over a SG network, although those experiences to date are very static and of poor quality. By 2030 teleportation will be a daily-use application, a mobile reality that will require transmission capacities at least higher than 1 Gbps everywhere.

Augmented Reality (AR) on the move

In this case the idea is to superimpose to reality some context information that allows interacting with this reality in a rich way.

A kind of glass or helmet shall be used with a light projection over the crystal. From the point of view of data connection, requirements are low — below 100 Mbps in the worse case-—, since the information is minor, although accuracy in location must be in the order of few centimetres and response to the movements of the head must be fast to avoid dizziness, more specifically, below 20 ms [124].

6.1.2 Enhanced Ultra Reliable Low Latency Communications

Enhanced Ultra Reliable and Low Latency Communications (eURLLC) refers to the evolution of concepts already present in the definition of 5G and which are related to the speed in which objects are able to communicate with a guaranteed transmission that in many cases will be necessary for safety reasons. Two main applications are clear examples of this:

Cooperative Autonomous Mobility

The means of transportation as we know them today are about to change. The recent advances in wireless communication networks and the technological development of the automotive industry have paved the way for a safer transportation of passengers and goods. Multiple technologies can be integrated in one autonomous and intelligent vehicle that shall take care of their passengers. In this context, the term Intelligent Transportation Systems (ITS) refers to a new set of information and communications technologies that allow vehicles to exchange information among them and with the infrastructure to improve road safety and travel comfort. Services like auto-activation of the vehicle brakes, and the identification and communication to the driver of road hazard warnings are planned to be feasible in 5 years. At that time, the transportation industry will begin to wonder how to continue evolving, and

for this question, there is a clear answer: efficient transportation. However, several things are missing to get a real efficient transport system, mainly because of the current low V2V communication channel capacity and reliability. Free-Space Optical (FSO) communication and the extension of conventional wireless technologies to multi-hop communications are clear technology trends that will make this service be ultra reliable and ultra low latency. Target values refer to a hundred of microseconds and full reliability of the transmission via multiple paths of communication. Without any doubt, safety is a must when the AI will take control of our vehicles.

Cooperative Robotics

Just like autonomous cars, autonomous robots are a technological reality. The use case of cooperative robotics refers to the future of the industry, what is called Industry 4.0, in which the production processes are flexible and necessarily wireless to exactly match the product-to-product demand. In this scenario, the robots will carry out cooperative production functions, manipulating two robots the same piece and requiring in this case precision levels not known so far to ensure maximum accuracy. The required latency is unknown yet, but should go below the current 1 ms of the 5G.

6.1.3 Ambient Internet

Ambient Internet refers to the last conceptual evolution of the Internet, in which historical information coming from all devices in the network is combined with contextual data from the ambient coming from nearby sensors and, then, AI is applied to produce at the end new user experiences that can be executed into the devices of the network. Home assistants, such as Amazon Alexa or Google Home, are preluding this concept that we are starting to look at today. Some voices call this concept Ambient Internet, others call it Internet of Bodies. This is the 6G.

With respect to some relevant applications related to this kind of service, the following two can be highlighted:

Smart clothing and environment

All the things and objects we have around will be sending information, even our clothes, which will in turn make our context rich-full and therefore useful for the network. Multiple touchpoints will exist, like cars, speakers, chatbots, cameras, etc. Sensors will be everywhere, and they will make AI agents guess what you most likely need at any moment. As an example, publicity could be

adapted to the people that is around, or lighting can be following you, like also doors or air conditioning.

Printable glass and projected objects

Augmented projection interfaces are needed in the form of glasses, clocks, windshields, etc. Heads Up Displays (HUD) used in cars are the technology more mature now. An inherited concept from gaming, with HUDs it is possible to superimpose relevant status information on the windshield of the car, so that the driver can see the road through an image projected on the window of, for example, the odometer. In order to achieve that, what is done is to install a projector on the dashboard of the car, and modify the characteristics of the windshield glass to be more reflective, and therefore the driver can see a reflected image of the projection on the glass. A similar technology could be developed for car windows, house windows, shop windows or, why not, our glass bottle, which reminds us our water consumption.

6.1.4 Holographic call

The holographic call represents everything that 6G will be. Imagine that someone calls you and when answering the hologram of this person appears on your wrist device (see central figure inside Fig 6.1). The question is how to get the recording of your avatar to be projected in mobility, anywhere and without having a specialized recording studio around. The answer lies in the collective intelligence of the network. Any camera seeing you will record images of you and configure another piece of information about your avatar, your virtualized self. Therefore, it may be e.g. the traffic camera that detects your clothing, and the camera of your neighbor in the elevator that detects the shoes you are wearing today. At the end, the details of your face can be captured in live with your front camera, making your avatar created with collective intelligence get alive. UMBB, eURLLC and Ambient Internet, all together in a single application.

6.2 Cell-less Deployment

To date, the cellular concept has been a key element of the mobile and wireless communication networks. It enables an efficient use of the scarce spectrum resources by allowing its reuse in different locations. In this context, cell densification has been a common means to increase the total capacity of a system, and hence we have seen macrocells being complemented by microcells, then picocells and, eventually, femtocells, each one covering shorter ranges. With

the advent of the 6G, even smaller cells, namely attocells and zeptocells, will be deployed, with ranges lower than 10 meters and 5 meters, respectively, to satisfy the higher capacity needs. These kind of cells are already foreseen in the context of VLC communications, where attocells are meant to cover rooms, while zeptocells would cover a part of a room, e.g. a desktop. Additionally, this smaller-than-femto cells are also the currently assumption when talking about cells operating in the THz band of spectrum.

The extreme densification will be a reality, above all, in indoor scenarios, where VLC and THz communications characteristic short range is not a significant problem because of the smaller areas to be covered. These technologies come with a huge potential capacity that will be of great use to satisfy the needs of capacity-hungry applications such as S-UHD video, VR, teleportation, etc., which will be commonly indoors. However, we foresee that the huge increase of capacity will exceed the needs of indoors communication allowing the use of part of this capacity to serve the outdoor surrounding environment. Indoor coverage would not be anymore just a problem but a solution that would allow the network operators to reduce the number of long-range cells. In fact, we foresee a more general trend in which the higher density of short-range stations will lead to less and less long-range stations being active, eventually leading to the end of the macro-stations.

An important problem of the cellular concept is the intercell interference, which has an impact on the quality of service experienced by the users in the border of the service areas of different cells. Cell coordination techniques have been proposed to mitigate this problem, but these proposals have not been implemented in reality. One reason is the high complexity of some proposals, whose real time implementation was not feasible. Another reason is that some proposals were useful basically in ultra-dense deployments, which have not been deployed in the real world. Nevertheless, these conditions will change in 6G. The outcome is that it will be feasible a higher degree of joint work between neighbor cells. Users could in this case be connected to multiple cells that would coordinate its resources as if they were part of a single pool of resources, the RAN pool. Therefore, the user would no longer be connected to a specific cell, but to the RAN itself. In this regard, the higher number of transmission/reception points will not result in more cells, but in a cell-less deployment where the center is not the cell but the user, or the service, whose requirements are satisfied by the RAN as a whole.

Not only the network is expected to be denser in the context of 6G, also the user density will increase. In the Ambient Internet, a huge number of devices

Figure 6.2: Cell-less deployment concept

will require local or remote connectivity. A majority of these devices will have low cost and low energy communication equipment, which will benefit from dense network deployments in which the communication takes place in short ranges. But, another implication of this fact is that there will be a huge number of elements with communication equipment. These devices can be not only termination points, terminals of the communication. Instead, they can take an active role in the network being another node more of the radio network. Of course, this is a game-changing idea that has implications on the business models, data privacy issues, etc., but whose benefits would be undeniable. It is clear, for example, that this idea would increase significantly the density of the radio network with the above mentioned benefits. For this vision to be implemented in practice, we foresee that a feature neglected in previous generations has to be considered: multi-hoping. One clear application of multi-hoping is V2X communications. Although multi-hoping has been considered in vehicular ad-hoc networks for a long time, 5G standards have overlooked this feature. However, in the age of autonomous vehicles, we can no longer underestimate its usefulness to empower the vehicles with the higher level of connectivity that comes with multi-hoping.

The end of the cellular era is reinforced by the increasing importance of two types of connectivity nodes, namely unmanned aerial stations and high throughput satellites. Its privileged position in the air facilitates the provision of wide coverage by using them, what makes long-range terrestrial stations less important. Unmanned aerial stations provide an additional benefit which is the high dynamicity in the system configuration and its fast deployment for emergency situations. These concepts are not novel, but its increasingly maturity and the prospect of better regulation and deployment in the 6G time frame will make them a reality.

Fig 6.2 illustrates the cell-less deployment concept, where macro-stations have been ignored on purpose to highlight the key role of short-range stations, new roles of user devices, indoor-to-outdoor coverage, multi-hopping, high-throughput satellites, and unmanned aerial stations.

6.3 Network Everywhere

With the 6G the Internet will move from being available anywhere and anytime in a device to being available everywhere at any time through most devices. Interactions will be different, and the mobile screen will no longer be the only possible interface for our interaction with the Internet. With 6G, in fact, the Internet will disappear from the users life, embedded in the system in a way that obfuscates it.

The most natural next step towards this vision is to distribute antennas everywhere, in such a way that the distance to the end user is reduced to few meters and hopefully with always line of sight conditions. The shorter the link length the better for propagation, interference confinement and feasibility of using higher frequency bands. Next sections are dedicated to describe how this hyper-dense network could work.

6.3.1 Radio-stripes

The concept of radio stripe arises from an idea of Ericsson published in 2018 [125]. In the concept of radio stripe, the antennas and their processing units are connected serially within the same cable, or cable roll, so that a shared bus offers the necessary information for synchronism, data transfer and power supply. In this continuous antenna cable, each access point includes all the required circuit-mounted chips within the same protection cover, so that a radio stripe actually includes multiple antenna elements, as much as the length of

Figure 6.3: Change in the architecture for the radio-stripe concept

the cable.

The radio stripe concept allows flexible and very cheap deployment of a massive antenna system, regardless of the cell concept. From the point of view of what this entails, we would have to imagine how architecture could incorporate this type of radio stripes into any building element and thus make the antennas really be everywhere. Fig 6.3 shows an example of the ease with which the system could be incorporated in blinds, columns or cornices and ceilings, so that the 6G network could have direct vision from any point to the connected devices.

6.3.2 Focused and seamless wireless charging

Since we have antennas everywhere, the idea is to make the most of it and use use beamforming for contact-less battery charge, this is typically referred to as power beaming [126]. If the network is less than 1 m away, all devices could be charged from the same network provided that the beampointing is good enough because a huge number of antennas is used. With the radio-stripe concept, we could go for hundreds of antennas and, therefore, reach the devices without any problem. In fact, the state of the art states that this way of wirelessly charging could reach even kilometers of distance with the appropriate signal processing [126].

6.3.3 Terahertzs

With the network everywhere, where there is always direct vision and short distance between transmitter and receiver, propagation losses are no longer a problem and it is possible to rise more in frequency, beyond the millimeter wave bands proposed for the 5G. In the literature, Terahertzs communications refers to the use of spectrum from 0.1 to 10 THz. In this band we can actually have electromagnetic and light waves, with better propagation conditions than some bands in the mmW spectrum, due to the lack of zones where electromagnetic radiation is absorbed by water. Moreover, the spectrum chunks in Terahertz band can be of hundreds of Gigahertzs, allowing potentially for the Terabit communication objective. Finally, it is worth highlighting that the wavelength in the Terahertz band is by far much shorter than the millimeter wave band, and therefore antenna integration and packaging is supposed to be easier, which is of special relevance for the radio stripe realization.

6.4 Federated AI-based Network

Machine Learning (ML) is an application of AI, based on providing computers with programs that allow them to learn automatically using training data for prediction and classification. Moreover, the proficiency of ML depends on the the existence of an acceptable amount of data to analyze and process and has the dilemma of the large delay of data processing. This condition creates a limitation in the deployment of ML models. Thus, Deep Learning (DL) joined ML as a new family member [127], bringing vigorous algorithms based on structuring the available data using deep neural network. Those algorithms are used in wireless networks such as network traffic classification prediction and control, interference classification, wireless resource allocation, channel estimation, modulation recognition and more [127]. DL has proofed its capacity to reduce the processing time, by executing the algorithms on advanced graphics processing units and advanced tensor processing units.

The 6G will be able to feed the hunger of DL towards data. With the Ambient Internet, data will be continuously collected from a plethora of devices located everywhere around us. In AI nomenclature, the 6G will be a federated deep learning network, where the intelligence is distributed among a number of points. DL and massive amount of data comes with two big challenges, massive data classification and security.

6.4.1 Quantum computing for the federated DL process

Conventional computers are built from billions of transistors that are turned 'on' or 'off' to represent a value of either '1' or '0'. This allows classical computers to store data in form of bits. In contrast, quantum computers process information using quantum bits or 'qubits' that can be represented by superconducting electronic circuits. Due to laws of quantum mechanics, qubits can exist in more than one state at the same point in time. This makes a qubit assume a value of '1' or '0' or both simultaneously. In turn, this enables a quantum computer to process a far higher number of data possibilities than a classical computer. Thus, if we have n interacting qubits, they can simultaneously represent 2^n unique binary patterns, instead of a single binary pattern at-once in the case of classical computers. In addition, assuming superposition, qubits can become 'entangled', which means that the state of a qubit can depend on the state of anothers. This is useful and powerful, as it means that observing one qubit can reveal the state of its unobserved pair.

Indeed, this is the era of Quantum Computing (QC). IBM, Intel and Google have already got advanced cloud-based quantum hardware as well as quantum processors. Besides, those big companies are targeting production-level quantum computers within ten years.

The combined framework of QC and DL will help develop powerful and efficient DL algorithm to satisfy the requirement of 6G. Taking into consideration that in 6G the data transmitted will be in the order of Tbps, using classical computer will not be enough. Therefore, the use of QC is a must to boost the computing capability of the 6G system.

DL in 6G will be used to manipulate and classify a large amount of data in the form of large-dimensional vectors. On the other hand, QC has the great potential to manipulate such large-dimensional data vectors. As a result, this combination will lead QC to accelerate the intelligent data analysis methods of DL [121].

Another advantage of using QC with DL is to provide strong security, which is based on the use of the quantum no-cloning theorem and uncertainty principle. Therefore, in a quantum communication, the qubit is disturbed whenever a wiretapper try to copy or listen to data. This allows the system to detect strange behaviors [128] and potential attacks.

The previous indications assert that the truly intelligence in communication networks will become a reality in 6G communications with QC-assisted DL in a federated AI-based network.

6.5 Conclusions

It is not clear how society will be in the year 2030, but this chapter is a projection exercise to foresee what will be necessary for the mobile network to support in the next generation. There are still doubts about whether there will really be a radical paradigm shift, but there should not be any doubt on the fact that there will be a sixth generation mobile, because the digital world is about to explore its maximum realization. Given everything described in this chapter, it is worth paying attention once again to the waveforms, and wondering if CP-OFDM will be sufficient for the sixth generation of mobile technologies. Most likely, all the requirements detailed here for 6G will be difficult to satisfy with a single waveform (even with different numerologies), so it will be necessary to put on the table, once again, the option of evaluating new waveforms and even consider presenting a harmonized solution that allows evaluating the environmental conditions (through mechanisms such as ML) and selecting an appropriate waveform according to each scenario. From here, it will be a matter of the ITU-R to trigger the consultation process, a process that will begin to be discussed in 2023 and that will call the international community in 2026. Until then, science will continue inventing until the policy puts the industry to work.

Chapter 7

Conclusions

7.1 Concluding Remarks

This dissertation has investigated the waveform harmonization approach as a solution to the debate about which waveform was best suitable for 5G. With this in mind, the first thing was to examine the main waveforms separately, analyzing their fundamental characteristics, their strengths and weaknesses, and its suitability into the 5G and beyond overall landscape. Moreover, after examining the waveforms, for this study three candidates were chosen,that is, CP-OFDM, OQAM-FBMC, and UFMC; which at that time were the most likely to be chosen for the physical layer of 5G. By implementing the physical layer of the three candidates, it was possible to evaluate the performance of each one, and later make a comparison in terms of the BER. In this sense, after analyzing individual performance, the application of a harmonized solution was evaluated from a complexity point of view, that is, the complexity cost of each waveform was compared with that of a harmonized transceiver so its suitability could be considered for 5G. Nonetheless, since the 3GPP decided to use CP-OFDM with mixed numerology for 5G, for the beyond 5G systems the study continued along this line, considering that using a set of numerologies for the physical layer (each one with different features) it is, after all, a harmonized solution. That is why this dissertation has sought a way to select the appropriate numerology for the different scenarios that are presented in beyond 5G. Finally, diverse definitions of what the sixth generation of mobile communications (6G) could become are presented, and along with this the need to talk again about the waveforms for its physical layer.

When analyzing the 5G candidate waveforms, it can be seen that they all have strengths and weaknesses. An important insight from this analysis is that there is a tradeoff between time localization and frequency localization. While P-OFDM, UFMC, W-OFDM, OQAM-FBMC, and QAM-FBMC have low OOB emissions, since their intrinsic mechanisms contribute to good spectral confinement; CP-OFDM, due to its band filtering, has a high OOB leakage. However, precisely because CP-OFDM (by itself) does not have mechanisms to improve frequency location, this makes it the waveform with the least complexity, and therefore, the one with the best time localization. Together with the theoretical study of waveforms, the hardware testbed carried out in this thesis provided important information into the waveform comparative. To begin with, it was possible to verify that the straightforward implementation of OQAM-FBMC is significantly more complex than that of CP-OFDM or UFMC, and therefore not easily applicable to MIMO. In addition, since the testbed was designed to evaluate sidelink transmissions without synchronization, it was observed that OQAM-FBMC and UFMC perform better than CP-OFDM in a scenario with these conditions. However, there exist mechanisms that improve OFDM robustness, like increasing the length of the CP, which is a change in its numerology. Since there are applications that require time localization (such as scenarios with low latency or TDD), others where frequency localization is more important (such as D2D communications), and others that require robustness against the lack of synchronization, it is clear that none of the waveform candidates is capable of fulfilling by its own with all the 5G and beyond requirements. On the other hand, although there are waveforms with advantages over CP-OFDM, none of them outperforms it in a sufficiently relevant way.

Regarding the harmonization of waveforms, as an alternative to choosing a single waveform for 5G, it has been shown that it is possible to elaborate a block diagram that contains the main and common elements of all the waveforms studied, for both the transmitter and the receiver. Furthermore, when evaluating the complexity of said transceiver and comparing it with each waveform individually, it has been determined in the first place that the waveforms with the highest and lowest complexity are OQAM-FBMC and CP-OFDM respectively. On the other hand, it has been found that this difference in complexity becomes noticeable for $N \geq 512$ which is largely due to the complexity added by the sophisticated equalizer that is required in the receiver. In broad terms, the harmonized proposal provides computational cost savings of around 25-40% of flops for the transmitter and 15-25% for the receiver. From the author's point of view, a harmonized solution is still considered a viable solution for beyond 5G systems.

OFDM with mixed numerology is also a harmonized solution based on a single waveform since varying the length of the CP and the number of subcarriers achieves different benefits, which allows adapting the waveform to be used in different scenarios. In this way, the evaluation carried out on the performance of the different numerologies in the scenarios proposed for 5G (applicable also for beyond 5G) showed that the operating frequency should not be the only factor to take into account when selecting a numerology, since that the topology and the UE speed have an important influence on the performance of each numerology. All 5G OFDM numerologies can be used throughout the 5G spectrum, depending on the characteristics of the system, and this dissertation has determined which numerology is suitable for each of the scenarios proposed.

On the other hand, after outlining the landscape of what 6G could become, its main applications, and the important changes that it would bring with respect to current concepts, it is important to consider again whether CP-OFDM -even if it uses mixed numerology- is sufficient to comply with all these new needs. Since it is not yet known with certainty what requirements will be essential for 6G, it is difficult to say that a change in the physical layer and subsequently of the current waveform, is necessary; however, this is likely the case. One of the reasons the 3GPP decided to continue with CP-OFDM was that none of the other candidate waveforms offered high enough performance to warrant a change. Therefore, it is important to continue evaluating new waveforms, pursue improvements in implementations of current waveforms, and consider again the possibility of a harmonized solution with different waveforms, as this thesis has proposed, which would allow adapting the system according to the scenario.

Finally, waveforms are the central element of the physical layer of a mobile communications standard, therefore, it is vitally important that their design and subsequent implementation are optimal, and consequently, all the requirements could be met. At present, more and more proposals appear about new waveforms and improve mechanisms for existing waveforms, so it is expected that this field will continue to advance and within it, there will be enriching debates that will contribute to the construction of new technologies, which in turn serve to improve the experience of mobile phone users.

7.2 Future Research Lines

During the preparation of this thesis, some lines of research that require a more in-depth study have been found. Some of these research directions are the following:

- The theoretical analysis of the waveforms should continue. Many new proposals are being presented for beyond 5G systems, from improvements to existing multicarrier waveforms to new waveforms with innovative solutions in signal processing. It is important to study them and determine which one could be an attractive option for the physical layer of future standards.

- In this sense, another important aspect that should be evaluated regarding all these new proposals is the workability of their implementation. That is why tests are required to determine their complexity, as well as the feasibility of being applicable to techniques such as MIMO and beamforming, especially in mmWave. Of course, this would also lead to the need to compare its performance against CP-OFDM and the other waveforms that were 5G candidates.

- PAPR is one of the main issues for real implementations of multicarrier waveforms. Delving into techniques that allow reducing the PAPR of the different waveforms is of vital importance, since if this obstacle is not solved, all other advantages may be diminished by this problem.

- Further research is also required on waveform harmonization. First of all, and since most of the proposals for beyond 5G are OFDM based, it would be interesting to see if these waveforms share some of the common blocks identified in this dissertation, or if it is necessary to add more blocks, in such a way that the harmonized transceiver improves and broaden its spectrum of applications. Secondly, it would be important to implement this harmonized solution and evaluate its performance. Finally, another aspect that would promote the harmonized solution as an applicable solution in beyond 5G systems, is to find an effective method to determine which waveform should be used, according to the scenario conditions.

- Regarding 5G OFDM numerology, there are still aspects that can be further evaluated. To begin with and continuing with the study carried out in this thesis, more factors could be added to the analysis, such as the mobility of the BS; this would be applicable to scenarios in which the base stations are drones that modify their height and position to provide better coverage. Likewise, it would be interesting to find a way

to transform the developed model so that it is adaptive, which would allow it to be extrapolated to situations in which scenario conditions change rapidly.

Appendix A

Waveform Implementation Code and Results

A.1 OFDM Code

The detailed explanation of the code used for the implementation of CP-OFDM was presented in Chapter 3. This MATLAB code is shown below.

```
%%%%%%%%%%%%%%%%%%%%%%%%%%%%%%
% wl_example_siso_ofdm_txrx.m
%%%%%%%%%%%%%%%%%%%%%%%%%%%%%
 clear

%Params:
USE_WARPLAB_TXRX = 0;     %Enable WARPLab-in-the-loop (otherwise ...
     sim-only)
WRITE_PNG_FILES = 0;      %Enable writing plots to PNG

%Waveform params
N_OFDM_SYMS = 190;  %Number of OFDM symbols
MOD_ORDER = 16;     %Modulation order (1/4/16 = BSPK/QPSK/16-QAM)
TX_SCALE = 1.0;     %Sale for Tx waveform ([0:1])
INTERP_RATE = 2;        %Interpolation rate (1 or 2)

%OFDM params
SC_IND_PILOTS = [8 22 44 58];   %Pilot subcarrier indices
SC_IND_DATA   = [2:7 9:21 23:27 39:43 45:57 59:64]; %Data ...
     subcarrier indices
N_SC = 64;          %Number of subcarriers
CP_LEN = 16;        %Cyclic prefix length
```

```
21 N_DATA_SYMS = N_OFDM_SYMS * length(SC_IND_DATA); %Number of data ...
       symbols (one per data-bearing subcarrier per OFDM symbol)
22
23 %Rx processing params
24 FFT_OFFSET = 4;       %Number of CP samples to use in FFT (on ...
       average)
25 LTS_CORR_THRESH = 0.8;  %Normalized threshold for LTS correlation
26 DO_APPLY_CFO_CORRECTION = 1;     %Enable CFO estimation/correction
27 USE_PILOT_TONES = 1;     %Enabel phase error correction
28 DECIMATE_RATE = INTERP_RATE;
29
30 if(USE_WARPLAB_TXRX)
31
32     %%%%%%%%%%%%%%%%%%%%%%%%%%%%%%%%
33     % Set up the WARPLab experiment
34     %%%%%%%%%%%%%%%%%%%%%%%%%%%%%%%%
35
36     USE_AGC = true;
37
38     NUMNODES = 2;
39
40     %Create a vector of node objects
41     nodes = wl_initNodes(NUMNODES);
42
43     %Create a UDP broadcast trigger and tell each node to be ...
           ready for it
44     eth_trig = wl_trigger_eth_udp_broadcast;
45     wl_triggerManagerCmd(nodes,'add_ethernet_trigger',[eth_trig]);
46
47     %Get IDs for the interfaces on the boards. Since this example ...
           assumes each
48     %board has the same interface capabilities, we only need to ...
           get the IDs
49     %from one of the boards
50     [RFA,RFB] = wl_getInterfaceIDs(nodes(1));
51
52     %Set up the interface for the experiment
53     wl_interfaceCmd(nodes,'RF_ALL','tx_gains',3,30);
54     wl_interfaceCmd(nodes,'RF_ALL','channel',2.4,4);
55
56     if(USE_AGC)
57         wl_interfaceCmd(nodes,'RF_ALL','rx_gain_mode','automatic');
58         wl_basebandCmd(nodes,'agc_target',-10);
59         wl_basebandCmd(nodes,'agc_trig_delay', 511);
60     else
61         wl_interfaceCmd(nodes,'RF_ALL','rx_gain_mode','manual');
62         RxGainRF = 2; %Rx RF Gain in [1:3]
63         RxGainBB = 12; %Rx Baseband Gain in [0:31]
64         wl_interfaceCmd(nodes,'RF_ALL','rx_gains',RxGainRF,RxGainBB);
65     end
66
```

```
67      TX_NUM_SAMPS = nodes(1).baseband.txIQLen;
68      SAMP_FREQ = wl_basebandCmd(nodes(1),'tx_buff_clk_freq');
69      node_tx = nodes(1);
70      node_rx = nodes(2);
71      RF_TX = RFA;
72      RF_RX = RFA;
73
74      %Set up the baseband for the experiment
75      wl_basebandCmd(nodes,'tx_delay',0);
76      wl_basebandCmd(nodes,'tx_length',TX_NUM_SAMPS);
77      example_mode_string = 'hw';
78  else
79      %Use sane defaults for hardware-dependent params in sim-only ...
            version
80      TX_NUM_SAMPS = 32768;
81      SAMP_FREQ = 40e6;
82      example_mode_string = 'sim';
83  end
84
85  %Define a halfband 2x interp filter response
86  interp_filt2 = zeros(1,43);
87  interp_filt2([1 3 5 7 9 11 13 15 17 19 21]) = [12 -32 72 -140 252 ...
        -422 682 -1086 1778 -3284 10364];
88  interp_filt2([23 25 27 29 31 33 35 37 39 41 43]) = ...
        interp_filt2(fliplr([1 3 5 7 9 11 13 15 17 19 21]));
89  interp_filt2(22) = 16384;
90  interp_filt2 = interp_filt2./max(abs(interp_filt2));
91
92  %% Define the preamble
93  sts_f = zeros(1,64);
94  sts_f(1:27) = [0 0 0 0 -1-1i 0 0 0 -1-1i 0 0 0 1+1i 0 0 0 1+1i 0 ...
        0 0 1+1i 0 0 0 1+1i 0 0];
95  sts_f(39:64) = [0 0 1+1i 0 0 0 -1-1i 0 0 0 1+1i 0 0 0 -1-1i 0 0 0 ...
        -1-1i 0 0 0 1+1i 0 0 0];
96  sts_t = ifft(sqrt(13/6).*sts_f, 64);
97  sts_t = sts_t(1:16);
98
99  %LTS for CFO and channel estimation
100 lts_f = [0 1 -1 -1 1 1 -1 1 -1 1 -1 -1 -1 -1 -1 1 1 -1 -1 1 -1 1 ...
        -1 1 1 1 1 0 0 0 0 0 0 0 0 0 0 0 0 1 1 -1 -1 1 1 -1 1 -1 1 1 1 ...
        1 1 1 -1 -1 1 1 -1 1 -1 1 1 1 1];
101 lts_t = ifft(lts_f, 64);
102
103 %Use 30 copies of the 16-sample STS for extra AGC settling margin
104 preamble = [repmat(sts_t, 1, 30)  lts_t(33:64) lts_t lts_t];
105
106 %Sanity check inputs
107 if(INTERP_RATE*((N_OFDM_SYMS * (N_SC + CP_LEN)) + ...
        length(preamble)) > TX_NUM_SAMPS)
108     fprintf('Too many OFDM symbols for TX_NUM_SAMPS!\n');
109     return;
```

```
110 end
111
112 %% Generate a payload
113 tx_data = randi(MOD_ORDER, 1, N_DATA_SYMS) - 1;
114
115 %Functions for data -> complex symbol mapping (avoids comm ...
        toolbox requirement for qammod)
116 modvec_bpsk =  (1/sqrt(2))  .* [-1 1];
117 modvec_16qam = (1/sqrt(10)) .* [-3 -1 +3 +1];
118
119 mod_fcn_bpsk = @(x) complex(modvec_bpsk(1+x),0);
120 mod_fcn_qpsk = @(x) complex(modvec_bpsk(1+bitshift(x, -1)), ...
        modvec_bpsk(1+mod(x, 2)));
121 mod_fcn_16qam = @(x) complex(modvec_16qam(1+bitshift(x, -2)), ...
        modvec_16qam(1+mod(x,4)));
122
123 %Map the data values on to complex symbols
124 switch MOD_ORDER
125     case 2 %BPSK
126         tx_syms = arrayfun(mod_fcn_bpsk, tx_data);
127     case 4 %QPSK
128         tx_syms = arrayfun(mod_fcn_qpsk, tx_data);
129     case 16 %16-QAM
130         tx_syms = arrayfun(mod_fcn_16qam, tx_data);
131     otherwise
132         fprintf('Invalid MOD_ORDER (%d)!\n', MOD_ORDER);
133         return;
134 end
135
136 %Reshape the symbol vector to a matrix with one column per OFDM ...
        symbol
137 tx_syms_mat = reshape(tx_syms, length(SC_IND_DATA), N_OFDM_SYMS);
138
139 %Define the pilot tones
140 if(USE_PILOT_TONES)
141     pilots = [1 1 -1 1].';
142 else
143     pilots = [0 0 0 0].';
144 end
145
146 %Repeat the pilots across all OFDM symbols
147 pilots_mat = repmat(pilots, 1, N_OFDM_SYMS);
148
149 %% IFFT
150
151 %Construct the IFFT input matrix
152 ifft_in_mat = zeros(N_SC, N_OFDM_SYMS);
153
154 %Insert the data and pilot values; other subcarriers will remain ...
        at 0
155 ifft_in_mat(SC_IND_DATA, :) = tx_syms_mat;
```

```
156 ifft_in_mat(SC_IND_PILOTS, :) = pilots_mat;
157
158 %Perform the IFFT
159 tx_payload_mat = ifft(ifft_in_mat, N_SC, 1);
160
161 %Insert the cyclic prefix
162 if(CP_LEN > 0)
163     tx_cp = tx_payload_mat((end-CP_LEN+1 : end), :);
164     tx_payload_mat = [tx_cp; tx_payload_mat];
165 end
166
167 %Reshape to a vector
168 tx_payload_vec = reshape(tx_payload_mat, 1, numel(tx_payload_mat));
169
170 %Construct the full time-domain OFDM waveform
171 tx_vec = [preamble tx_payload_vec];
172
173 %Pad with zeros for transmission
174 tx_vec_padded = [tx_vec ...
        zeros(1,(TX_NUM_SAMPS/INTERP_RATE)-length(tx_vec))];
175
176 %% Interpolate
177 if(INTERP_RATE == 1)
178     tx_vec_air = tx_vec_padded;
179 elseif(INTERP_RATE == 2)
180     tx_vec_2x = zeros(1, 2*numel(tx_vec_padded));
181     tx_vec_2x(1:2:end) = tx_vec_padded;
182     tx_vec_air = filter(interp_filt2, 1, tx_vec_2x);
183 end
184
185 %Scale the Tx vector
186 tx_vec_air = TX_SCALE .* tx_vec_air ./ max(abs(tx_vec_air));
187
188 %% WARPLab Tx/Rx
189 if(USE_WARPLAB_TXRX)
190     %Write the Tx waveform to the Tx node
191     wl_basebandCmd(node_tx,[RF_TX], 'write_IQ', tx_vec_air(:));
192
193     %Enable the Tx and Rx radios
194     wl_interfaceCmd(node_tx,RF_TX,'tx_en');
195     wl_interfaceCmd(node_rx,RF_RX,'rx_en');
196
197     %Enable the Tx and Rx buffers
198     wl_basebandCmd(node_tx,RF_TX,'tx_buff_en');
199     wl_basebandCmd(node_rx,RF_RX,'rx_buff_en');
200
201     %Trigger the Tx/Rx cycle at both nodes
202     eth_trig.send();
203
204     %Retrieve the received waveform from the Rx node
```

```
205     rx_vec_air = wl_basebandCmd(node_rx,[RF_RX],'read_IQ', 0, ...
            TX_NUM_SAMPS);
206     rx_vec_air = rx_vec_air(:).';
207
208     %Disable the Tx/Rx radios and buffers
209     wl_basebandCmd(nodes,'RF_ALL','tx_rx_buff_dis');
210     wl_interfaceCmd(nodes,'RF_ALL','tx_rx_dis');
211 else
212     %Sim-only mode: Apply wireless degradations here for sim ...
            (noise, fading, etc)
213
214     %Perfect Rx=Tx
215     %rx_vec_air = tx_vec_air;
216
217     %AWGN:
218     rx_vec_air = tx_vec_air + ...
            1e-2*complex(randn(1,length(tx_vec_air)), ...
            randn(1,length(tx_vec_air)));
219
220     %CFO:
221     %rx_vec_air = tx_vec_air .* ...
            exp(-1i*2*pi*1e-4*[0:length(tx_vec_air)-1]);
222 end
223
224 %% Decimate
225 if(DECIMATE_RATE == 1)
226     raw_rx_dec = rx_vec_air;
227 elseif(DECIMATE_RATE == 2)
228     raw_rx_dec = filter(interp_filt2, 1, rx_vec_air);
229     raw_rx_dec = raw_rx_dec(1:2:end);
230 end
231
232 %% Correlate for LTS
233
234 %Complex cross correlation of Rx waveform with time-domain LTS
235 lts_corr = abs(conv(conj(fliplr(lts_t)), sign(raw_rx_dec)));
236
237 %Skip early and late samples
238 lts_corr = lts_corr(32:end-32);
239
240 %Find all correlation peaks
241 lts_peaks = find(lts_corr > LTS_CORR_THRESH*max(lts_corr));
242
243 %Select best candidate correlation peak as LTS-payload boundary
244 [LTS1, LTS2] = meshgrid(lts_peaks,lts_peaks);
245 [lts_second_peak_index,y] = find(LTS2-LTS1 == length(lts_t));
246
247 %Punt if no valid correlation peak was found
248 if(isempty(lts_second_peak_index))
249     fprintf('No LTS Correlation Peaks Found!\n');
250     return;
```

```
251 end
252
253 %Set the sample indices of the payload symbols and preamble
254 payload_ind = lts_peaks(max(lts_second_peak_index))+32;
255 lts_ind = payload_ind-160;
256
257 if(DO_APPLY_CFO_CORRECTION)
258     %Extract LTS (not yet CFO corrected)
259     rx_lts = raw_rx_dec(lts_ind : lts_ind+159);
260     rx_lts1 = rx_lts(-64-FFT_OFFSET + [97:160]);
261     rx_lts2 = rx_lts(-FFT_OFFSET + [97:160]);
262
263     %Calculate coarse CFO est
264     rx_cfo_est_lts = mean(unwrap(angle(rx_lts1 .* conj(rx_lts2))));
265     rx_cfo_est_lts = rx_cfo_est_lts/(2*pi*64);
266 else
267     rx_cfo_est_lts = 0;
268 end
269
270 %Apply CFO correction to raw Rx waveform
271 rx_cfo_corr_t = ...
        exp(1i*2*pi*rx_cfo_est_lts*[0:length(raw_rx_dec)-1]);
272 rx_dec_cfo_corr = raw_rx_dec .* rx_cfo_corr_t;
273
274 %Re-extract LTS for channel estimate
275 rx_lts = rx_dec_cfo_corr(lts_ind : lts_ind+159);
276 rx_lts1 = rx_lts(-64-FFT_OFFSET + [97:160]);
277 rx_lts2 = rx_lts(-FFT_OFFSET + [97:160]);
278
279 rx_lts1_f = fft(rx_lts1);
280 rx_lts2_f = fft(rx_lts2);
281
282 %Calculate channel estimate
283 rx_H_est = lts_f .* (rx_lts1_f + rx_lts2_f)/2;
284
285 %% Rx payload processsing
286
287 %Extract the payload samples (integral number of OFDM symbols ...
        following preamble)
288 payload_vec = rx_dec_cfo_corr(payload_ind : ...
        payload_ind+N_OFDM_SYMS*(N_SC+CP_LEN)-1);
289 payload_mat = reshape(payload_vec, (N_SC+CP_LEN), N_OFDM_SYMS);
290
291 %Remove the cyclic prefix, keeping FFT_OFFSET samples of CP (on ...
        average)
292 payload_mat_noCP = payload_mat(CP_LEN-FFT_OFFSET+[1:N_SC], :);
293
294 %Take the FFT
295 syms_f_mat = fft(payload_mat_noCP, N_SC, 1);
296
297 %Equalize (zero-forcing, just divide by compled chan estimates)
```

```
298 syms_eq_mat = syms_f_mat ./ repmat(rx_H_est.', 1, N_OFDM_SYMS);
299
300 %Extract the pilots and calculate per-symbol phase error
301 pilots_f_mat = syms_eq_mat(SC_IND_PILOTS, :);
302 pilot_phase_err = angle(mean(pilots_f_mat.*pilots_mat));
303 pilot_phase_corr = repmat(exp(-1i*pilot_phase_err), N_SC, 1);
304
305 %Apply the pilot phase correction per symbol
306 syms_eq_pc_mat = syms_eq_mat .* pilot_phase_corr;
307 payload_syms_mat = syms_eq_pc_mat(SC_IND_DATA, :);
308
309 %% Demod
310 rx_syms = reshape(payload_syms_mat, 1, N_DATA_SYMS);
311
312 demod_fcn_bpsk = @(x) double(real(x)>0);
313 demod_fcn_qpsk = @(x) double(2*(real(x)>0) + 1*(imag(x)>0));
314 demod_fcn_16qam = @(x) (8*(real(x)>0)) + ...
        (4*(abs(real(x))<0.6325)) + (2*(imag(x)>0)) + ...
        (1*(abs(imag(x))<0.6325));
315
316 switch(MOD_ORDER)
317     case 2 %BPSK
318         rx_data = arrayfun(demod_fcn_bpsk, rx_syms);
319     case 4 %QPSK
320         rx_data = arrayfun(demod_fcn_qpsk, rx_syms);
321     case 16 %16-QAM
322         rx_data = arrayfun(demod_fcn_16qam, rx_syms);
323 end
324
325 %% Calculate Rx stats
326
327 sym_errs = sum(tx_data ~= rx_data);
328 bit_errs = length(find(dec2bin(bitxor(tx_data, rx_data),8) == ...
        '1'));
329 rx_evm = sqrt(sum((real(rx_syms) - real(tx_syms)).^2 + ...
        (imag(rx_syms) - imag(tx_syms)).^2)/(length(SC_IND_DATA) * ...
        N_OFDM_SYMS));
```

A.2 UFMC Code

This section presents the MATLAB code for UFMC, and at the same time presents different results obtained by varying the intrinsic parameters of the waveform.

```
1 %%%%%%%%%%%%%%%%%%%%%%%%%%%%%%%%%%%%
2 % wl_example_siso_ufmc_txrx_par.m
3 %%%%%%%%%%%%%%%%%%%%%%%%%%%%%%%%%%%%
```

```
4  clear
5
6  %Params:
7  USE_WARPLAB_TXRX = 0;    %Enable WARPLab-in-the-loop (otherwise ...
       sim-only)
8  WRITE_PNG_FILES = 0;     %Enable writing plots to PNG
9
10 %Waveform params
11 N_UFMC_SYMS = 190;       %Number of UFMC symbols
12 N_PRB = 4;               %Number of PRB's
13 CP_LEN = 16;             %Cyclic prefix length
14 FILTER_LENGTH = 17;      %Dolph-Chebychev filter length
15 SIDELOB_ATT = 100;       %Dolph-Chebychev sidelob attenuation
16 MOD_ORDER = 4;           %Modulation order (1/4/16 = ...
       BSPK/QPSK/16-QAM)
17 TX_SCALE = 1.0;          %Scale for Tx waveform ([0:1])
18 INTERP_RATE = 2;         %Interpolation rate (1 or 2)
19
20 %UFMC params
21 SC_IND_PILOTS = [8 22 44 58];   %Pilot subcarrier indices
22 SC_IND_DATA   = [2:7 9:21 23:27 39:43 45:57 59:64]; %Data ...
       subcarrier indices
23 SC_NULL = [1 28:38];     %Null subcarrier indices
24 N_SC = 64;               %Number of subcarriers
25 N_SB = N_SC/N_PRB;       %Number of subcarriers per block
26 N_NULLSC = 12;           %Number of null subcarriers
27 N_DATA_SYMS = N_UFMC_SYMS * length(SC_IND_DATA); %Number of data ...
       symbols (one per data-bearing subcarrier per UFMC symbol)
28
29 %Rx processing params
30 FFT_OFFSET = 0;          %Number of CP samples to use in FFT (on ...
       average)
31 LTS_CORR_THRESH = 0.8;  %Normalized threshold for LTS correlation
32 DO_APPLY_CFO_CORRECTION = 1;     %Enable CFO estimation/correction
33 USE_PILOT_TONES = 1;     %Enabel phase error correction
34 DECIMATE_RATE = INTERP_RATE;
35
36 if(USE_WARPLAB_TXRX)
37
38     %%%%%%%%%%%%%%%%%%%%%%%%%%%%%%%%%
39     % Set up the WARPLab experiment
40     %%%%%%%%%%%%%%%%%%%%%%%%%%%%%%%%%
41
42     USE_AGC = false;
43
44     NUMNODES = 2;
45
46     %Create a vector of node objects
47     nodes = wl_initNodes(NUMNODES);
48
```

```
49      %Create a UDP broadcast trigger and tell each node to be ...
            ready for it
50      eth_trig = wl_trigger_eth_udp_broadcast;
51      wl_triggerManagerCmd(nodes,'add_ethernet_trigger',[eth_trig]);
52
53      %Get IDs for the interfaces on the boards. Since this example ...
            assumes each
54      %board has the same interface capabilities, we only need to ...
            get the IDs
55      %from one of the boards
56      [RFA,RFB] = wl_getInterfaceIDs(nodes(1));
57
58      %Set up the interface for the experiment
59      wl_interfaceCmd(nodes,'RF_ALL','tx_gains',3,63);
60      wl_interfaceCmd(nodes,'RF_ALL','channel',2.4,14);
61
62      if(USE_AGC)
63          wl_interfaceCmd(nodes,'RF_ALL','rx_gain_mode','automatic');
64          wl_basebandCmd(nodes,'agc_target',-10);
65          wl_basebandCmd(nodes,'agc_trig_delay', 511);
66      else
67          wl_interfaceCmd(nodes,'RF_ALL','rx_gain_mode','manual');
68          RxGainRF = 2; %Rx RF Gain in [1:3]
69          RxGainBB = 15; %Rx Baseband Gain in [0:31]
70          wl_interfaceCmd(nodes,'RF_ALL','rx_gains',RxGainRF,RxGainBB)
71      end
72
73      TX_NUM_SAMPS = nodes(1).baseband.txIQLen;
74      SAMP_FREQ = wl_basebandCmd(nodes(1),'tx_buff_clk_freq');
75      node_tx = nodes(1);
76      node_rx = nodes(2);
77      RF_TX = RFA;
78      RF_RX = RFA;
79
80      %Set up the baseband for the experiment
81      wl_basebandCmd(nodes,'tx_delay',0);
82      wl_basebandCmd(nodes,'tx_length',TX_NUM_SAMPS);
83      example_mode_string = 'hw';
84  else
85      %Use sane defaults for hardware-dependent params in sim-only ...
            version
86      TX_NUM_SAMPS = 32768;
87      SAMP_FREQ = 40e6;
88      example_mode_string = 'sim';
89  end
90
91  %Define a halfband 2x interp filter response
92  interp_filt2 = zeros(1,43);
93  interp_filt2([1 3 5 7 9 11 13 15 17 19 21]) = [12 -32 72 -140 252 ...
        -422 682 -1086 1778 -3284 10364];
```

```
94  interp_filt2([23 25 27 29 31 33 35 37 39 41 43]) = ...
        interp_filt2(fliplr([1 3 5 7 9 11 13 15 17 19 21]));
95  interp_filt2(22) = 16384;
96  interp_filt2 = interp_filt2./max(abs(interp_filt2));
97
98  %% Define the preamble
99  sts_f = zeros(1,64);
100 sts_f(1:27) = [0 0 0 0 -1-1i 0 0 0 -1-1i 0 0 0 1+1i 0 0 0 1+1i 0 ...
        0 0 1+1i 0 0 0 1+1i 0 0];
101 sts_f(39:64) = [0 0 1+1i 0 0 0 -1-1i 0 0 0 1+1i 0 0 0 -1-1i 0 0 0 ...
        -1-1i 0 0 0 1+1i 0 0 0];
102 sts_t = ifft(sqrt(13/6).*sts_f, 64);
103 sts_t = sts_t(1:16);
104
105 %LTS for CFO and channel estimation
106 lts_f = [-1 1 -1 -1 1 1 -1 1 -1 1 -1 -1 -1 -1 -1 1 1 -1 -1 1 -1 1 ...
        -1 1 1 1 1 -1 1 -1 1 -1 1 -1 1 -1 1 -1 1 1 -1 -1 1 1 -1 1 -1 ...
        1 1 1 1 1 1 -1 -1 1 1 -1 1 -1 1 1 1 1];
107 lts_t = ifft(lts_f, 64);
108
109 %Use 30 copies of the 16-sample STS for extra AGC settling margin
110 preamble = [repmat(sts_t, 1, 30)  lts_t(33:64) lts_t lts_t];
111
112 %Sanity check inputs
113 if(INTERP_RATE*((N_UFMC_SYMS * N_SC) + length(preamble)) > ...
        TX_NUM_SAMPS)
114     fprintf('Too many UFMC symbols for TX_NUM_SAMPS!\n');
115     return;
116 end
117
118 %% Generate a payload
119 tx_data = randi(MOD_ORDER, 1, N_DATA_SYMS) - 1;
120
121 %Functions for data -> complex symbol mapping (avoids comm ...
        toolbox requirement for qammod)
122 modvec_bpsk =  (1/sqrt(2))  .* [-1 1];
123 modvec_16qam = (1/sqrt(10)) .* [-3 -1 +3 +1];
124
125 mod_fcn_bpsk = @(x) complex(modvec_bpsk(1+x),0);
126 mod_fcn_qpsk = @(x) complex(modvec_bpsk(1+bitshift(x, -1)), ...
        modvec_bpsk(1+mod(x, 2)));
127 mod_fcn_16qam = @(x) complex(modvec_16qam(1+bitshift(x, -2)), ...
        modvec_16qam(1+mod(x,4)));
128
129 %Map the data values on to complex symbols and create the row ...
        vector with the constellation symbols
130 %for the 'comb' function
131 switch MOD_ORDER
132     case 2 %BPSK
133         tx_syms = arrayfun(mod_fcn_bpsk, tx_data);
134     case 4 %QPSK
```

```
135             tx_syms = arrayfun(mod_fcn_qpsk, tx_data);
136         case 16 %16-QAM
137             tx_syms = arrayfun(mod_fcn_16qam, tx_data);
138         otherwise
139             fprintf('Invalid MOD_ORDER (%d)!\n', MOD_ORDER);
140             return;
141     end
142
143     %Reshape the symbol vector to a matrix with one column per UFMC ...
            symbol
144     tx_syms_mat = reshape(tx_syms, length(SC_IND_DATA), N_UFMC_SYMS);
145
146     %Define the pilot tones
147     if(USE_PILOT_TONES)
148         pilots = [1 1 -1 1].';
149     else
150         pilots = [0 0 0 0].';
151     end
152
153     %Repeat the pilots across all UFMC symbols
154     pilots_mat = repmat(pilots, 1, N_UFMC_SYMS);
155
156     %% Modulator Block (IDFT + Sub-block Filtering)
157
158     %Construct the IFFT input matrix
159     ifft_in_mat = zeros(N_SC, N_UFMC_SYMS);
160
161     %Insert the data and pilot values; other subcarriers will remain ...
            at 0
162     ifft_in_mat(SC_IND_DATA, :) = tx_syms_mat;
163     ifft_in_mat(SC_IND_PILOTS, :) = pilots_mat;
164
165     %Construct IDFT matrix
166     fftmtx = dftmtx(N_SC);
167     idftmtx = conj(dftmtx(N_SC))/N_SC;
168
169     %Construct sub-blocks and Filter Matrixs
170     tx_payload_vec_final = 0;
171     for iPRB = 1:N_PRB
172         %Sub-blocks
173         ifft_sub_obj{iPRB} = ...
                ifft_in_mat((1+(iPRB-1)*N_SC/N_PRB):(iPRB*N_SC/N_PRB),:);
174
175         %IDFT Spreader
176         filter_sub_mat{iPRB} = ...
                idftmtx(:,(1+(iPRB-1)*N_SC/N_PRB):(iPRB*N_SC/N_PRB),:) * ...
                ifft_sub_obj{iPRB};
177
178         %Filter Matrix
```

```
179         cheby_filter = chebwin(FILTER_LENGTH, ...
                SIDELOB_ATT)./norm(chebwin(FILTER_LENGTH,SIDELOB_ATT)); ...
                %Dolph-Chebyshev filter
180         cheby_filter_bp = ...
                cheby_filter.*(exp(1j*pi*(0:(FILTER_LENGTH-1))*(N_SB+1)...
181         /N_SC).'); %bandpass
182         carrierind(iPRB) = (iPRB-1)*N_SB; % center carrier block
183         centerFshift = zeros(FILTER_LENGTH,1);
184             for k = 1:FILTER_LENGTH
185                 centerFshift(k) = ...
                        exp(2*pi*1i*(k-1)*carrierind(iPRB)/N_SC);
186             end
187         %Frequency-shifted FIR window
188         cheby_filter = cheby_filter_bp.*centerFshift;
189
190         %Generate Toeplitz matrix for convolution
191         filtermtx{iPRB} = ...
                toeplitz([cheby_filter;zeros(N_SC-1,1)],[cheby_filter(1),...
192         zeros(1,N_SC-1)]);
193
194         %Generate sub-block payload
195         tx_payload{iPRB} = filtermtx{iPRB} * filter_sub_mat{iPRB};
196
197         %P/S converter
198         tx_payload_vec{iPRB} = reshape(tx_payload{iPRB}, 1, ...
                numel(tx_payload{iPRB}));
199
200         %Signal mixing
201         tx_payload_vec_final = tx_payload_vec_final + ...
                tx_payload_vec{iPRB};
202     end
203
204     %Construct the full time-domain UFMC waveform
205     tx_vec = [preamble tx_payload_vec_final];
206
207     %Pad with zeros for transmission
208     tx_vec_padded = [tx_vec ...
            zeros(1,(TX_NUM_SAMPS/INTERP_RATE)-length(tx_vec))];
209
210     %% Interpolate
211     if(INTERP_RATE == 1)
212         tx_vec_air = tx_vec_padded;
213     elseif(INTERP_RATE == 2)
214         tx_vec_2x = zeros(1, 2*numel(tx_vec_padded));
215         tx_vec_2x(1:2:end) = tx_vec_padded;
216         tx_vec_air = filter(interp_filt2, 1, tx_vec_2x);
217     end
218
219     %Scale the Tx vector
220     tx_vec_air = TX_SCALE .* tx_vec_air ./ max(abs(tx_vec_air));
221
```

```
222 %% WARPLab Tx/Rx
223 if(USE_WARPLAB_TXRX)
224     %Write the Tx waveform to the Tx node
225     wl_basebandCmd(node_tx,[RF_TX], 'write_IQ', tx_vec_air(:));
226
227     %Enable the Tx and Rx radios
228     wl_interfaceCmd(node_tx,RF_TX,'tx_en');
229     wl_interfaceCmd(node_rx,RF_RX,'rx_en');
230
231     %Enable the Tx and Rx buffers
232     wl_basebandCmd(node_tx,RF_TX,'tx_buff_en');
233     wl_basebandCmd(node_rx,RF_RX,'rx_buff_en');
234
235     %Trigger the Tx/Rx cycle at both nodes
236     eth_trig.send();
237
238     %Retrieve the received waveform from the Rx node
239     rx_vec_air = wl_basebandCmd(node_rx,[RF_RX],'read_IQ', 0, ...
            TX_NUM_SAMPS);
240     rx_vec_air = rx_vec_air(:).';
241
242     %Disable the Tx/Rx radios and buffers
243     wl_basebandCmd(nodes,'RF_ALL','tx_rx_buff_dis');
244     wl_interfaceCmd(nodes,'RF_ALL','tx_rx_dis');
245 else
246     %Sim-only mode: Apply wireless degradations here for sim ...
            (noise, fading, etc)
247
248     %Perfect Rx=Tx
249     rx_vec_air = tx_vec_air;
250
251     %AWGN:
252     %rx_vec_air = tx_vec_air + ...
            1e-2*complex(randn(1,length(tx_vec_air)), ...
            randn(1,length(tx_vec_air)));
253
254     %CFO:
255     %rx_vec_air = tx_vec_air .* ...
            exp(-1i*2*pi*1e-4*[0:length(tx_vec_air)-1]);
256 end
257
258 %% Decimate
259 if(DECIMATE_RATE == 1)
260     raw_rx_dec = rx_vec_air;
261 elseif(DECIMATE_RATE == 2)
262     raw_rx_dec = filter(interp_filt2, 1, rx_vec_air);
263     raw_rx_dec = raw_rx_dec(1:2:end);
264 end
265
266 %% Correlate for LTS
267
```

```
268 %Complex cross correlation of Rx waveform with time-domain LTS
269 lts_corr = abs(conv(conj(fliplr(lts_t)), sign(raw_rx_dec)));
270
271 %Skip early and late samples
272 lts_corr = lts_corr(32:end-32);
273
274 %Find all correlation peaks
275 lts_peaks = find(lts_corr > LTS_CORR_THRESH*max(lts_corr));
276
277 %Select best candidate correlation peak as LTS-payload boundary
278 [LTS1, LTS2] = meshgrid(lts_peaks,lts_peaks);
279 [lts_second_peak_index,y] = find(LTS2-LTS1 == length(lts_t));
280
281 %Punt if no valid correlation peak was found
282 if(isempty(lts_second_peak_index))
283     fprintf('No LTS Correlation Peaks Found!\n');
284     return;
285 end
286
287 %Set the sample indices of the payload symbols and preamble
288 payload_ind = lts_peaks(max(lts_second_peak_index))+32;
289 lts_ind = payload_ind-160;
290
291 if(DO_APPLY_CFO_CORRECTION)
292     %Extract LTS (not yet CFO corrected)
293     rx_lts = raw_rx_dec(lts_ind : lts_ind+159);
294     rx_lts1 = rx_lts(-64-FFT_OFFSET + [97:160]);
295     rx_lts2 = rx_lts(-FFT_OFFSET + [97:160]);
296
297     %Calculate coarse CFO est
298     rx_cfo_est_lts = mean(unwrap(angle(rx_lts1 .* conj(rx_lts2))));
299     rx_cfo_est_lts = rx_cfo_est_lts/(2*pi*64);
300 else
301     rx_cfo_est_lts = 0;
302 end
303
304 %Apply CFO correction to raw Rx waveform
305 rx_cfo_corr_t = ...
        exp(1i*2*pi*rx_cfo_est_lts*[0:length(raw_rx_dec)-1]);
306 rx_dec_cfo_corr = raw_rx_dec .* rx_cfo_corr_t;
307
308 %Re-extract LTS for channel estimate
309 rx_lts = rx_dec_cfo_corr(lts_ind : lts_ind+159);
310 rx_lts1 = rx_lts(-64-FFT_OFFSET + [97:160]);
311 rx_lts2 = rx_lts(-FFT_OFFSET + [97:160]);
312
313 rx_lts1_f = fft(rx_lts1);
314 rx_lts2_f = fft(rx_lts2);
315
316 %Calculate channel estimate
317 rx_H_est = lts_f .* (rx_lts1_f + rx_lts2_f)/2;
```

```
318 %rx_H_estd = (rx_lts1_f + rx_lts2_f)/2 ./ lts_f;
319
320 %% Rx payload processsing
321
322 %Extract the payload samples (integral number of UFMC symbols ...
        following preamble)
323 payload_vec = rx_dec_cfo_corr(payload_ind : ...
        payload_ind+N_UFMC_SYMS*(N_SC+FILTER_LENGTH-1)-1);
324 payload_mat = reshape(payload_vec, (N_SC+FILTER_LENGTH-1), ...
        N_UFMC_SYMS);
325
326 idftmtx_all = zeros(N_SC*N_PRB, N_SC);
327 filtermtx_rx = [];
328 for i=1:N_PRB
329 %Generate expanded DFT matrix
330 idftmtx_all ((1+(i-1)*N_SC):(i*N_SC), ...
        (1+(i-1)*N_SC/N_PRB):(i*N_SC/N_PRB)) = ...
331 idftmtx(:,(1+(i-1)*N_SC/N_PRB):(i*N_SC/N_PRB));
332
333 %Generate stacked Toeplitz matrices implement multicarrier ...
        demodulation
334 filtermtx_rx = [filtermtx_rx filtermtx{i}];
335 end
336
337 tx_mtx = filtermtx_rx*idftmtx_all;
338 rx_mtx = inv(tx_mtx' * tx_mtx) * tx_mtx';
339 syms_f_mat = rx_mtx * payload_mat;
340
341 %Equalize (zero-forcing, just divide by compled chan estimates)
342 syms_eq_mat = syms_f_mat ./ repmat(rx_H_est.', 1, N_UFMC_SYMS);
343
344 %Extract the pilots and calculate per-symbol phase error
345 pilots_f_mat = syms_eq_mat(SC_IND_PILOTS, :);
346 pilot_phase_err = angle(mean(pilots_f_mat.*pilots_mat));
347 pilot_phase_corr = repmat(exp(-1i*pilot_phase_err), N_SC, 1);
348
349 %Apply the pilot phase correction per symbol
350 syms_eq_pc_mat = syms_eq_mat .* pilot_phase_corr;
351 payload_syms_mat = syms_eq_pc_mat(SC_IND_DATA, :);
352
353 %% Demod
354 rx_syms = reshape(payload_syms_mat, 1, N_DATA_SYMS);
355
356 demod_fcn_bpsk = @(x) double(real(x)>0);
357 demod_fcn_qpsk = @(x) double(2*(real(x)>0) + 1*(imag(x)>0));
358 demod_fcn_16qam = @(x) (8*(real(x)>0)) + ...
        (4*(abs(real(x))<0.6325)) + (2*(imag(x)>0)) + ...
        (1*(abs(imag(x))<0.6325));
359
360 switch(MOD_ORDER)
361     case 2 %BPSK
```

```
362             rx_data = arrayfun(demod_fcn_bpsk, rx_syms);
363         case 4 %QPSK
364             rx_data = arrayfun(demod_fcn_qpsk, rx_syms);
365         case 16 %16-QAM
366             rx_data = arrayfun(demod_fcn_16qam, rx_syms);
367     end
368
369     %% Calculate SNR
370     Signal = 0;
371     Noise = 0;
372
373     for i = 1:N_UFMC_SYMS
374         for j = 1:N_SC
375             Signal = Signal + abs(syms_f_mat(j,i))^2;
376
377             if length(find(SC_NULL == j)) == 1
378                 Noise = Noise + abs(syms_f_mat(j,i))^2;
379             end
380         end
381     end
382
383     Eta = N_NULLSC / N_SC;
384     SNR = (Signal / Noise)*Eta - 1;
385
386     %% Calculate Rx stats
387
388     sym_errs = sum(tx_data ~= rx_data);
```

The results of the implementation are separated into two types. The first type will present the influence of the variation of the different parameters on the signal performance. While the second type consists of a comparison between UFMC and OFDM performance.

UFMC has three parameters that can be varied to obtain different results. These parameters are: filter side-lobe attenuation, number of sub-bands, and filter length. After varying these parameters and executing different tests, the following results have been obtained.

The side-lobe attenuation of the filter has a high influence on the quality of the signal reception. If its value is very low the symbols get dispersed; however, after a certain level it is no longer relevant. In this case, this level is reached after 100 dB. Fig A.1 shows the symbol constellation for different side-lobe attenuation values.

This effect can be corroborated by observing the UFMC signal in the frequency domain. It can be seen how, by changing the filter side-lobe attenuation values, each sub-band has less influence on the adjacent sub-bands. Fig A.2,

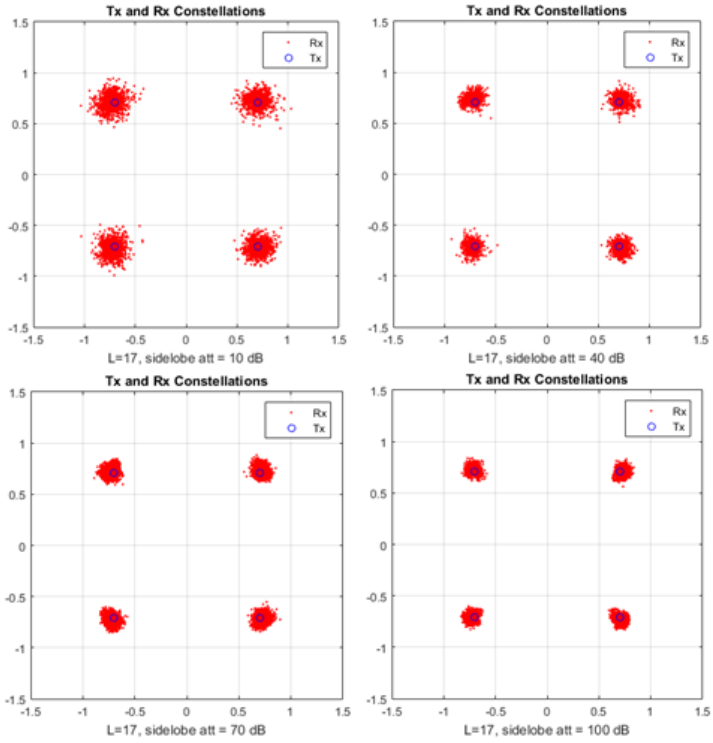

Figure A.1: UFMC signal dispersion according to filter side-lobe attenuation

A.3, A.4, and A.5 show this effect. Although in Fig A.3 (which shows the signal with a side-lobe attenuation of 40 dB) it seems that there is less interference than with larger side-lobe attenuation values, i.e. 70 dB and 100 dB; what actually happens is that in this case, the first side-lobe decreases slowly, generating interference in the other sub-bands. While for the 70 dB and 100 dB cases the secondary lobes are higher than the 40 dB case, giving the impression of having more interference, but actually for the 70 dB and 100 dB cases the first side-lobe decreases abruptly, and therefore there is less interference in the other sub-bands.

Another parameter that influences the UFMC signal is the number of sub-bands into which each symbol is divided. In Fig A.6 a comparison between the constellations of the signal divided into 4 and 8 sub-bands is presented.

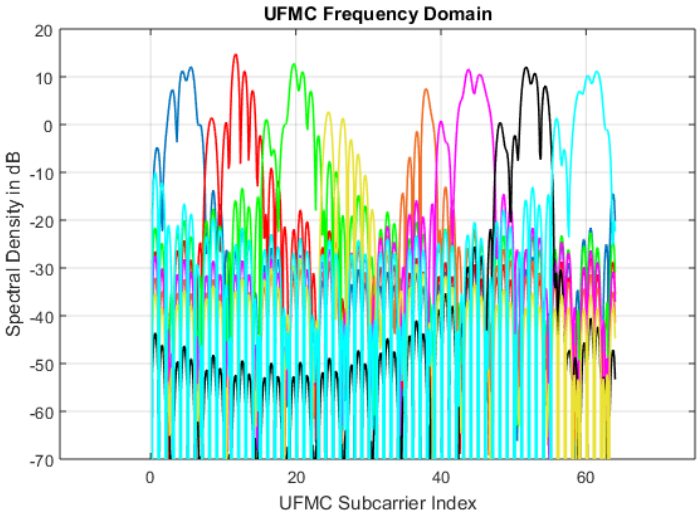

Figure A.2: UFMC signal L = 17, sidelobe att = 10 dB

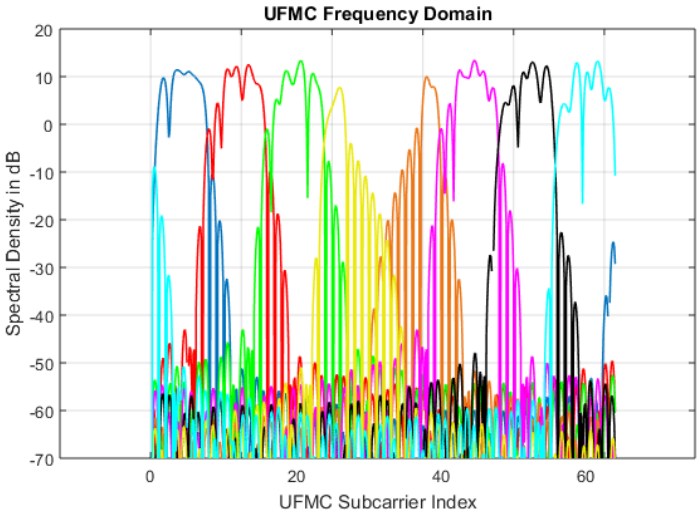

Figure A.3: UFMC signal L = 17, sidelobe att = 40 dB

It can be clearly seen that, in the case of a signal with 64 carriers, dividing each UFMC symbol into 8 sub-bands has better performance than dividing it

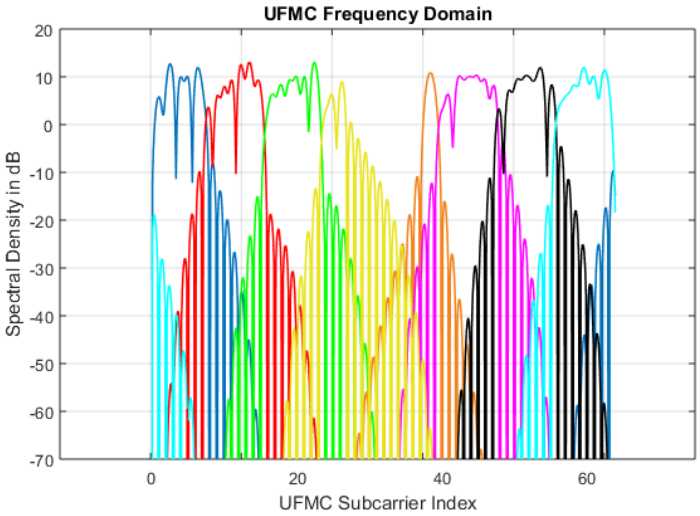

Figure A.4: UFMC signal L = 17, sidelobe att = 70 dB

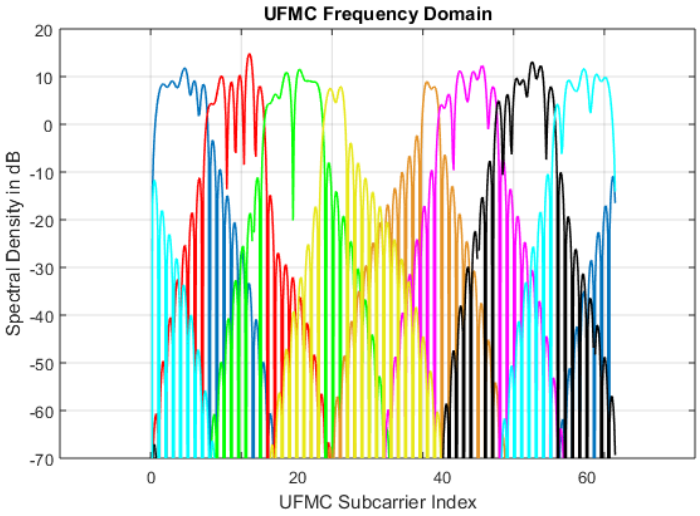

Figure A.5: UFMC signal L = 17, sidelobe att = 100 dB

into 4. This is because the fewer sub-bands there are, the more sub-carriers must be contained in each one of them, and therefore due to the type of filter-

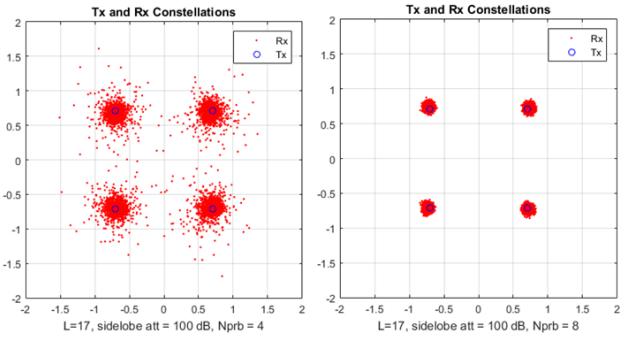

Figure A.6: UFMC constellations with 4 and 8 sub-bands

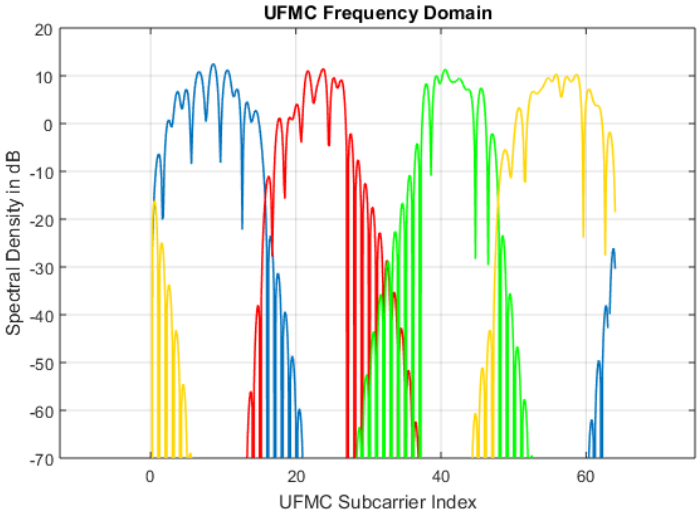

Figure A.7: UFMC signal L = 17, sidelobe att = 100 dB, 4 sub-bands

ing the flat shape in the central band is lost. This implies losing power at the edges of the sub-bands, and if the noise level is high enough, it would prevent the signal from being properly recovered. This behavior can be observed in Fig A.7. It has also been observed that increasing the number of sub-bands for this particular case (L = 17 and rejection band = 100 dB) would not imply any improvement, since 8 sub-bands make the signal is flat enough in the center

band.

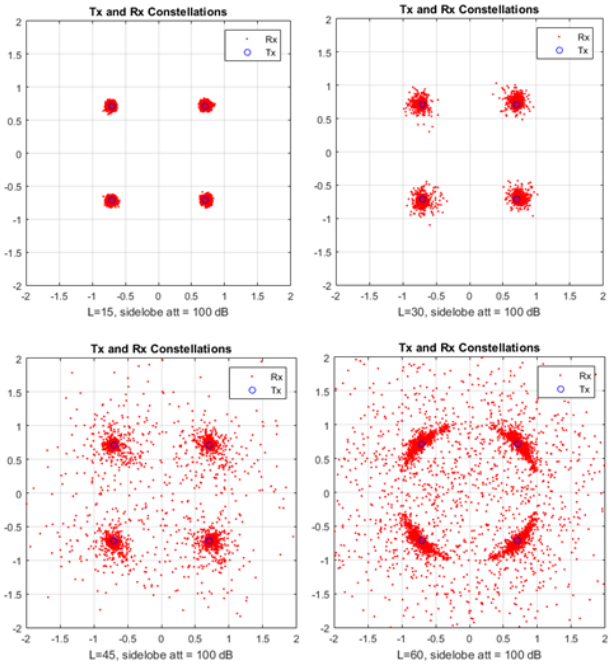

Figure A.8: UFMC signal with different L values, sidelobe att = 100 dB, and 8 sub-bands

The last parameter that remains to be modified is the filter length. Even though to be fairly compared with OFDM, the filter must have a length of 17 samples; in order to see the influence of this parameter on the performance of the system, different comparisons shown in Fig A.8 were made. It is possible to see that as the length of the filter increases, the signal deteriorates.

The reason this happens is that as the length of the filter increases, the sub-band becomes less flat in the central frequency band. This can be noticed by looking at Fig A.9, A.10, A.11, and A.12.

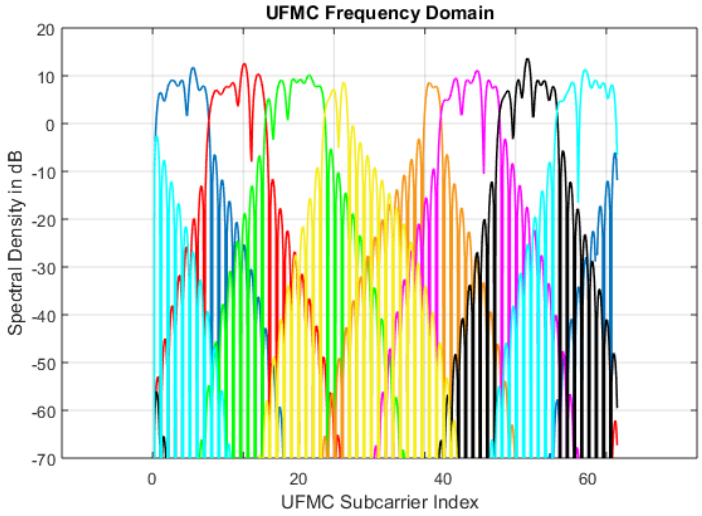

Figure A.9: UFMC signal L = 15, sidelobe att = 100 dB, and 8 sub-bands

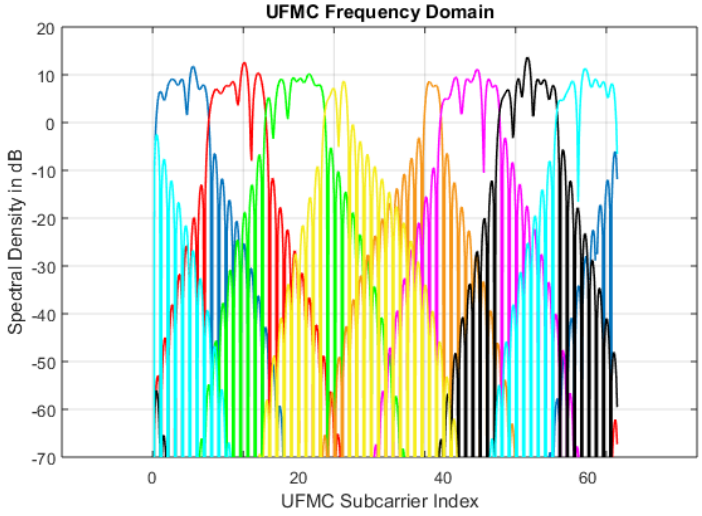

Figure A.10: UFMC signal L = 30, sidelobe att = 100 dB, and 8 sub-bands

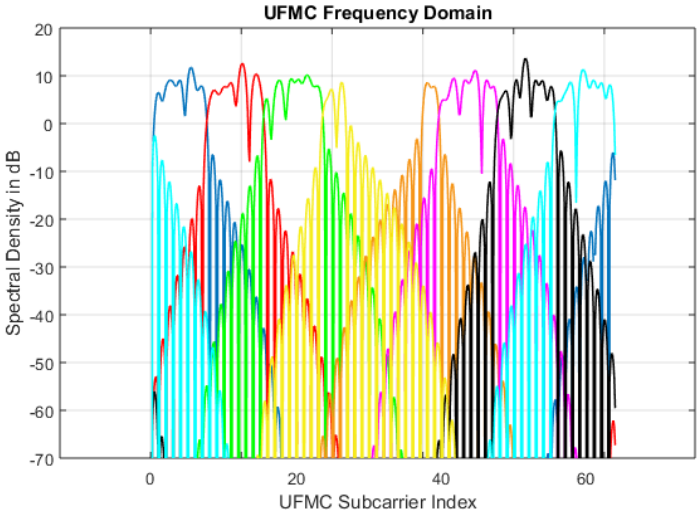

Figure A.11: UFMC signal L = 45, sidelobe att = 100 dB, and 8 sub-bands

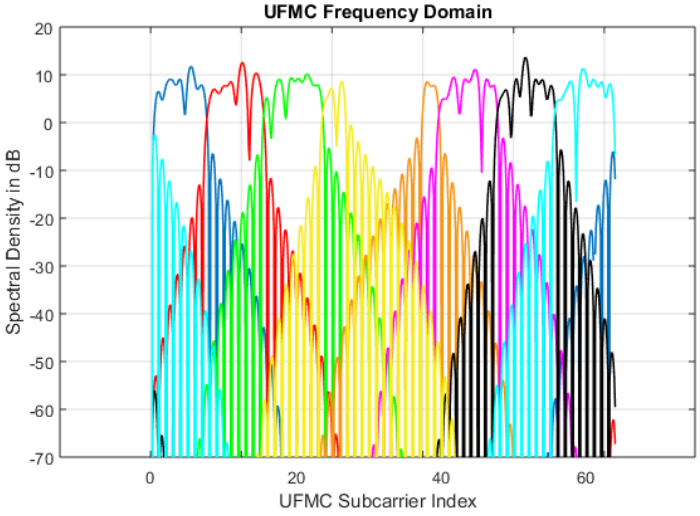

Figure A.12: UFMC signal L = 100, sidelobe att = 100 dB, and 8 sub-bands

If we compare UFMC with OFDM, the most remarkable aspect is the greater spectral efficiency that the first presents over the second. Another aspect that stands out is the low interference between sub-bands that UFMC has compared to OFDM. Both aspects can be appreciated in Fig A.13, where it can be seen that OFDM has its first secondary lobe approximately -15 dB below the maximum, while the other secondary lobes continue with a slow transition; on the other hand, UFMC presents its first secondary lobe approximately -20 dB below the maximum, and the rest of the secondary lobes decay abruptly.

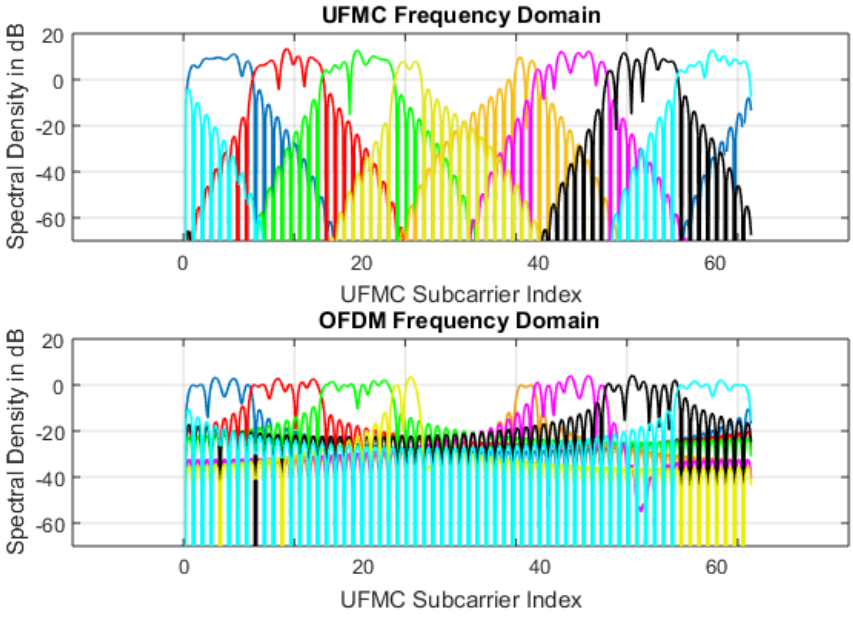

Figure A.13: UFMC and OFDM PSD comparison

The other important aspect to take into account is the performance of both waveforms, measuring the Bit Error Rate (BER) as a function of the Signal to Noise Ratio (SNR). Fig A.14 shows a comparative graph between the SNR vs. BER relationship of OFDM and UFMC.

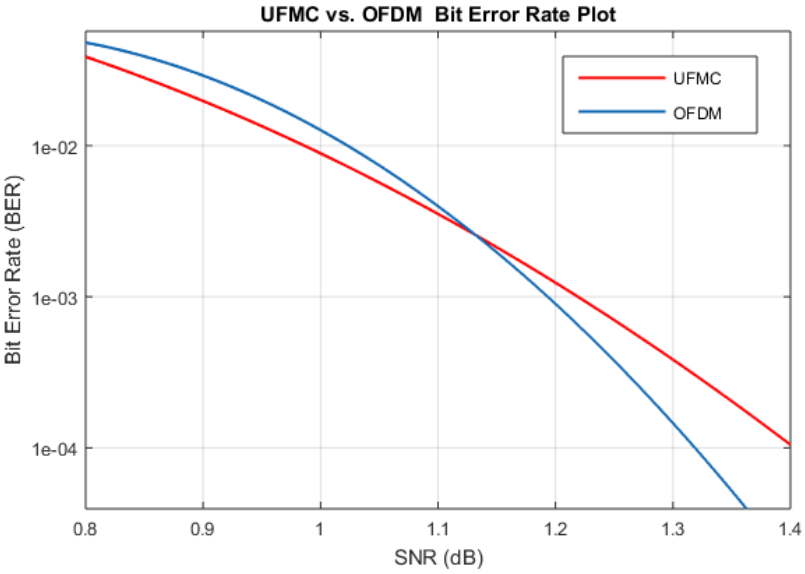

Figure A.14: UFMC and OFDM SNR comparison

A.3 FBMC Code

This section presents the MATLAB code for FBMC.

```
%%%%%%%%%%%%%%%%%%%%%%%%%%%%%%
% wl_example_siso_OQAM-FBMC.m
%%%%%%%%%%%%%%%%%%%%%%%%%%%%%%
 clear

%Params:
USE_WARPLAB_TXRX = 1;     %Enable WARPLab-in-the-loop (otherwise ...
        sim-only)
WRITE_PNG_FILES = 0;      %Enable writing plots to PNG

%Waveform params
N_FBMC_SYMS = 28;         %Number of FBMC symbols
MOD_ORDER = 16;            %Modulation order (4/16 = QPSK/16-QAM). ...
        BPSK not supported in OQAM
TX_SCALE = 1.0;           %Scale for Tx waveform ([0:1])
INTERP_RATE = 2;          %Interpolation rate (1 or 2)

%FBMC params
```

```
17 SC_IND_PILOTS = [8 22 44 58];   %Pilot subcarrier indices
18 SC_IND_DATA   = [2:7 9:21 23:27 39:43 45:57 59:64]; %Data ...
       subcarrier indices
19 SC_NULL = [1 28:38];     %Null subcarrier indices
20 N_SC = 64;               %Number of subcarriers
21 N_NULLSC = 12;           %Number of null subcarriers
22 N_DATA_SYMS = N_FBMC_SYMS * length(SC_IND_DATA); %Number of data ...
       symbols (one per data-bearing subcarrier per FBMC symbol)
23 OVERLAP_FAC = 4;         %Overlap factor
24
25 %Rx processing params
26 FFT_OFFSET = 0;          %Number of CP samples to use in FFT (on ...
       average)
27 LTS_CORR_THRESH = 0.8;  %Normalized threshold for LTS correlation
28 DO_APPLY_CFO_CORRECTION = 0;     %Enable CFO estimation/correction
29 USE_PILOT_TONES = 1;     %Enabel phase error correction
30 DECIMATE_RATE = INTERP_RATE;
31
32 if(USE_WARPLAB_TXRX)
33     fprintf('Using WARPLAB TRRX\n');
34     %%%%%%%%%%%%%%%%%%%%%%%%%%%%%%%
35     % Set up the WARPLab experiment
36     %%%%%%%%%%%%%%%%%%%%%%%%%%%%%%%
37
38     USE_AGC = false;
39
40     NUMNODES = 2;
41
42     %Create a vector of node objects
43     nodes = wl_initNodes(NUMNODES);
44
45     %Create a UDP broadcast trigger and tell each node to be ...
           ready for it
46     eth_trig = wl_trigger_eth_udp_broadcast;
47     wl_triggerManagerCmd(nodes,'add_ethernet_trigger',[eth_trig]);
48
49     %Get IDs for the interfaces on the boards. Since this example ...
           assumes each
50     %board has the same interface capabilities, we only need to ...
           get the IDs
51     %from one of the boards
52     [RFA,RFB] = wl_getInterfaceIDs(nodes(1));
53
54     %Set up the interface for the experiment
55     wl_interfaceCmd(nodes,'RF_ALL','tx_gains',2,15);
56     wl_interfaceCmd(nodes,'RF_ALL','channel',5,20);
57
58     if(USE_AGC)
59         wl_interfaceCmd(nodes,'RF_ALL','rx_gain_mode','automatic');
60         wl_basebandCmd(nodes,'agc_target',-10);
61         wl_basebandCmd(nodes,'agc_trig_delay', 511);
```

```
62      else
63          wl_interfaceCmd(nodes,'RF_ALL','rx_gain_mode','manual');
64          RxGainRF = 2; %Rx RF Gain in [1:3]
65          RxGainBB = 10; %Rx Baseband Gain in [0:31]
66          wl_interfaceCmd(nodes,'RF_ALL','rx_gains',RxGainRF,RxGainBB)
67      end
68
69      TX_NUM_SAMPS = nodes(1).baseband.txIQLen;
70      SAMP_FREQ = wl_basebandCmd(nodes(1),'tx_buff_clk_freq');
71      node_tx = nodes(1);
72      node_rx = nodes(2);
73      RF_TX = RFA;
74      RF_RX = RFA;
75
76      %Set up the baseband for the experiment
77      wl_basebandCmd(nodes,'tx_delay',0);
78      wl_basebandCmd(nodes,'tx_length',TX_NUM_SAMPS);
79      example_mode_string = 'hw';
80  else
81      fprintf('NOT Using WARPLAB\n');
82      %Use sane defaults for hardware-dependent params in sim-only ...
            version
83      TX_NUM_SAMPS = 32768;
84      SAMP_FREQ = 40e6;
85      example_mode_string = 'sim';
86  end
87
88  %Define a halfband 2x interp filter response
89  interp_filt2 = zeros(1,43);
90  interp_filt2([1 3 5 7 9 11 13 15 17 19 21]) = [12 -32 72 -140 252 ...
        -422 682 -1086 1778 -3284 10364];
91  interp_filt2([23 25 27 29 31 33 35 37 39 41 43]) = ...
        interp_filt2(fliplr([1 3 5 7 9 11 13 15 17 19 21]));
92  interp_filt2(22) = 16384;
93  interp_filt2 = interp_filt2./max(abs(interp_filt2));
94
95  HBi = dsp.FIRHalfbandInterpolator('SampleRate',SAMP_FREQ,...
96  'Specification','Filter order and stopband ...
        attenuation','FilterOrder',1720,...
97  'StopbandAttenuation',80);
98  HBi_dec = dsp.FIRHalfbandDecimator('SampleRate',SAMP_FREQ,...
99  'Specification','Filter order and stopband ...
        attenuation','FilterOrder',1720,...
100 'StopbandAttenuation',80);
101
102 %% Define the preamble
103 sts_f = zeros(1,64);
104 sts_f(1:27) = [0 0 0 0 -1-1i 0 0 0 -1-1i 0 0 0 1+1i 0 0 0 1+1i 0 ...
        0 0 1+1i 0 0 0 1+1i 0 0];
105 sts_f(39:64) = [0 0 1+1i 0 0 0 -1-1i 0 0 0 1+1i 0 0 0 -1-1i 0 0 0 ...
        -1-1i 0 0 0 1+1i 0 0 0];
```

```
106 sts_t = ifft(sqrt(13/6).*sts_f, 64);
107 sts_t = sts_t(1:16);
108
109 %LTS for CFO and channel estimation
110 lts_f = [-1 1 -1 -1 1 1 -1 1 -1 1 -1 -1 -1 -1 -1 1 1 -1 -1 1 -1 1 ...
        -1 1 1 1 1 -1 1 -1 1 -1 1 -1 1 -1 1 -1 1 1 -1 -1 1 1 -1 1 -1 ...
        1 1 1 1 1 1 -1 -1 1 1 -1 1 -1 1 1 1 1];
111 lts_t = ifft(lts_f, 64);
112
113 %Use 30 copies of the 16-sample STS for extra AGC settling margin
114 preamble = [repmat(sts_t, 1, 0)  lts_t(33:64) lts_t lts_t];
115
116 %Sanity check inputs
117 if(INTERP_RATE*((N_FBMC_SYMS*2*OVERLAP_FAC * N_SC) + ...
        length(preamble)) > TX_NUM_SAMPS)
118     fprintf('Too many FBMC symbols for TX_NUM_SAMPS!\n');
119     return;
120 end
121
122 %% Generate a payload
123 tx_data = randi(MOD_ORDER, 1, N_DATA_SYMS) - 1;
124
125 %Functions for data -> complex symbol mapping (avoids comm ...
        toolbox requirement for qammod)
126 modvec_bpsk =  (1/sqrt(2))  .* [-1 1];
127 modvec_16qam = (1/sqrt(10)) .* [-3 -1 +3 +1];
128
129 mod_fcn_bpsk = @(x) complex(modvec_bpsk(1+x),0);
130 mod_fcn_qpsk = @(x) complex(modvec_bpsk(1+bitshift(x, -1)), ...
        modvec_bpsk(1+mod(x, 2)));
131 mod_fcn_16qam = @(x) complex(modvec_16qam(1+bitshift(x, -2)), ...
        modvec_16qam(1+mod(x,4)));
132
133 %Map the data values on to complex symbols and create the row ...
        vector with the constellation symbols
134 %for the 'comb' function
135 switch MOD_ORDER
136     %case 2 %BPSK: not supported in OQAM modulation
137         %tx_syms = arrayfun(mod_fcn_bpsk, tx_data);
138     case 4 %QPSK
139         tx_syms = arrayfun(mod_fcn_qpsk, tx_data);
140     case 16 %16-QAM
141         tx_syms = arrayfun(mod_fcn_16qam, tx_data);
142     otherwise
143         fprintf('Invalid MOD_ORDER (%d)!\n', MOD_ORDER);
144         return;
145 end
146
147
148 %Reshape the symbol vector to a matrix with one column per FBMC ...
        symbol
```

```
149 tx_syms_mat = reshape(tx_syms, length(SC_IND_DATA), N_FBMC_SYMS);
150
151
152 %% Symbols Matrix
153
154 %Construct the input data matrix
155 N_OQAM_SYMS = N_FBMC_SYMS*2;
156 data_mat = zeros(length(SC_IND_DATA), N_OQAM_SYMS);
157
158 %OQAM pre-processing
159 for n_fbmc_sym = 1:N_FBMC_SYMS
160     for k = 1:length(SC_IND_DATA)
161         if(mod(k,2))
162             data_mat(k,(2*n_fbmc_sym-1)) = ...
                    real(tx_syms_mat(k,n_fbmc_sym));
163             data_mat(k,2*n_fbmc_sym) = ...
                    imag(tx_syms_mat(k,n_fbmc_sym));
164         else
165             data_mat(k,(2*n_fbmc_sym-1)) = ...
                    imag(tx_syms_mat(k,n_fbmc_sym));
166             data_mat(k,2*n_fbmc_sym) = ...
                    real(tx_syms_mat(k,n_fbmc_sym));
167         end
168     end
169 end
170
171 for n_oqam_sym = 1:N_OQAM_SYMS
172     for k = 1:length(SC_IND_DATA)
173         data_mat(k,n_oqam_sym) = data_mat(k,n_oqam_sym) * ...
                (1i^(n_oqam_sym-1+k-1));
174     end
175 end
176
177
178 %Define the pilot tones
179 if(USE_PILOT_TONES)
180     pilots = [1 1 -1 1].';
181 else
182     pilots = [0 0 0 0].';
183 end
184
185 %Repeat the pilots across all FBMC symbols
186 pilots_mat = repmat(pilots, 1, N_OQAM_SYMS);
187
188 symbols_mat = zeros(N_SC, N_OQAM_SYMS);
189 symbols_mat(SC_IND_DATA,:) = data_mat;
190 symbols_mat(SC_IND_PILOTS,:) = pilots_mat;
191
192 %% Filtering
193
194 %Prototype filter (changes according to the overlap factor)
```

```
%Prototype filter in frequency domain
switch OVERLAP_FAC
    case 1
        prot_filter_f = [1];
    case 2
        prot_filter_f = [sqrt(2)/2 1 sqrt(2)/2];
    case 3
        prot_filter_f = [0.411438 0.911438 1 0.911438 0.411438];
    case 4
        prot_filter_f = [0.235147 sqrt(2)/2 0.971960 1 0.971960 ...
            sqrt(2)/2 0.235147];
end

%Construct the filter matrix
fftSize_fbmc = N_SC*OVERLAP_FAC;

freqSpread_mat = zeros(N_SC, fftSize_fbmc);
    for idx=1:(N_SC-1)
        freqSpread_mat(idx,(1+(idx-1)*(OVERLAP_FAC)):((idx+1)*...
        ... (OVERLAP_FAC)-1)) = prot_filter_f;
    end
freqSpread_mat(N_SC,1:(OVERLAP_FAC-1))=prot_filter_f((end...
-OVERLAP_FAC+2):end);
freqSpread_mat(N_SC,(end-OVERLAP_FAC+1):end)=prot_filter_f(1:(end...
-OVERLAP_FAC+1));


%Filter the input matrix
for n_sym = 1:N_OQAM_SYMS
    filtered_symbols_mat(:,n_sym) = symbols_mat(:,n_sym).' * ...
        freqSpread_mat;
end


%%IFFT
tx_payload = ifft(filtered_symbols_mat, fftSize_fbmc, 1);


%%P/S converter
tx_payload_vec = reshape(tx_payload, 1, numel(tx_payload));

%%Construct the full time-domain FBMC waveform
tx_vec = [preamble tx_payload_vec];

%%Pad with zeros for transmission
tx_vec_padded = [tx_vec ...
    zeros(1,(TX_NUM_SAMPS/INTERP_RATE)-length(tx_vec))];

%% Interpolate
if(INTERP_RATE == 1)
    tx_vec_air = tx_vec_padded;
```

```
243  elseif(INTERP_RATE == 2)
244  %      tx_vec_2x = zeros(1, 2*numel(tx_vec_padded));
245  %      tx_vec_2x(1:2:end) = tx_vec_padded;
246  %      tx_vec_air = filter(interp_filt2, 1, tx_vec_2x);
247
248      tx_vec_air = step(HBi, tx_vec_padded');
249      tx_vec_air = tx_vec_air';
250  end
251
252  %Scale the Tx vector
253  tx_vec_air = TX_SCALE .* tx_vec_air ./ max(abs(tx_vec_air));
254
255  %% WARPLab Tx/Rx
256  if(USE_WARPLAB_TXRX)
257      %Write the Tx waveform to the Tx node
258      wl_basebandCmd(node_tx,[RF_TX], 'write_IQ', tx_vec_air(:));
259
260      %Enable the Tx and Rx radios
261      wl_interfaceCmd(node_tx,RF_TX,'tx_en');
262      wl_interfaceCmd(node_rx,RF_RX,'rx_en');
263
264      %Enable the Tx and Rx buffers
265      wl_basebandCmd(node_tx,RF_TX,'tx_buff_en');
266      wl_basebandCmd(node_rx,RF_RX,'rx_buff_en');
267
268      %Trigger the Tx/Rx cycle at both nodes
269      eth_trig.send();
270
271      %Retrieve the received waveform from the Rx node
272      rx_vec_air = wl_basebandCmd(node_rx,[RF_RX],'read_IQ', 0, ...
             TX_NUM_SAMPS);
273      rx_vec_air = rx_vec_air(:).';
274
275      %Disable the Tx/Rx radios and buffers
276      wl_basebandCmd(nodes,'RF_ALL','tx_rx_buff_dis');
277      wl_interfaceCmd(nodes,'RF_ALL','tx_rx_dis');
278  else
279      %Sim-only mode: Apply wireless degradations here for sim ...
             (noise, fading, etc)
280
281      %Perfect Rx=Tx
282      rx_vec_air = tx_vec_air;
283
284      %AWGN:
285  %      rx_vec_air = tx_vec_air + ...
       10e-2*complex(randn(1,length(tx_vec_air)), ...
       randn(1,length(tx_vec_air)));
286
287      %CFO:
288      %rx_vec_air = tx_vec_air .* ...
             exp(-1i*2*pi*1e-4*[0:length(tx_vec_air)-1]);
```

```
289 end
290
291 %% Decimate
292 if(DECIMATE_RATE == 1)
293     raw_rx_dec = rx_vec_air;
294 elseif(DECIMATE_RATE == 2)
295 %     raw_rx_dec = filter(interp_filt2, 1, rx_vec_air);
296 %     raw_rx_dec = raw_rx_dec(1:2:end);
297
298     raw_rx_dec = step(HBi_dec, rx_vec_air');
299     raw_rx_dec = raw_rx_dec';
300 end
301
302 %% Correlate for LTS
303
304 %Complex cross correlation of Rx waveform with time-domain LTS
305 lts_corr = abs(conv(conj(fliplr(lts_t)), sign(raw_rx_dec)));
306
307 %Skip early and late samples
308 lts_corr = lts_corr(32:end-32);
309
310 %Find all correlation peaks
311 lts_peaks = find(lts_corr > LTS_CORR_THRESH*max(lts_corr));
312
313 %Select best candidate correlation peak as LTS-payload boundary
314 [LTS1, LTS2] = meshgrid(lts_peaks,lts_peaks);
315 [lts_second_peak_index,y] = find(LTS2-LTS1 == length(lts_t));
316
317 %Punt if no valid correlation peak was found
318 if(isempty(lts_second_peak_index))
319     fprintf('No LTS Correlation Peaks Found!\n');
320     return;
321 end
322
323 %Set the sample indices of the payload symbols and preamble
324 payload_ind = lts_peaks(max(lts_second_peak_index))+32;
325 lts_ind = payload_ind-160;
326
327 if(DO_APPLY_CFO_CORRECTION)
328     %Extract LTS (not yet CFO corrected)
329     rx_lts = raw_rx_dec(lts_ind : lts_ind+159);
330     rx_lts1 = rx_lts(-64-FFT_OFFSET + [97:160]);
331     rx_lts2 = rx_lts(-FFT_OFFSET + [97:160]);
332
333     %Calculate coarse CFO est
334     rx_cfo_est_lts = mean(unwrap(angle(rx_lts1 .* conj(rx_lts2))));
335     rx_cfo_est_lts = rx_cfo_est_lts/(2*pi*64);
336 else
337     rx_cfo_est_lts = 0;
338 end
339
```

```
340 %Apply CFO correction to raw Rx waveform
341 rx_cfo_corr_t = ...
        exp(1i*2*pi*rx_cfo_est_lts*[0:length(raw_rx_dec)-1]);
342 rx_dec_cfo_corr = raw_rx_dec .* rx_cfo_corr_t;
343
344 %Re-extract LTS for channel estimate
345 rx_lts = rx_dec_cfo_corr(lts_ind : lts_ind+159);
346 rx_lts1 = rx_lts(-64-FFT_OFFSET + [97:160]);
347 rx_lts2 = rx_lts(-FFT_OFFSET + [97:160]);
348
349 rx_lts1_f = fft(rx_lts1);
350 rx_lts2_f = fft(rx_lts2);
351
352 %Calculate channel estimate
353 % rx_H_est = lts_f .* (rx_lts1_f + rx_lts2_f)/2;
354 rx_H_est = (rx_lts1_f + rx_lts2_f)/2 ./ lts_f;
355
356 %% Rx payload processing
357
358 %Extract the payload samples (integral number of FBMC symbols ...
        following preamble)
359 payload_vec = rx_dec_cfo_corr(payload_ind : ...
        payload_ind+N_OQAM_SYMS*fftSize_fbmc-1);
360 payload_mat = reshape(payload_vec, fftSize_fbmc, N_OQAM_SYMS);
361
362 %FFT
363 payload_mat_FD = fft(payload_mat, fftSize_fbmc, 1);
364
365 %Reverse filtering action
366 syms_f_mat = zeros(N_SC, N_OQAM_SYMS);
367 for n_sym = 1:N_OQAM_SYMS
368     syms_f_mat(:,n_sym) = ...
            payload_mat_FD(OVERLAP_FAC:OVERLAP_FAC:end, n_sym);
369 end
370
371 %Equalize (zero-forcing, just divide by compled chan estimates)
372 syms_eq_mat = syms_f_mat ./ repmat(rx_H_est.', 1, N_OQAM_SYMS);
373
374 %Extract the pilots and calculate per-symbol phase error
375 pilots_f_mat = syms_eq_mat(SC_IND_PILOTS, :);
376 pilot_phase_err = angle(mean(pilots_f_mat.*pilots_mat));
377 pilot_phase_corr = repmat(exp(-1i*pilot_phase_err), N_SC, 1);
378
379 %Apply the pilot phase correction per symbol
380 syms_eq_pc_mat = syms_eq_mat .* pilot_phase_corr;
381 data_eq_pc_mat = syms_eq_pc_mat(SC_IND_DATA,:);
382
383
384 %%OQAM post-processing
385
386 for n_oqam_sym = 1:N_OQAM_SYMS
```

```
387         for k = 1:length(SC_IND_DATA)
388             data_eq_pc_mat(k,n_oqam_sym) = ...
                    data_eq_pc_mat(k,n_oqam_sym) * ...
                    ((-1i)^(n_oqam_sym-1+k-1));
389         end
390     end
391
392     payload_syms_mat = zeros(length(SC_IND_DATA), N_FBMC_SYMS);
393
394     for n_fbmc_sym = 1:N_FBMC_SYMS
395         for k = 1:length(SC_IND_DATA)
396             if(mod(k,2))
397                 payload_syms_mat(k,n_fbmc_sym) = ...
                        data_eq_pc_mat(k,(2*n_fbmc_sym-1)) + ...
                        1i*data_eq_pc_mat(k,2*n_fbmc_sym);
398             else
399                 payload_syms_mat(k,n_fbmc_sym) = ...
                        data_eq_pc_mat(k,2*n_fbmc_sym) + ...
                        1i*data_eq_pc_mat(k,(2*n_fbmc_sym-1));
400             end
401         end
402     end
403
404     %% Demod
405
406     rx_syms = reshape(payload_syms_mat, 1, N_DATA_SYMS);
407
408     demod_fcn_bpsk = @(x) double(real(x)>0);
409     demod_fcn_qpsk = @(x) double(2*(real(x)>0) + 1*(imag(x)>0));
410     demod_fcn_16qam = @(x) (8*(real(x)>0)) + ...
            (4*(abs(real(x))<0.6325)) + (2*(imag(x)>0)) + ...
            (1*(abs(imag(x))<0.6325));
411
412     switch(MOD_ORDER)
413         case 2 %BPSK
414             rx_data = arrayfun(demod_fcn_bpsk, rx_syms);
415         case 4 %QPSK
416             rx_data = arrayfun(demod_fcn_qpsk, rx_syms);
417         case 16 %16-QAM
418             rx_data = arrayfun(demod_fcn_16qam, rx_syms);
419     end
420
421     Signal = 0;
422     Noise = 0;
423
424     for j = 1:N_SC
425         Signal = Signal + abs(rx_H_est(j)*lts_f(j))^2;
426         Noise = Noise + abs(rx_lts2_f(j) - rx_H_est(j)*lts_f(j))^2;
427     end
428
429     SNR = Signal/Noise;
```

```
430 SNR_dB = 10*log10(SNR);
431
432 %% Calculate Rx stats
```

Appendix B

Total Interference Graphs per Scenario

This appendix contains the total interference graphs for each 5G scenario described in 5.3, that is, according to the different channel models, user equipment speeds, and the 5G NR numerologies.

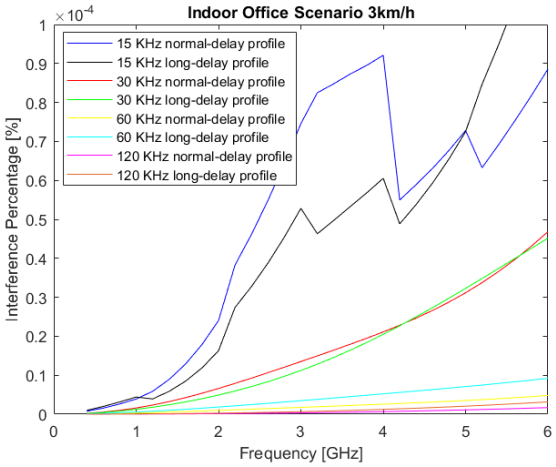

Figure B.1: Total Interference for an Indoor scenario at 3 km/h and < 6 GHz band

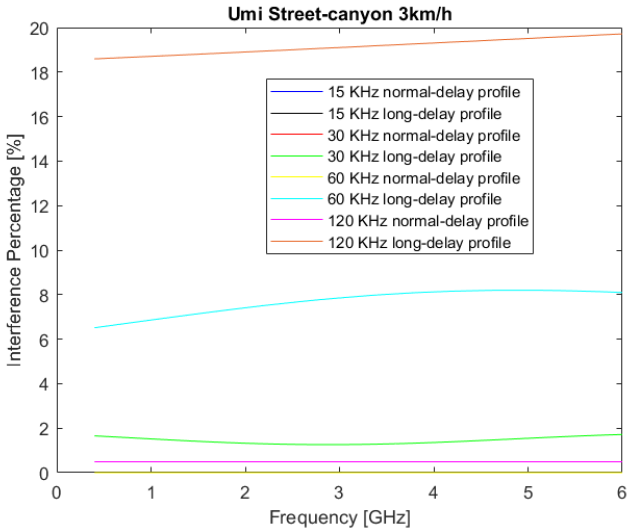

Figure B.2: Total Interference for an UMi Street-canyon scenario at 3 km/h and < 6 GHz band

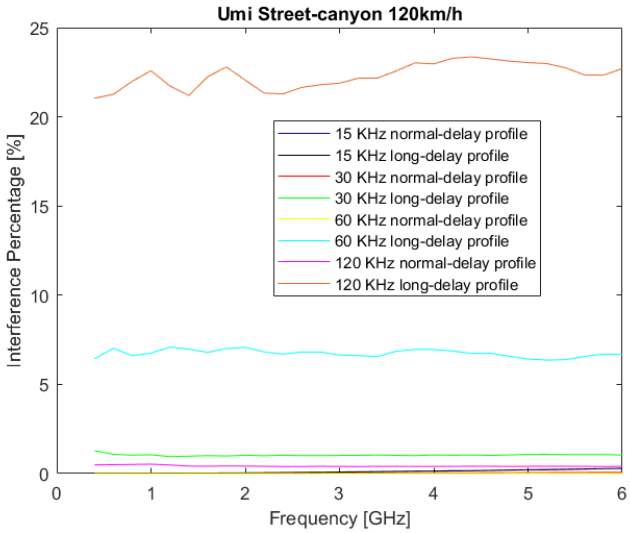

Figure B.3: Total Interference for an UMi Street-canyon scenario at 120 km/h and < 6 GHz band

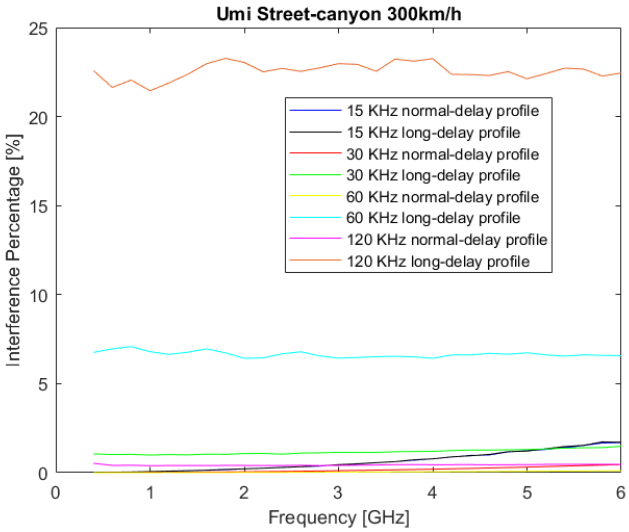

Figure B.4: Total Interference for an UMi Street-canyon scenario at 300 km/h and < 6 GHz band

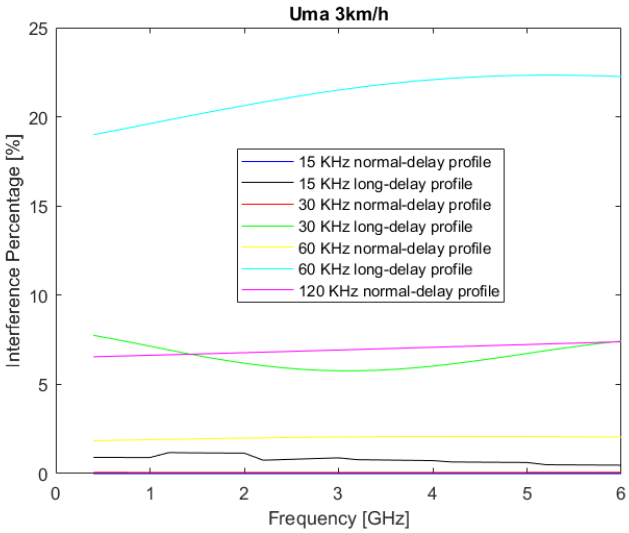

Figure B.5: Total Interference for an UMa scenario at 3 km/h and < 6 GHz band

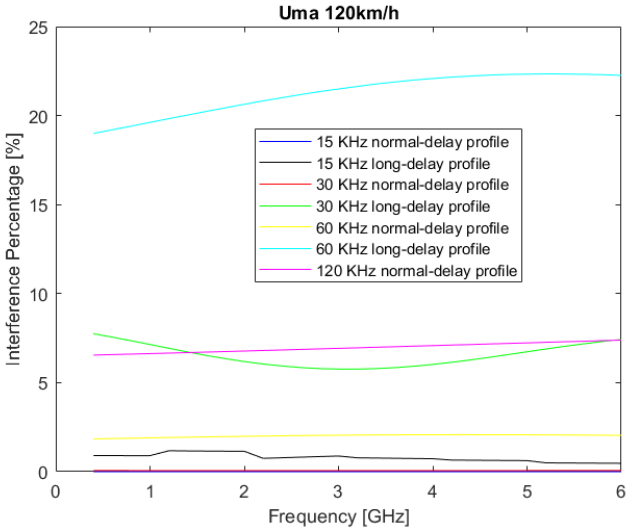

Figure B.6: Total Interference for an UMa scenario at 120 km/h and < 6 GHz band

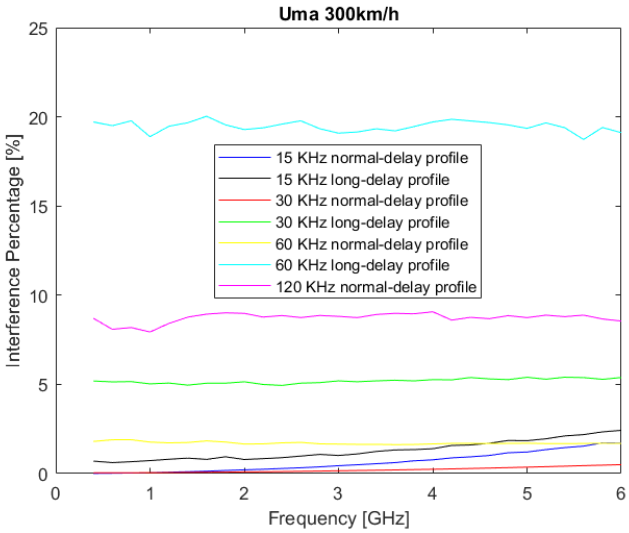

Figure B.7: Total Interference for an UMa scenario at 300 km/h and < 6 GHz band

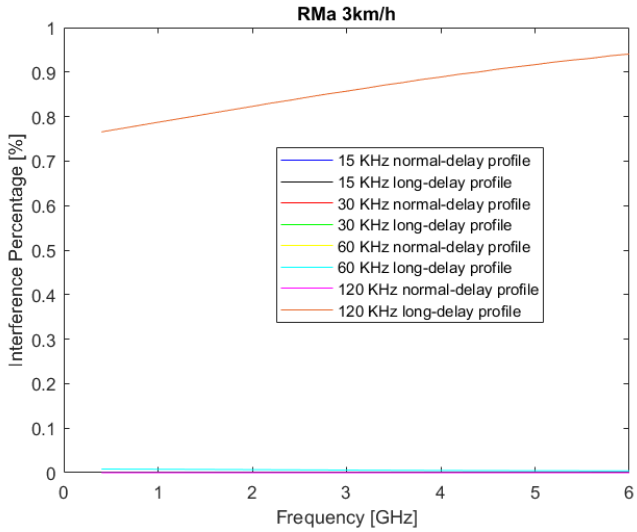

Figure B.8: Total Interference for an RMa scenario at 3 km/h and < 6 GHz band

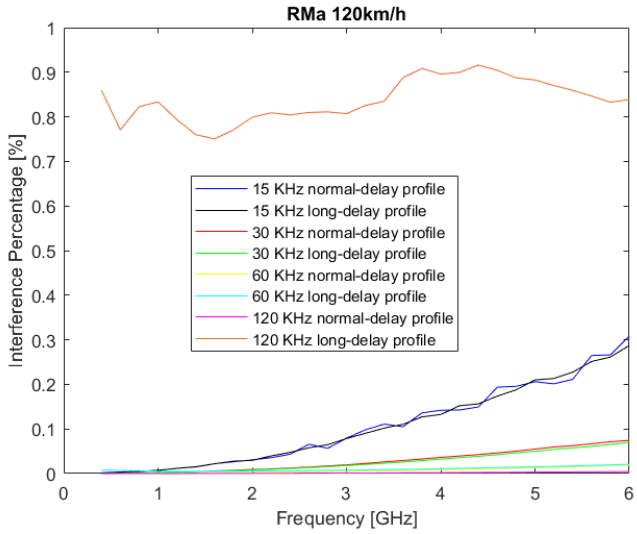

Figure B.9: Total Interference for an RMa scenario at 120 km/h and < 6 GHz band

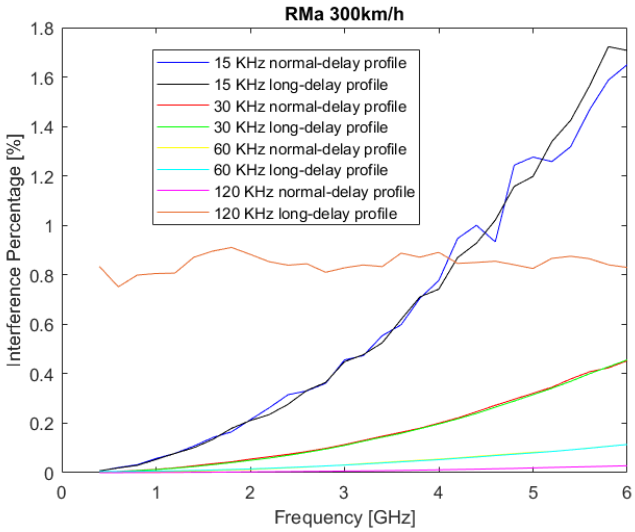

Figure B.10: Total Interference for an RMa scenario at 300 km/h and < 6 GHz band

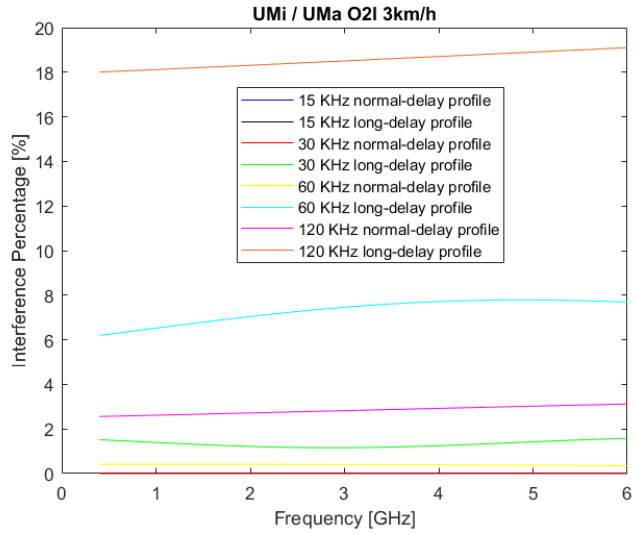

Figure B.11: Total Interference for an UMi/UMa O2I scenario at 3 km/h and < 6 GHz band

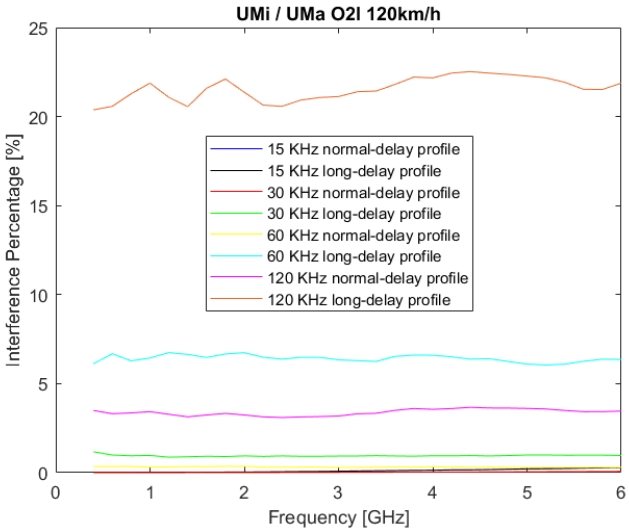

Figure B.12: Total Interference for an UMi/UMa O2I scenario at 120 km/h and < 6 GHz band

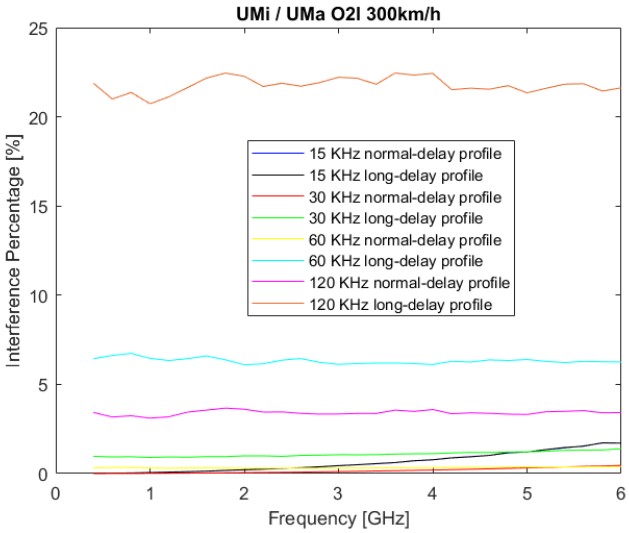

Figure B.13: Total Interference for an UMi/UMa O2I scenario at 300 km/h and < 6 GHz band

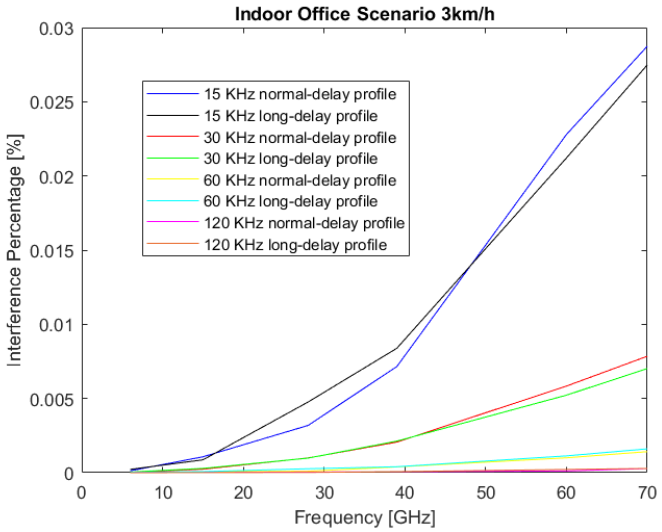

Figure B.14: Total Interference for an Indoor scenario at 3 km/h and > 6 GHz band

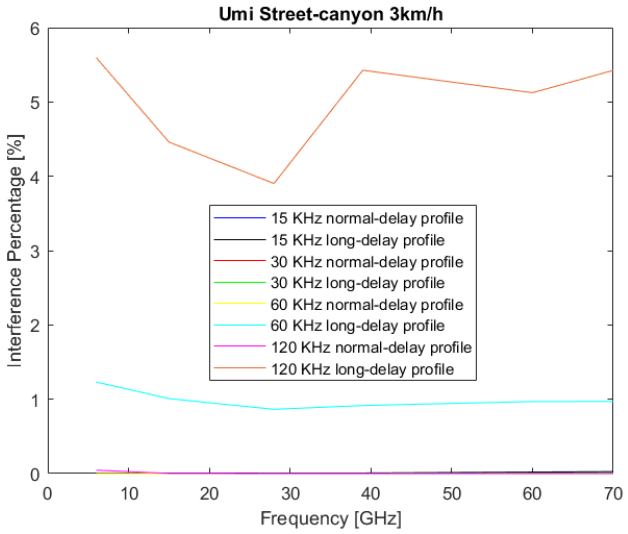

Figure B.15: Total Interference for an UMi Street-canyon scenario at 3 km/h and > 6 GHz band

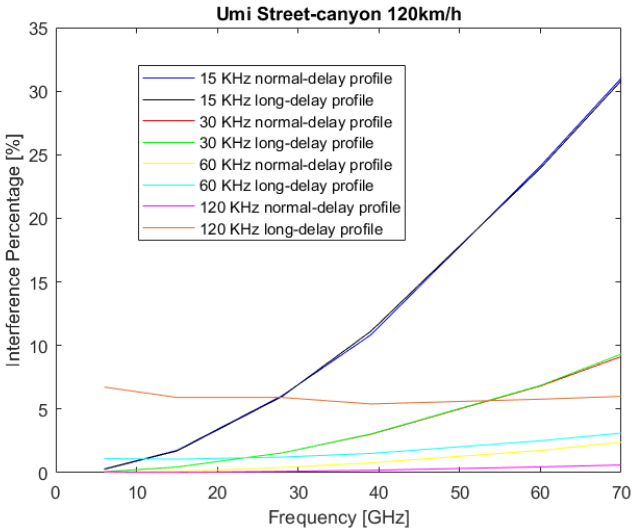

Figure B.16: Total Interference for an UMi Street-canyon scenario at 120 km/h and > 6 GHz band

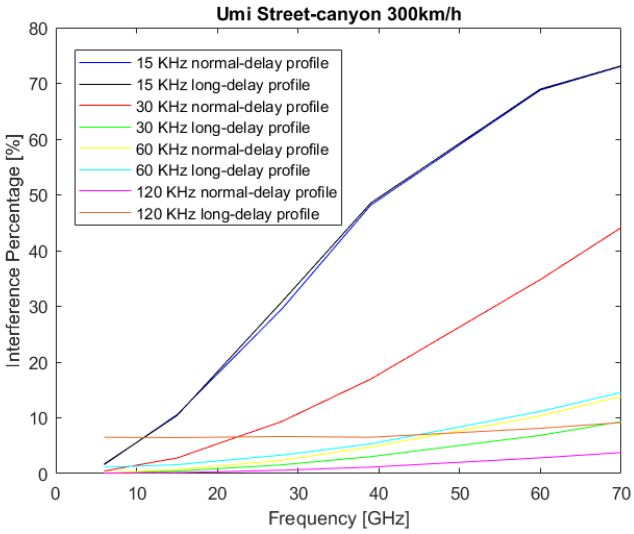

Figure B.17: Total Interference for an UMi Street-canyon scenario at 300 km/h and > 6 GHz band

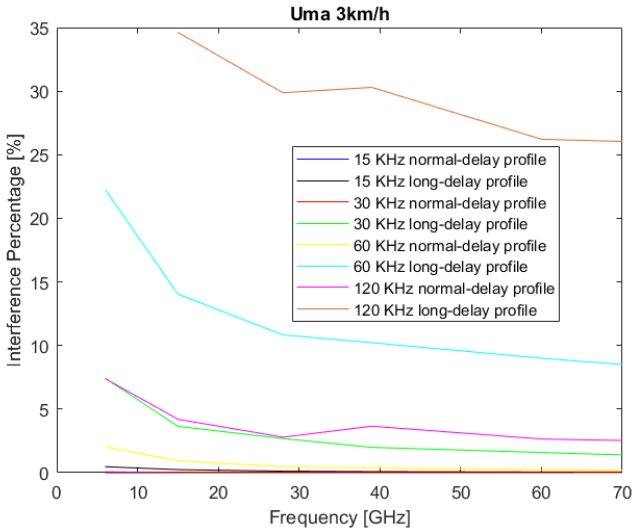

Figure B.18: Total Interference for an UMa scenario at 3 km/h and > 6 GHz band

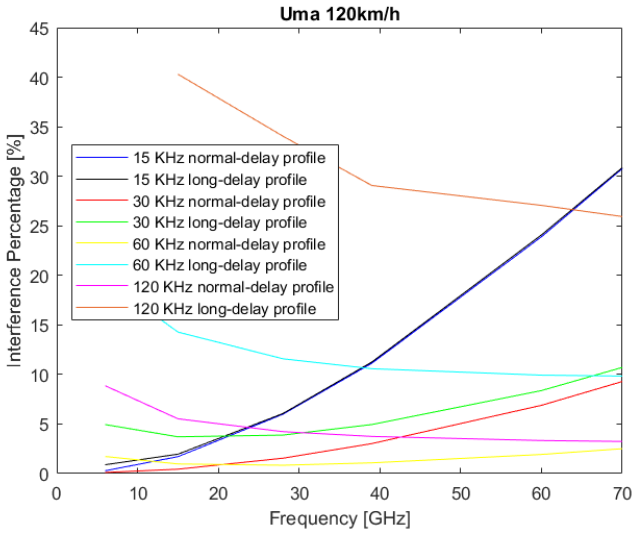

Figure B.19: Total Interference for an UMa scenario at 120 km/h and > 6 GHz band

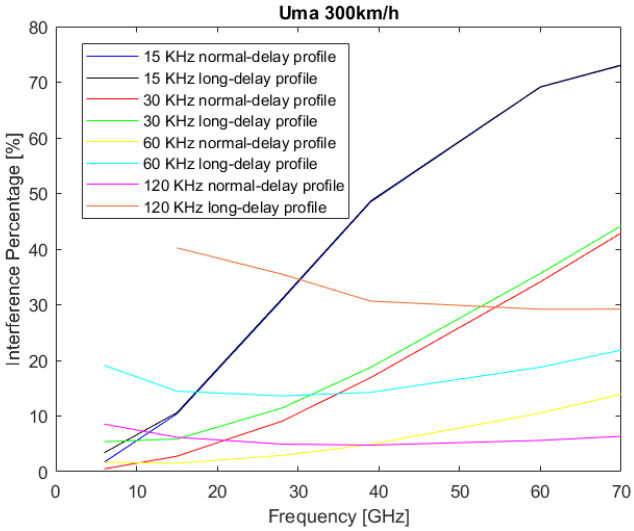

Figure B.20: Total Interference for an UMa scenario at 300 km/h and > 6 GHz band

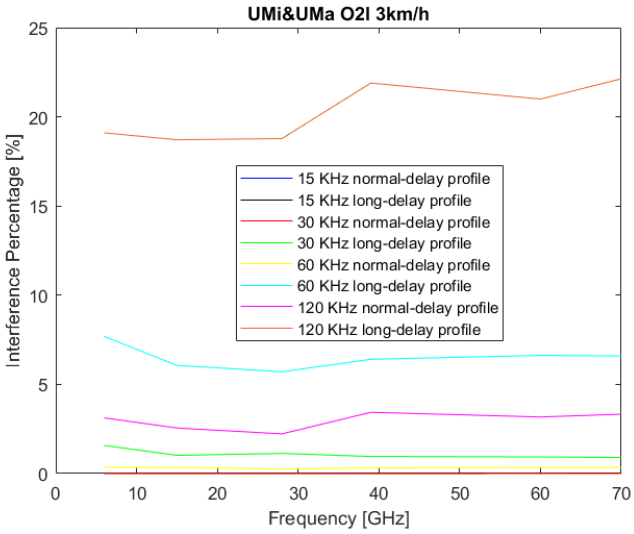

Figure B.21: Total Interference for an UMi/UMa O2I scenario at 3 km/h and > 6 GHz band

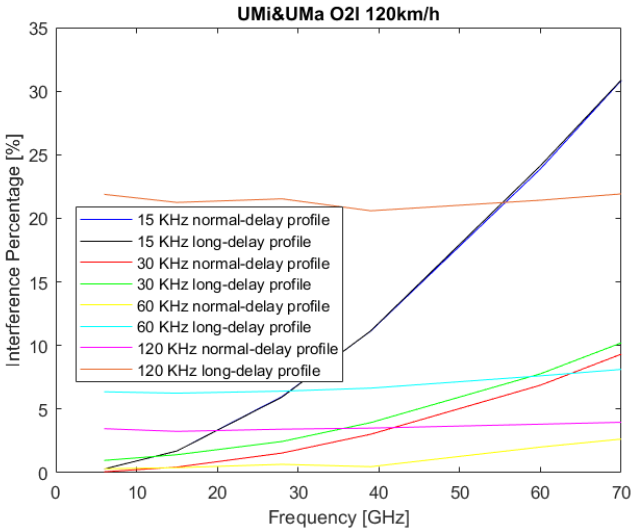

Figure B.22: Total Interference for an UMi/UMa O2I scenario at 120 km/h and > 6 GHz band

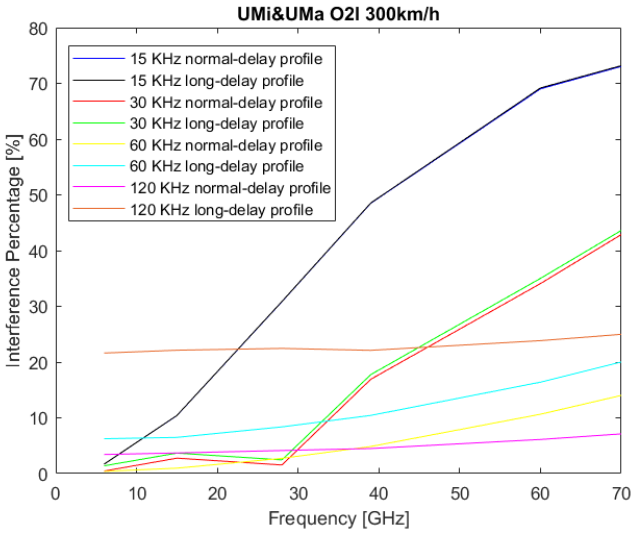

Figure B.23: Total Interference for an UMi/UMa O2I scenario at 300 km/h and > 6 GHz band

References

[1] Kalyani, Vijay Laxmi and Sharma, Deeksha, "IoT: Machine to machine (M2M), device to device (D2D) Internet of everything (IoE) and human to human (H2H): Future of communication," *J. Manag. Eng. Inf. Technol*, vol. 2, pp. 17–23, 2015.

[2] L. Militano, G. Araniti, M. Condoluci, I. Farris, and A. Iera, "Device-to-device communications for 5G internet of things," *EAI Endorsed Trans. Internet Things*, vol. 1, no. 1, pp. 1–15, 2015.

[3] S. Agrawal and K. Sharma, "5G millimeter wave (mmWave) communications," in *2016 3rd International Conference on Computing for Sustainable Global Development (INDIACom)*. IEEE, 2016, pp. 3630–3634.

[4] M. Giordani, M. Mezzavilla, and M. Zorzi, "Initial access in 5G mmWave cellular networks," *IEEE Communications Magazine*, vol. 54, no. 11, pp. 40–47, 2016.

[5] ITU-R, "Spectrum requirements for International Mobile Telecommunications-2000 (IMT-2000)," ITU, Tech. Rep. M.2023-0, Jan 2000.

[6] ITU-R, "Requirements related to technical performance for IMT-Advanced radio interface(s)," ITU, Tech. Rep. M.2134-0, Nov 2008.

[7] ITU-R, "Minimum requirements related to technical performance for IMT-2020 radio interface(s)," ITU, Tech. Rep. M.2410-0, Nov 2017.

[8] ITU-R, "Workplan, timeline, process and deliverables," 2015.

[9] 3GPP TSG SA, "Release 14 Description," 3GPP, Tech. Rep. 21.914 v14.0.0, May 2018.

[10] 3GPP TSG SA, "Release 15 Description," 3GPP, Tech. Rep. 21.915 v1.1.0, Mar 2019.

[11] 3GPP TSG RAN, ""5G" timeline in 3GPP," 3GPP, SP 150149, Mar 2015.

[12] ITU-R, "IMT Vision – Framework and overall objectives of the future development of IMT for 2020 and beyond," ITU, Tech. Rep. M.2083-0, Sep 2015.

[13] W. Shi, J. Cao, Q. Zhang, Y. Li, and L. Xu, "Edge computing: Vision and challenges," *IEEE Internet of Things Journal*, vol. 3, no. 5, pp. 637–646, 2016.

[14] W. Shi and S. Dustdar, "The promise of edge computing," *Computer*, vol. 49, no. 5, pp. 78–81, 2016.

[15] I. Stojmenovic and S. Wen, "The fog computing paradigm: Scenarios and security issues," in *2014 Federated Conference on Computer Science and Information Systems*. IEEE, 2014, pp. 1–8.

[16] F. Bonomi, R. Milito, P. Natarajan, and J. Zhu, "Fog computing: A platform for internet of things and analytics," in *Big data and internet of things: A roadmap for smart environments*. Springer, 2014, pp. 169–186.

[17] L. M. Vaquero and L. Rodero-Merino, "Finding your way in the fog: Towards a comprehensive definition of fog computing," *ACM SIGCOMM Computer Communication Review*, vol. 44, no. 5, pp. 27–32, 2014.

[18] G. K. Tran, H. Nishiuchi, V. Frascolla, K. Takinami, A. De Domenico, E. C. Strinati, T. Haustein, K. Sakaguchi, S. Barbarossa, S. Barberis, and K. Yunoki, "Architecture of mmWave Edge Cloud in 5G-MiEdge," *2018 IEEE International Conference on Communications Workshops (ICC Workshops)*, pp. 1–6, May 2018.

[19] D3.2, "Integration of mmWave edge cloud into 5G mobile networks," Feb 2019.

[20] Y. C. Hu, M. Patel, D. Sabella, N. Sprecher, and V. Young, "Mobile edge computing—A key technology towards 5G," *ETSI white paper*, vol. 11, no. 11, pp. 1–16, 2015.

[21] D. Kreutz, F. Ramos, P. Verissimo, C. E. Rothenberg, S. Azodolmolky, and S. Uhlig, "Software-defined networking: A comprehensive survey," *arXiv preprint arXiv:1406.0440*, 2014.

[22] M. Peng, S. Yan, K. Zhang, and C. Wang, "Fog computing based radio access networks: Issues and challenges," *arXiv preprint arXiv:1506.04233*, 2015.

[23] 3GPP TSG RAN, "Support for Ultra-Reliable Low Latency Communication (URLLC)," 3GPP, Tech. Rep. R2-164130, May 2016.

[24] C. V. N. Index, "Cisco annual internet report, 2018–2023 white paper," *Cisco: San Jose, CA, USA*, 2020.

[25] D2.3, "Components of a new air interface - building blocks and performance," May 2014.

[26] J. Abdoli, M. Jia, and J. Ma, "Filtered OFDM: A new waveform for future wireless systems," in *2015 IEEE 16th International Workshop on Signal Processing Advances in Wireless Communications (SPAWC)*. IEEE, 2015, pp. 66–70.

[27] T. Wild, F. Schaich, and Y. Chen, "5G air interface design based on universal filtered (UF-) OFDM," in *2014 19th International Conference on Digital Signal Processing*. IEEE, 2014, pp. 699–704.

[28] Z. Zhao, M. Schellmann, X. Gong, Q. Wang, R. Böhnke, and Y. Guo, "Pulse shaped OFDM for 5G systems," *arXiv preprint arXiv:1605.03731*, 2016.

[29] C. An, B. Kim, and H.-G. Ryu, "Design of W-OFDM and nonlinear performance comparison for 5G waveform," in *2016 International Conference on Information and Communication Technology Convergence (ICTC)*. IEEE, 2016, pp. 1006–1009.

[30] G. Berardinelli, K. I. Pedersen, T. B. Sorensen, and P. Mogensen, "Generalized DFT-spread-OFDM as 5G waveform," *IEEE Communications Magazine*, vol. 54, no. 11, pp. 99–105, 2016.

[31] A. Farhang, N. Marchetti, and L. E. Doyle, "Low-complexity modem design for GFDM," *IEEE Transactions on Signal Processing*, vol. 64, no. 6, pp. 1507–1518, 2015.

[32] Y. Qi and M. Al-Imari, "An enabling waveform for 5G—QAM-FBMC: Initial analysis," in *2016 IEEE Conference on Standards for Communications and Networking (CSCN)*. IEEE, 2016, pp. 1–6.

[33] M. Bellanger, D. Le Ruyet, D. Roviras, M. Terré, J. Nossek, L. Baltar, Q. Bai, D. Waldhauser, M. Renfors, T. Ihalainen *et al.*, "FBMC physical layer: a primer," *Phydyas*, vol. 25, no. 4, pp. 7–10, 2010.

[34] R. Ahmed, T. Wild, and F. Schaich, "Coexistence of UF-OFDM and CP-OFDM," in *2016 IEEE 83rd Vehicular Technology Conference (VTC Spring)*. IEEE, 2016, pp. 1–5.

[35] C. Sexton, Q. Bodinier, A. Farhang, N. Marchetti, F. Bader, and L. A. DaSilva, "Coexistence of OFDM and FBMC for Underlay D2D Communication in 5G Networks," in *2016 IEEE Globecom Workshops (GC Wkshps)*. IEEE, 2016, pp. 1–7.

[36] B. Lim and Y.-C. Ko, "SIR analysis of OFDM and GFDM waveforms with timing offset, CFO, and phase noise," *IEEE Transactions on Wireless Communications*, vol. 16, no. 10, pp. 6979–6990, 2017.

[37] F. Schaich and T. Wild, "Waveform contenders for 5G - OFDM vs. FBMC vs. UFMC," in *2014 6th international symposium on communications, control and signal processing (ISCCSP)*. IEEE, 2014, pp. 457–460.

[38] R. Gerzaguet, N. Bartzoudis, L. G. Baltar, V. Berg, J.-B. Doré, D. Kténas, O. Font-Bach, X. Mestre, M. Payaró, M. Färber *et al.*, "The 5g candidate waveform race: a comparison of complexity and performance," *EURASIP Journal on Wireless Communications and Networking*, vol. 2017, no. 1, p. 13, 2017.

[39] A. A. Zaidi, J. Luo, R. Gerzaguet, A. Wolfgang, R. J. Weiler, J. Vihriala, T. Svensson, Y. Qi, H. Halbauer, Z. Zhao *et al.*, "A preliminary study on waveform candidates for 5G mobile radio communications above 6 GHz," in *2016 IEEE 83rd Vehicular Technology Conference (VTC Spring)*. IEEE, 2016, pp. 1–6.

[40] X. Zhang, L. Chen, J. Qiu, and J. Abdoli, "On the waveform for 5G," *IEEE Communications Magazine*, vol. 54, no. 11, pp. 74–80, 2016.

[41] Y. Liu, X. Chen, Z. Zhong, B. Ai, D. Miao, Z. Zhao, J. Sun, Y. Teng, and H. Guan, "Waveform design for 5G networks: Analysis and comparison," *IEEE Access*, vol. 5, pp. 19 282–19 292, 2017.

[42] S. Gökceli, B. Canli *et al.*, "Universal filtered multicarrier systems: Testbed deployment of a 5G waveform candidate," in *2016 IEEE 37th Sarnoff Symposium*. IEEE, 2016, pp. 94–99.

[43] M. Danneberg, R. Datta, and G. Fettweis, "Experimental testbed for dynamic spectrum access and sensing of 5G GFDM waveforms," in *2014 IEEE 80th Vehicular Technology Conference (VTC2014-Fall)*. IEEE, 2014, pp. 1–5.

[44] D. Garcia-Roger, J. F. de Valgas, J. F. Monserrat, N. Cardona, and N. Incardona, "Hardware testbed for sidelink transmission of 5G waveforms without synchronization," in *IEEE International Symposium on Personal, Indoor and Mobile Radio Communications (PIMRC)*, Sep. 2016.

[45] A. A. Zaidi, R. Baldemair, H. Tullberg, H. Bjorkegren, L. Sundstrom, J. Medbo, C. Kilinc, and I. Da Silva, "Waveform and numerology to support 5G services and requirements," *IEEE Communications Magazine*, vol. 54, no. 11, pp. 90–98, 2016.

[46] P. Guan, D. Wu, T. Tian, J. Zhou, X. Zhang, L. Gu, A. Benjebbour, M. Iwabuchi, and Y. Kishiyama, "5G field trials: OFDM-based waveforms and mixed numerologies," *IEEE Journal on Selected Areas in Communications*, vol. 35, no. 6, pp. 1234–1243, 2017.

[47] A. T. Abusabah and H. Arslan, "NOMA for multinumerology OFDM systems," *Wireless Communications and Mobile Computing*, vol. 2018, 2018.

[48] A. Tusha, S. Doğan, and H. Arslan, "A hybrid downlink NOMA with OFDM and OFDM-IM for beyond 5G wireless networks," *IEEE Signal Processing Letters*, vol. 27, pp. 491–495, 2020.

[49] A. F. Demir and H. Arslan, "Inter-numerology interference management with adaptive guards: A cross-layer approach," *IEEE Access*, vol. 8, pp. 30 378–30 386, 2020.

[50] A. B. Kihero, M. S. J. Solaija, and H. Arslan, "Inter-numerology interference for beyond 5g," *IEEE Access*, vol. 7, pp. 146 512–146 523, 2019.

[51] A. Yazar and H. Arslan, "Reliability enhancement in multi-numerology-based 5g new radio using ini-aware scheduling," *EURASIP Journal on Wireless Communications and Networking*, vol. 2019, no. 1, p. 110, 2019.

[52] C. Campolo, A. Molinaro, F. Romeo, A. Bazzi, and A. O. Berthet, "5G NR V2X: On the Impact of a Flexible Numerology on the Autonomous Sidelink Mode," in *2019 IEEE 2nd 5G World Forum (5GWF)*. IEEE, 2019, pp. 102–107.

[53] F. Firyaguna, J. Kibilda, and N. Marchetti, "Application of flexible numerology to blockage mitigation in 5G-mmWave networks," in *2019 IEEE Global Communications Conference (GLOBECOM)*. IEEE, 2019, pp. 1–6.

[54] W. Saad, M. Bennis, and M. Chen, "A vision of 6G wireless systems: Applications, trends, technologies, and open research problems," *IEEE network*, vol. 34, no. 3, pp. 134–142, 2019.

[55] K. B. Letaief, W. Chen, Y. Shi, J. Zhang, and Y.-J. A. Zhang, "The roadmap to 6G: AI empowered wireless networks," *IEEE Communications Magazine*, vol. 57, no. 8, pp. 84–90, 2019.

[56] P. Yang, Y. Xiao, M. Xiao, and S. Li, "6G wireless communications: Vision and potential techniques," *IEEE Network*, vol. 33, no. 4, pp. 70–75, 2019.

[57] J. F. Monserrat, D. Martin-Sacristan, F. Bouchmal, O. Carrasco, J. Flores de Valgas, and N. Cardona, "Key technologies for the advent of the 6G," in *2020 IEEE wireless communications and networking Conference Workshops (WCNCW)*. IEEE, 2020, pp. 1–6.

[58] F. J. Velez *et al.*, "Multicarrier Waveform Candidates for Beyond 5G," in *CSNDSP-2020 12th International Symposium on Communication Systems, Networks and Digital Signal Processing*. Institute of Electrical and Electronics Engineers.

[59] X. Liu, T. Xu, and I. Darwazeh, "Coexistence of Orthogonal and Non-orthogonal Multicarrier Signals in Beyond 5G Scenarios," in *2020 2nd 6G Wireless Summit (6G SUMMIT)*. IEEE, 2020, pp. 1–5.

[60] Z. E. Ankarali, B. Peköz, and H. Arslan, "Flexible radio access beyond 5G: A future projection on waveform, numerology, and frame design principles," *IEEE Access*, vol. 5, pp. 18 295–18 309, 2017.

[61] A. F. Demir, M. Elkourdi, M. Ibrahim, and H. Arslan, "Waveform design for 5G and beyond," *arXiv preprint arXiv:1902.05999*, 2019.

[62] I. Baig, U. Farooq, N. U. Hasan, M. Zghaibeh, and V. Jeoti, "A Multi-Carrier Waveform Design for 5G and beyond Communication Systems," *Mathematics*, vol. 8, no. 9, p. 1466, 2020.

[63] "Filter Bank Multicarrier for Next Generation of Communication Systems, author=Farhang-Boroujeny, Behrouz," *EURASIP Journal on Advances in Signal Processing*, 2010.

[64] X. Wang, T. Wild, and F. Schaich, "Filter optimization for carrier-frequency-and timing-offset in universal filtered multi-carrier systems," in *2015 IEEE 81st Vehicular Technology Conference (VTC Spring)*. IEEE, 2015, pp. 1–6.

[65] X. Wang, T. Wild, F. Schaich, and A. F. Dos Santos, "Universal filtered multi-carrier with leakage-based filter optimization," in *European Wireless 2014; 20th European Wireless Conference*. VDE, 2014, pp. 1–5.

[66] V. Vakilian, T. Wild, F. Schaich, S. ten Brink, and J.-F. Frigon, "Universal-filtered multi-carrier technique for wireless systems beyond LTE," in *2013 IEEE Globecom Workshops (GC Wkshps)*. IEEE, 2013, pp. 223–228.

[67] O. Aydin, J. Gebert, J. Belschner, J. Bazzi, P. Weitkemper, C. Kilinc, I. Leonardo Da Silva, A. Zaidi, M. Schellmann, M. Filippou *et al.*, "D4. 1 Draft air interface harmonization and user plane design." METIS-II, 2016.

[68] A. Sahin, I. Guvenc, and H. Arslan, "A survey on multicarrier communications: Prototype filters, lattice structures, and implementation aspects," *IEEE communications surveys & tutorials*, vol. 16, no. 3, pp. 1312–1338, 2013.

[69] P. Achaichia, M. Le Bot, and P. Siohan, "Windowed OFDM versus OFDM/OQAM: A transmission capacity comparison in the HomePlug AV context," in *2011 IEEE International Symposium on Power Line Communications and Its Applications*. IEEE, 2011, pp. 405–410.

[70] P. P. Vaidyanathan, "Multirate digital filters, filter banks, polyphase networks, and applications: a tutorial," *Proceedings of the IEEE*, vol. 78, no. 1, pp. 56–93, 1990.

[71] T. M. Schmidl and D. C. Cox, "Robust frequency and timing synchronization for OFDM," *IEEE transactions on communications*, vol. 45, no. 12, pp. 1613–1621, 1997.

[72] C. Dick and F. Harris, "FPGA implementation of an OFDM PHY," in *The Thrity-Seventh Asilomar Conference on Signals, Systems & Computers, 2003*, vol. 1. IEEE, 2003, pp. 905–909.

[73] A. M. Abdelgader and W. Lenan, "The physical layer of the IEEE 802.11 p WAVE communication standard: the specifications and challenges," in *Proceedings of the world congress on engineering and computer science*, vol. 2, 2014, pp. 22–24.

[74] A. Viholainen, M. Bellanger, and M. Huchard, "Prototype Filter and Structure Optimization, ICT-211887 Project PHYDYAS (Physical Layer for Dynamic Access and Cognitive Radio) Technical Report D5. 1," 2009.

[75] I. . W. Group *et al.*, "IEEE standard for information technology–Telecommunications and information exchange between systems–Local and metropolitan area networks–Specific requirements–Part 11: Wireless

LAN Medium Access Control (MAC) and Physical Layer (PHY) specifications Amendment 6: Wireless Access in Vehicular Environments," *IEEE Std*, vol. 802, no. 11, 2010.

[76] Y. Mostofi and D. C. Cox, "Mathematical analysis of the impact of timing synchronization errors on the performance of an OFDM system," *IEEE Transactions on Communications*, vol. 54, no. 2, pp. 226–230, 2006.

[77] M. A. A. Hasan, F. Nabita, A. Khandakar, I. Ahmed, and F. Ahmed, "Analytical evaluation of timing offset error in OFDM system," in *2010 Second International Conference on Communication Software and Networks*. IEEE, 2010, pp. 3–7.

[78] H. Saeedi-Sourck, Y. Wu, J. W. Bergmans, S. Sadri, and B. Farhang-Boroujeny, "Sensitivity analysis of offset qam multicarrier systems to residual carrier frequency and timing offsets," *Signal Processing*, vol. 91, no. 7, pp. 1604–1612, 2011.

[79] "Impact of time and carrier frequency offsets on the FBMC/OQAM modulation scheme, author=Lin, Hao and Gharba, Mohamed and Siohan, Pierre," *Signal Processing*, vol. 102, pp. 151–162, 2014.

[80] T. Fusco, A. Petrella, and M. Tanda, "Sensitivity of multi-user filter-bank multicarrier systems to synchronization errors," in *2008 3rd International Symposium on Communications, Control and Signal Processing*. IEEE, 2008, pp. 393–398.

[81] Q. Bai and J. A. Nossek, "On the effects of carrier frequency offset on cyclic prefix based OFDM and filter bank based multicarrier systems," in *2010 IEEE 11th International Workshop on Signal Processing Advances in Wireless Communications (SPAWC)*. IEEE, 2010, pp. 1–5.

[82] A. Aminjavaheri, A. Farhang, A. RezazadehReyhani, and B. Farhang-Boroujeny, "Impact of timing and frequency offsets on multicarrier waveform candidates for 5G," in *2015 IEEE Signal Processing and Signal Processing Education Workshop (SP/SPE)*. IEEE, 2015, pp. 178–183.

[83] A. Osseiran, F. Boccardi, V. Braun, K. Kusume, and et al., "Scenarios for 5G mobile and wireless communications: the vision of the METIS project," *IEEE Communications Magazine*, vol. 52, no. 5, pp. 26–35, May 2014.

[84] J. F. Monserrat, G. Mange, V. Braun, H. Tullberg, G. Zimmermann, and O. Bulakci, "METIS Research Advances towards the 5G Mobile and

Wireless System Definition," *EURASIP Journal on Wireless Communications and Networking*, vol. 2015, no. 53, March 2015.

[85] M. Tesanovic, V. Venkatasubramanian, M. Schellmann, J. Bazzi, M. C. Filippou, D. Calabuig, O. Aydin, and C. Kilinc, "Air interface design for 5G: a METIS-II perspective," in *European Conference on Networks and Communications (EuCNC)*, June 2016.

[86] P. Marsch, I. D. Silva, O. Bulakci, M. Tesanovic, S. E. E. Ayoubi, T. Rosowski, A. Kaloxylos, and M. Boldi, "5G radio access network architecture: Design guidelines and key considerations," *IEEE Communications Magazine*, vol. 54, no. 11, pp. 24–32, 2016.

[87] X. Zhang, L. Chen, J. Qiu, and J. Abdoli, "On the waveform for 5G," *IEEE Communications Magazine*, vol. 54, no. 11, pp. 74–80, November 2016.

[88] G. P. M.-I. project, "Final air interface harmonization and user plane design," 2017.

[89] M. Danneberg, R. Datta, and G. Fettweis, "Experimental testbed for dynamic spectrum access and sensing of 5G GFDM waveforms," in *IEEE Vehicular Technology Conference*, Sep. 2014, pp. 1–5.

[90] J. Nadal, C. A. Nour, A. Baghdadi, and H. Lin, "Hardware prototyping of FBMC/OQAM baseband for 5G mobile communication systems," in *IEEE International Symposium on Rapid System Prototyping*, Oct. 2014, pp. 135–141.

[91] F. Kaltenberger, R. Knopp, M. Danneberg, and A. Festag, "Experimental analysis and simulative validation of dynamic spectrum access for coexistence of 4G and future 5G systems," in *IEEE Vehicular Technology Conference*, June 2015, pp. 497–501.

[92] G. Jue and S. Shin. Keysight Technologies White Paper 2015: Implementing a flexible testbed for 5G waveform generation and analysis.

[93] J. Nadal, C. A. Nour, and A. Baghdadi, "Low-Complexity Pipelined Architecture for FBMC/OQAM Transmitter," *IEEE Transactions on Circuits and Systems II: Express Briefs*, vol. 63, no. 1, pp. 19–23, Jan. 2016.

[94] R. Zayani, H. Shaiek, X. Cheng, X. Fu, C. Alexandre, and D. Roviras, "Experimental testbed of post-OFDM waveforms toward future wireless networks," *IEEE Access*, vol. 6, pp. 67 665–67 680, 2018.

[95] H. G. Feichtinger and T. Strohmer, *Gabor Analysis and Algorithms: Theory and Applications*. Springer, 1998.

[96] A. Sahin, I. Guvenc, and H. Arslan, "A survey on multicarrier communications: Prototype filters, lattice structures, and implementation aspects," *IEEE Communications Surveys Tutorials*, vol. 16, no. 3, pp. 1312–1338, Third Quarter 2014.

[97] A. R. S. Bahai, B. R. Saltzberg, and M. Ergen, *Multi Carrier Digital Communications: Theory and Applications of OFDM*. Springer, 2004.

[98] V. Kumbasar and O. Kucur, "ICI reduction in OFDM systems by using improved sinc power pulse," *Digital Signal Processing*, vol. 17, no. 6, pp. 997 – 1006, 2007.

[99] M. Bellanger, "FBMC physical layer : a primer," *PT-ICT Project PHYDYAS*, June 2010.

[100] P. Siohan, C. Siclet, and N. Lacaille, "Analysis and design of OFDM/OQAM systems based on filterbank theory," *IEEE Transactions on Signal Processing*, vol. 50, no. 5, pp. 1170–1183, May 2002.

[101] T.-Y. Sung, H.-C. Hsin, and Y.-P. Cheng, "Low-power and high-speed CORDIC-based split-radix FFT processor for OFDM systems," *Digital Signal Processing*, vol. 20, no. 2, pp. 511 – 527, 2010.

[102] E. O. Brigham, *The Fast Fourier Transform*. Prentice-Hall Inc, 1998.

[103] Z. Zhao, M. Schellmann, Q. Wang, X. Gong, R. Boehnke, and W. Xu, "Pulse shaped OFDM for asynchronous uplink access," in *2015 49th Asilomar Conference on Signals, Systems and Computers*, Nov 2015, pp. 3–7.

[104] D. S. Waldhauser, L. G. Baltar, and J. A. Nossek, "Adaptive equalization for filter bank based multicarrier systems," in *2008 IEEE International Symposium on Circuits and Systems*, May 2008, pp. 3098–3101.

[105] Y. Yang, T. Ihalainen, M. Rinne, and M. Renfors, "Frequency-domain equalization in single-carrier transmission: filter bank approach," *EURASIP Journal on Advances in Signal Processing*, vol. 2007, no. 1, p. 010438, 2007.

[106] T. G. S. Lutz Lampe, Andrea M. Tonello, *Power Line Communications: Principles, Standards and Applications from Multimedia to Smart Grid*. Wiley, 2016.

[107] 3GPP, "Study on new radio (nr) access technology (release 14)," Tech. Rep. 38.912 v14.0.0, Mar 2017.

[108] A. Osseiran, J. F. Monserrat, and P. Marsch, *5G mobile and wireless communications technology*. Cambridge University Press, 2016.

[109] 3GPP, "Cellular system support for ultra-low complexity and low throughput internet of things (ciot)," Tech. Rep. 45.820 v13.1.0, Dec 2015.

[110] I. Da Silva, S. E. El Ayoubi, O. M. Boldi, Ö. Bulakci, P. Spapis, M. Schellmann, J. F. Monserrat, T. Rosowski, G. Zimmermann, D. Telekom *et al.*, "5g ran architecture and functional design," *METIS II white paper*, 2016.

[111] J. Vihriälä, A. A. Zaidi, V. Venkatasubramanian, N. He, E. Tiirola, J. Medbo, E. Lähetkangas, K. Werner, K. Pajukoski, A. Cedergren *et al.*, "Numerology and frame structure for 5g radio access," in *2016 IEEE 27th annual international symposium on personal, indoor, and mobile radio communications (PIMRC)*. IEEE, 2016, pp. 1–5.

[112] A. Yazar and H. Arslan, "Flexible multi-numerology systems for 5g new radio," *Journal of Mobile Multimedia*, vol. 14, no. 4, pp. 367–394, 2018.

[113] S. Chen and C. Zhu, "ICI and ISI analysis and mitigation for OFDM systems with insufficient cyclic prefix in time-varying channels," *IEEE Transactions on Consumer Electronics*, vol. 50, no. 1, pp. 78–83, 2004.

[114] D. Tse and P. Viswanath, *Fundamentals of wireless communication*. Cambridge university press, 2005.

[115] T. Wang, J. G. Proakis, E. Masry, and J. R. Zeidler, "Performance degradation of OFDM systems due to Doppler spreading," *IEEE Transactions on Wireless Communications*, vol. 5, no. 6, pp. 1422–1432, 2006.

[116] 3GPP, "Technical specification group radio access network; channel model for frequency spectrum above 6 GHz (release 14)," Tech. Rep. 38.900 v14.2.0, Dec 2016.

[117] G. W. Paper, "5G Channel Model for bands up to 100 GHz." http://www.5gworkshops.com/5GCM.html, Dec 2015.

[118] P. Marsch, Ö. Bulakci, O. Queseth, and M. Boldi, *5G system design: architectural and functional considerations and long term research*. John Wiley & Sons, 2018.

[119] 3GPP, "Study on scenarios and requirements for next generation access technologies," Tech. Rep. 38.913 v14.2.0, May 2017.

[120] K. David and H. Berndt, "6G vision and requirements: Is there any need for beyond 5G?" *IEEE Vehicular Technology Magazine*, vol. 13, no. 3, pp. 72–80, 2018.

[121] S. J. Nawaz, S. K. Sharma, S. Wyne, M. N. Patwary, and M. Asaduzzaman, "Quantum machine learning for 6g communication networks: State-of-the-art and vision for the future," *IEEE Access*, vol. 7, pp. 46 317–46 350, 2019.

[122] Z. Zhang, Y. Xiao, Z. Ma, M. Xiao, Z. Ding, X. Lei, G. K. Karagiannidis, and P. Fan, "6G wireless networks: Vision, requirements, architecture, and key technologies," *IEEE Vehicular Technology Magazine*, vol. 14, no. 3, pp. 28–41, 2019.

[123] L. Zhang, Y.-C. Liang, and D. Niyato, "6G Visions: Mobile ultra-broadband, super internet-of-things, and artificial intelligence," *China Communications*, vol. 16, no. 8, pp. 1–14, 2019.

[124] D. PRADO ALVAREZ, "Creación de interfaces de realidad virtual móvil en unity 3d y validación experimental de sus requisitos de red," 2018.

[125] P. Frenger, J. Hederen, M. Hessler, and G. Interdonato, "Improved antenna arrangement for distributed massive MIMO," *WO patent application*, vol. 2018103897, 2017.

[126] Y. Zeng, B. Clerckx, and R. Zhang, "Communications and signals design for wireless power transmission," *IEEE Transactions on Communications*, vol. 65, no. 5, pp. 2264–2290, 2017.

[127] J. Wang, C. Jiang, H. Zhang, Y. Ren, K.-C. Chen, and L. Hanzo, "Thirty years of machine learning: The road to pareto-optimal wireless networks," *IEEE Communications Surveys & Tutorials*, 2020.

[128] S. Epstein, "Algorithmic no-cloning theorem," *IEEE Transactions on Information Theory*, vol. 65, no. 9, pp. 5925–5930, 2019.